Micro-Structure of Functional Particles and Particle Systems

Dissertation

Submitted for the Degree of

Doktor der Ingenieurwissenschaften (Dr.-Ing.)

in

Faculty of Engineering,

Christian-Albrechts-Universität zu Kiel

Mao Deng

Kiel

May 2015

Supervisor: Prof. Dr. Lorenz Kienle

Second reviewer: Prof. Dr. Rainer Adelung

Date of oral examination: 24. 06. 2015

Abstract

Nanoparticles and particle systems exhibit exceptional properties in various applications. In the present dissertation the results of the transmission electron microscopy (TEM) analysis in microstructures of nanoparticles and of hybrid nanocomposites with different length scales are presented. The functional particles and particle systems under study include samples from:

1. MoS_2 based catalysts and their composites. A photocatalyst MoS_2/carbon/phosphorus composite is synthesized, and high resolution TEM (HRTEM) visualizes the expanded (002) lattice planes. Electron energy loss spectroscopy (EELS) results suggest an ordered and sp^2 bonding dominated carbon species. *In situ* electron beam irradiation shows instability of the composite sample. The intercalation of graphitic carbon inside the 250 °C sample and the nanoslabs with more active sites in the 350 °C sample are responsible for their higher photocatalytic activities as compared to bulk MoS_2. With regard to an amorphous MoS_2 (PX) sample, *in situ* electron beam irradiation and *in situ* thermal annealing inside TEM both lead to an increased crystallinity. Yet statistic studies comparing the size distribution of the MoS_2 slabs reveal different crystallization mechanisms of the two pathways. The inherent coordinatively unsaturated sites inside the PX sample account for the high photocatalytic activity. In hydrodesulferizaton (HDS) catalysts where PX is promoted with cobalt, HRTEM reveals microstructural difference between samples prepared under different conditions, and their HDS catalytic activity is related accordingly. Quantitative analyses of electron diffraction show a good agreement with size distributions of MoS_2 nanoparticles. Kinematic and dynamic simulations of a diffraction pattern reveal the influence of HDS reaction on crystallinity and microstructure of MoS_2 phase. Computer simulation of the interface between MoS_2 and Co is performed for understanding promoter effect. For MoS_2/carbon composite as a potential candidate for catalyst and electrode, EELS analyses suggest a mixture of graphitic and carbide-like carbons. Synthesis conditions play an important role on the structure of the sample.

2. Quasi 1D MoO_3, SnO_2 nanorods and core-shell composite. For the MoO_3 nanorods, TEM structural and compositional studies reveal the growth direction and the highly defective structure of the orthorhombic MoO_3. The performance of the MoO_3 nanorods sensor toward ethanol vapor is related to the surface catalytic reaction on the lattice oxygen of MoO_3. The reaction is further facilitated by the defect rearrangement of the crystallographic structure. The fast gas response is due to the dimension of the MoO_3 nanorods. For the $SnO_2/Ga_2O_3/GaN:O_x$ composite, a comprehensive approach of energy filtered TEM, diffraction, HRTEM and *in situ* heating is applied to reveal the complex

structure of the sample. The influences of thermal annealing to the structure are demonstrated via *ex situ* and *in situ* heating experiments.

3. Carbon microtube (Aerographite, AG) and its variants. Beam sensitivity of AG is investigated with 80 kV and 300 kV EELS. The quantitative EELS result shows an increased π^*/σ^* peak ratio of the carbon K-edge when lowering the acceleration voltage of TEM, which indicates the 300 kV electron beam modifies the graphitic carbon into the amorphous carbon. A high temperature variant of the AG-like amorphous carbon is presented. The bonding state of carbon atoms is studied by examining both the high loss and the low loss regions of the carbon K-edge. A mixture of graphite- and diamond-like carbon bonding is signified. EFTEM elemental mapping reveals small traces of light elements like oxygen, nitrogen and carbon on AG based composites down to micro-/nano-scale. Furthermore, a novel hollow tubular structure of Aero-GaN is shown. Diffraction patterns and corresponding computer simulations suggest a possible intergrowth of GaN and ZnO phases. HRTEM simulation proves the structure of GaN and near-atomic resolution imaging discloses defective structure.

4. A 0-3 nanocomposite of CdSe (crystalline nanoparticles) and Cr_2Se_3 (amorphous matrix) is studied. The transformation of the 0-3 composite is studied under TEM *in situ* electron beam irradiation and thermal annealing. *In situ* irradiation removes the CdSe nanoparticles and a porous Cr_2Se_3 matrix with a slightly increased crystallinity is produced. *In situ* thermal annealing eliminates CdSe particles and generates crystalline nano- and micro Cr_2Se_3 particles, with an additional formation of chromium enriched crystallites. The results are compared with those of conventional *ex situ* methods.

Contents

List of Abbreviations

Å	Angstrom
AG	Aerographite
at. %	Atomic percent
ATM	Ammonium Tetrathiomolybdate: $(NH_4)_2MoS_4$
BT	Benzothiophene
BP	Biphenyl
bpy	2,2'-bipyridine
Bu	Butyl group ($-C_4H_9$)
CHB	Cyclohexylbenzene
CUS	Coordinatively Unsaturated Sites
CVD	Chemical Vapor Deposition
DBT	Dibenzothiophene
DDS	Direct Desulfurization
DF	Dark Field
EDX	Energy Dispersive X-Ray
EELS	Electron Energy Loss Spectroscopy
EFTEM	Energy Filtered Transmission Electron Microscopy
e^--h^+	electron-hole
ELNES	Energy Loss NearEdge Structure
eV	Electron Volt
EXAFS	Extended X-ray Absorption Fine Structure
EXELFS	Extended Energy Loss Fine Structure
FEG	Field Emission Gun
FFT	Fast Fourier Transform
FTS	Flame Transport Synthesis
HAADF	High Annular Angular Dark Field
HDS	Hydrodesulphurization
HRTEM	High Resolution Transmission Electron Microscopy
HRSTEM	High Resolution Scanning Transmission Electron Microscopy
HVPE	Hydride Vapor Phase Epitaxy
HYD	Hydrogenation
IFFT	inverse FFT
IR	Infrared Spectroscopy
LC	Lacey Carbon
LDOS	Local Density of States
Me	Methyl ($-CH_3$) group
NMR	Nuclear Magnetic Resonance
Ph	Phenyl group
RTP	Rapid Thermal Processing
SAED	Selected Area Electron Diffraction
STEM	Scanning Transmission Electron Microscopy
STM	Scanning Tunneling Microscopy
TEM	Transmission Electron Microscope
THDBT	Tetrahydrodibenzothiophene
vdW	van der Waals
XRD	X-ray Diffraction
XPS	X-ray Photoelectron Spectroscopy
ZLP	Zero Loss Peak

Motivation

Owing to its size effect nanoparticle presents unique possibilities for catalytic, electronic, semiconducting, biologic and mechanical applications. Hybrid particle systems contain assemblies of particles with different length scales (from nanometer to micrometer), phases, and compositions, where individual functions from the components can be unified to achieve a synergistic effect, thus expanding the horizon of nanoparticle applications.

As a result of stringent demands arising from state-of-the-art nanotechnology, a deliberate control and fabrication of nanoparticles and particle systems cannot be realized without reliable characterization approaches providing in-depth understanding of the nanomaterial. Transmission electron microscopy (TEM), especially high resolution TEM (HRTEM), has become an essential technique for analyzing nanomaterials.[1] In combination with spectroscopy methods and other external stimuli devices, modern TEM is capable of retrieving valuable information from key aspects including particle size, morphology, chemical composition, crystal microstructure, or the dynamics in the physical and chemical processes at the sub angstrom scale. This entitles TEM to be a versatile and powerful tool for both fundamental and practical research on functional nanoparticles and particle systems.

The scope of this thesis aims to study advanced TEM characterization and computer simulation methods to unravel the microstructure of a variety of functional nanoparticles and particle systems. The geometry and dimension of the specimens under study range from nanoparticles (< 100 nm in three dimensions, **Chapter 3**), quasi 1D nanorods (~100 nm at least in two dimensions and several µm in the third dimension, **Chapter 4**), hollow nano-/micro-tube networks (several µm in three dimensions yet with a few nanometer in wall thickness, **Chapter 5**), to hybrid nanostructured composites including core-shell nanorods (**Section 4.2**), nanocrystallite decorated 3D network (**Section 5.3**), and nanoparticle embedded matrix material (0-3 nanocomposite, **Chapter 6**).

To further elaborate the particular challenges and questions arisen in revealing the structure-property correlation by TEM, several functional nanoparticles and particle systems from different application fields are selected as following:

- **Chapter 3**: MoS_2 catalyst nanoparticles and their composites. Particularly, hydrodesulphurization catalyst and photocatalyst are of interest for environmental concerns[2] and for the world's demand for energy[3]. As the particle size is reduced to nanometer range, the surfaces with more defects, edge and corner sites become dominate over the bulk counterparts, which is highly beneficial for catalytic activities. [4,5] Moreover, the interface between different phases within the heterogeneous catalyst system plays an increasing role as the dimension of the particle decreases. [6] In addition to these structural

changes, the band gap of the photocatalyst can be modified due to the quantum size confinement effect. [7] Therefore, direct observation of the microstructures of the surface sites and interfaces with TEM is of great importance to further optimize the catalytic performance. Another factor that influences the catalytic property is the incorporation of carbon, either by manual introducing or as residual from precursors. [8,9,10,11] The role of carbon is still under debate,[12,13,14,15] which demands intensive study of the carbon phase within the catalysts. Consequently, a combined approach of TEM and EELS can be a promising method to probe locally the microstructure and bonding states of carbon simultaneously, satisfying the characterization requirement of high spatial resolution for nanoparticle catalysts.

- **Chapter 4**: Metal oxide (MoO_3 and SnO_2) semiconducting nanorods and composites. The size effect of a quasi 1D nanorod ascribes to its large surface to volume ratio; hence, the conductivity of the quasi 1D structure is strongly reliant on surface reactions.[16] TEM allows exceptional view of surface sites on the quasi 1D structure and fundamental insights into the microstructural origin of surface reactions, thus better understanding the structure-property correlation of the MoO_3 and SnO_2 nanorods based semiconductor devices.
- **Chapter 5**: Carbon based nanostructured materials and their variants. Carbon material is of high relevance for electronic and mechanical applications in the micro or nanometer range. [17,18] Various morphologies of carbon micro-/nanomaterials have been synthesized including carbon fullerite[19], fullerene[20], carbon nanotubes[21] and graphene[22]. Therefore, the correlation of the structure and properties is highly demanding for understanding these new carbon nanomaterials. TEM can provide an exceptional solution to reveal the morphology and microstructure of the carbon nanomaterials. EELS and energy filtered TEM (EFTEM) can enable a reliable detection and visualization of light elements, e.g. carbon, within the nanocomposite. Additionally, due to the presence of abundant allotropes and different phases of carbon, the physical and chemical properties largely depend on the bonding states of carbon atoms.[17,23] So far EELS technique is considered to be the most effective method to probe the bonding states of carbon materials, especially those of amorphous carbon.[17,24,25,26]
- **Chapter 6**: CdSe / Cr_2Se_3 nanocomposites. TEM proves to be an indispensable method to characterize morphology, structure and chemical property of all components in a nanocomposite for relating its structure and property. [27,28,29,30,31] However, the general examination of material inside the TEM is experimentally challenging as a result of an electron-beam induced damage to the sample. Even more complex damage phenomena arise when the electron beam interacts with nanoparticles and nanocomposites. [32,33,34,35,36] However, most of the previous reports pay less attention to the dynamic nature of the nanocomposite under external stimuli.[37] *In situ* TEM allows real-time monitoring to the microstructural and compositional evolution down to the atomic scale, therefore sheds light on the dynamic stability of CdSe based nanocomposites under external thermal and/or irradiation conditions.

Last but not least, TEM analysis applied to assemblies of nanoparticles is not commonly considered as a representative statistical method due to its localized nature. On the other hand,

XRD as the routine procedure for determining phase and structure of powder samples suffers from strong peak broadening and overlap in the case of nanoparticle and particle systems. Consequently, the possibility of quantitative and statistical evaluations of the crystal structure and phases of an assembly of nanoparticles by combining electron diffraction and computer simulation methods has been explored for only less than two decades.[38,39,40] Therefore, the quantitative analysis, modeling and simulating the statistic characteristics of the microstructure and phase of the particle system is critical to extend the capability of TEM techniques, which can allow further comprehensive prediction of the nanoparticle assemblies and systems.

Introduction to Theory

1 Experimental Techniques

In this chapter the principle of experimental techniques, i.e. TEM, will be introduced. Theories about electron diffraction, scanning transmission electron microscopy (STEM), high resolution transmission electron microscopy (HRTEM), and EELS will be briefly discussed with some practical examples from experiments conducted for this thesis work. In the last section of this chapter, information about the instrument, the experimental setup and methods of sample preparation applied in this work will be provided.

1.1 Transmission Electron Microscopy

Transmission electron microscopy is utilized in this work as a main characterization approach for direct microstructure imaging and atomic resolution chemical analysis. The most effective analyses include electron dispersive X-ray analyses (EDX), selected area electron diffraction (SAED), HRTEM, STEM and EELS. Various combinations of these methods are possible to provide a comprehensive insight into structural and chemical features at the nanoscale.

1.1.1 Electron Diffraction

For crystalline materials, an electron diffraction pattern can be obtained on the back focal plane of the objective lens of the microscope when the Laue condition is fulfilled during a high energy electron beam interacts with the atoms in a solid specimen. The Laue's condition is described by the equation:

$$\boldsymbol{k}_D - \boldsymbol{k}_I = \boldsymbol{g},$$

where $\boldsymbol{k}_D$ is the wave vector of the diffracted beam and $\boldsymbol{k}_I$ is that of the incident beam, $\boldsymbol{g}$ is the reciprocal lattice vector. The information for solving and refining crystal structures, including defect structures of the solids, can be determined by measuring and simulating the electron diffraction pattern.

For amorphous materials, the Laue's condition cannot be applied as the scattering of electrons can occur at every atom position within the specimen. Consequently, the diffraction intensities spread through the entire reciprocal space, i.e. broad and diffuse diffraction rings

are present in the diffraction pattern. The kinematical intensity I_k of an electron beam scattered from an isotropic amorphous specimen is given as[41]:

$$I_k = | f(\vec{k}) |^2 \sum_{i,j} e^{i2\pi \vec{k}\cdot(\vec{r_i}-\vec{r_j})}$$

From the intensity distribution of an amorphous diffraction pattern, a probability function $\rho(\vec{r})$ can be obtained, i.e. the radial distribution function (RDF):

$$\rho(\vec{r}) - \rho_0 = \frac{1}{r}\int_0^\infty \sum_{i\neq j} e^{i2\pi \vec{k}\cdot(\vec{r_i}-\vec{r_j})} \sin 2\pi kr \cdot dk ,$$

which estimates the probability to find an atom at a distance *r* from another atom.[41] Moreover, the coordination number of the nearest shells of an atom can be approximated.[42] RDF is an important feature to quantitatively evaluate an amorphous material. Therefore, electron diffraction in TEM can provide valuable information from amorphous materials.

1.1.2 High Resolution TEM

High resolution TEM (HRTEM) allows imaging of very thin (optimally less than 50 nm for light elements, 20 nm for heavy elements) crystalline solids as projection of intensities of the transmitted and interference electron waves. The phase difference between these waves, so called phase contrast, can be interpreted up to sub-angstrom level with the support of computer simulations from structure models. Phase contrast originates from a phase shift of the propagating electron wave when it interacts with specimen, which generates an interference of the diffracted electron beam with the primary beam on the specimen's exit plane. HRTEM has been so far the most powerful method to investigate defects, interfaces and crystal growth directions in solid material (e.g. semiconductor, catalyst, thermoelectric materials etc.). Moreover, HRTEM can offer close to atomic resolution method to study nanocrystalline materials, the crystallite size of which is beyond the resolution of conventional XRD analysis, thus often be considered as amorphous using the XRD criteria.

1.1.3 High Angle Annular Dark Field Scanning TEM

In the high angle annular dark field scanning TEM (HAADF-STEM) mode a high angle annular detector collects the elastically scattered electrons which are the primary incident electrons deflected at high angles when colliding with the specimen. The intensity of the image contrast is strongly correlated to the atomic number of the specimens, i.e. $|f(\Theta)| \sim Z^2$, where $f(\Theta)$ is the atomic scattering factor which represents the amplitude of the scattered electron waves and Z is the atomic number of the specimen. Accordingly, STEM image can be attributed to Z-contrast image. Unlike HRTEM image, direct interpretation of columns of the atoms in high resolution HAADF-STEM image can be conducted without any aid from the computer simulation.[43] Furthermore, by virtue of the nanoprobe nature of the focused

electron beam in STEM, this technique can be combined with spectroscopy methods, e.g. EDX and EELS, to provide chemical, electrostatic and structural information simultaneously down to the atomic scale.

1.2 Electron Energy Loss Spectroscopy

The EELS approach involves an inelastic scattering process during the beam-specimen interaction, where the energy loss of the transmitted beam electrons is analyzed by a magnetic prism spectrometer. Note that in this aspect the transmitted beam is referred as the Zero-Loss Peak (ZLP).

Due to the inelastic scattering of the incident electrons from the electrons inside the specimen, specific atoms of the specimen can be ionized. An example EEL spectrum of Fe_2O_3 is depicted in **Figure 1.1**. The peaks in the low-loss region (right after ZLP and up to ~50 eV) are plasmon peaks, which stem from the ionization of the valence electrons and accordingly can give hint about the electronic structure and the band gap. In core-loss region (which ranges from 50 eV up to several keVs), the position of higher energy loss edges in the EEL spectrum is associated with the binding energy of the corresponding inner atomic shell, e.g. ionization edges of the K, L shell, respectively, providing information of element species present in the specimen. As shown in **Figure 1.1**, the oxygen-K ionization edge and iron-L ionization edge are demonstrated. Besides the elemental information, more information can be inferred from the fine structures behind the core-loss edges, e.g. Energy-Loss Near-Edge Structure (ELNES) and EXtended Energy-Loss Fine Structure (EXELFS). They can give clues to the local coordination environment of crystal structures, such as allotropes (for example, graphite, diamond or carbide forms for carbon element), and the oxidation states of transition metals.

In the following sections several aspects of EELS technique are discussed with some practical examples on various samples obtained within the frame of this thesis work, or from collaborations with other project partners.

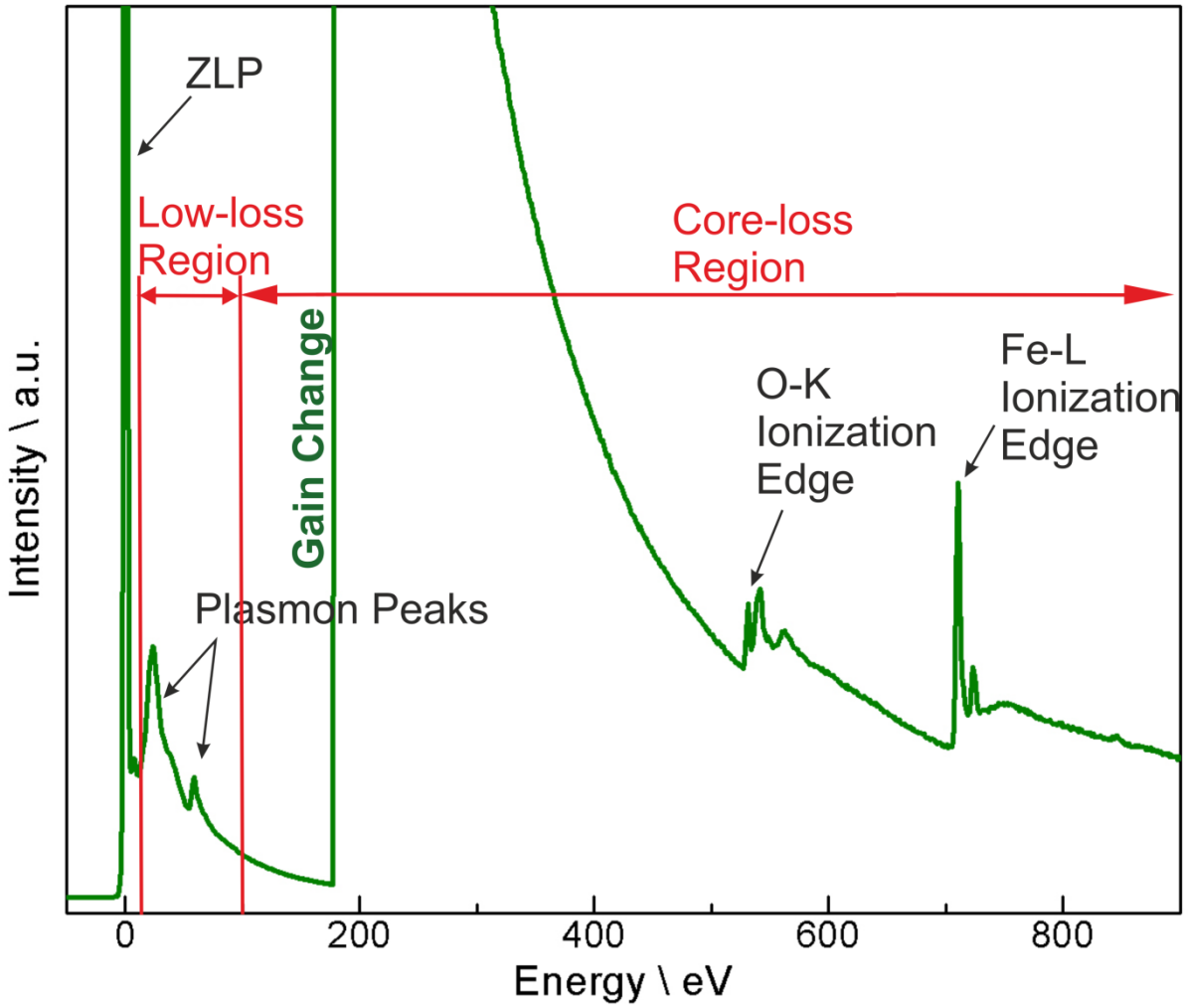

Figure 1.1 *The EEL spectrum of Fe_2O_3 exhibiting typical features in both low-loss and core-loss regions. Replotted from ref. 44.*

1.2.1 Energy-Loss Near-Edge Structure and the Influence of the Acquisition Parameter to the Fine Structures

ELNES is the fingerprinting fine structure appearing after an ionization edge and within a range of several tens of electron volt, while EXELFS starts from ~50 eV after ELNES.[45] (See **Figure 1.2**) It represents the unoccupied local density of states (LDOS) which are influenced by the chemical and crystallographic surroundings of the atom excited by the fast electrons.[46] Thus, ELNES can be used to determine the coordination number and the valence state of the specimen, provided that the experimental condition can be analogue to single scattering approximation, or the plural scattering stems from the thickness effect is deconvoluted (cf. **Section 1.2.5**).[46,47] Especially, the ELNES arose in transition metals, i.e. 'white lines', are widely investigated (cf. **Section 1.2.6)**. [48,49,50]

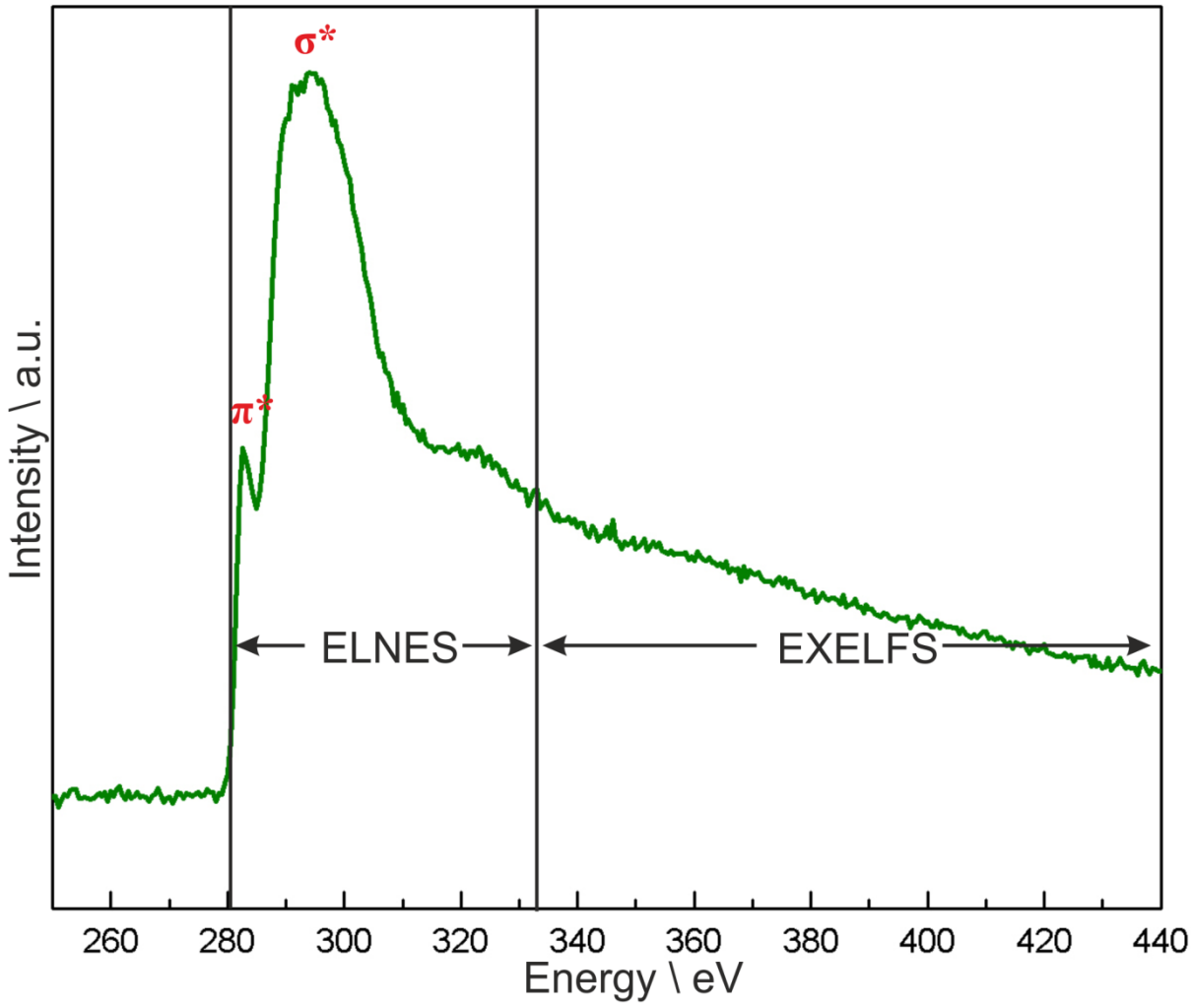

Figure 1.2 *Schematic illustration of ELNES and EXELFS fingerprinting in an EEL spectrum of the carbon K ionization edge. Within ~50 eV range after the onset of ionization edge (284 eV) the ELNES structures are presenting, while beyond 50 eV is mostly information from EXELFS. The π* and σ* peaks in the ELNES region of the C-K edge are marked out. Further discussions about the two peaks please refer to* ***Section 2.3****. Replotted from ref. 44.*

Practically, the ELNES is not only a representation of the local atomic environment of the solids, but can be influenced by an instrumental broadening due to the energy resolution of the electron source.[46] To better resolve the fine structures, a smaller entrance aperture size can be applied during the acquisition. The effect of different acquisition parameter is given in the following comparison (**Figure 1.3**). However, it must be noted that a smaller aperture size leads to a reduced intensity for the transmitted electron and thus worse signal-to-noise ratio. For critically thick samples a compromise of the energy resolution and peak intensity must be carefully chosen.

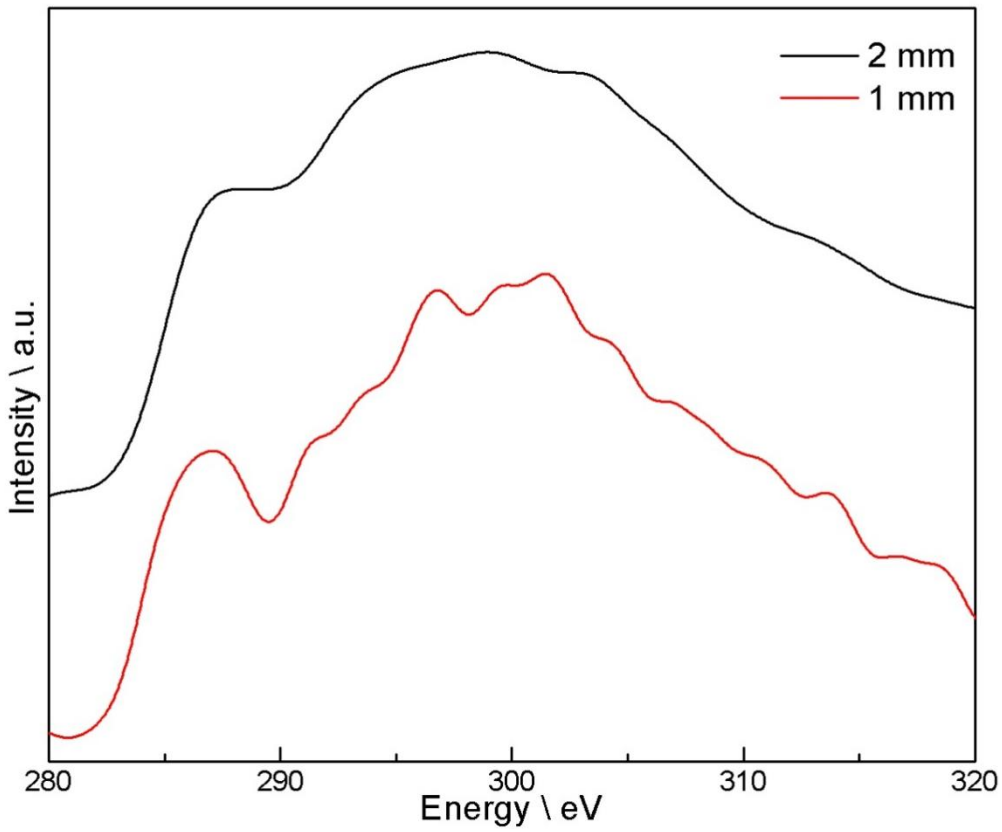

Figure 1.3 *Electron energy loss (EEL) spectra of the carbon K ionization edge (284 eV) of a MoS_2 / Carbon composite specimen recorded with different entrance aperture sizes. The spectrum with a smaller aperture size (1 mm in diameter, red line) reveals more details of the fine structures of the carbon ionization edge than that recorded with a bigger aperture size (2 mm in diameter, black line). Specimen prepared by David Westfall.*

To first establish that EELS is a repeatable and controllable method for investigation of the fine structures, comparison spectra are shown in **Figure 1.4**. Both spectra were obtained at the same position of a MoS_2/carbon composite sample only differing in the respective acquisition time. The two spectra exhibit the same fine structures and peaks at the same energy loss. There is no shift along the energy axis between these two acquisitions, indicating a stable electron beam during the experiment. The only difference between the spectrum obtained with 64 s and 90 s is the total counts of the transmitted electrons. It can be inferred from **Figure 1.4** that longer exposure time leads to a higher signal counts, but not necessarily to a higher signal to noise (S/N) ratio. Longer exposure time is not always preferable due to the possibility of undesirable modifications to beam sensitive samples by beam damage.

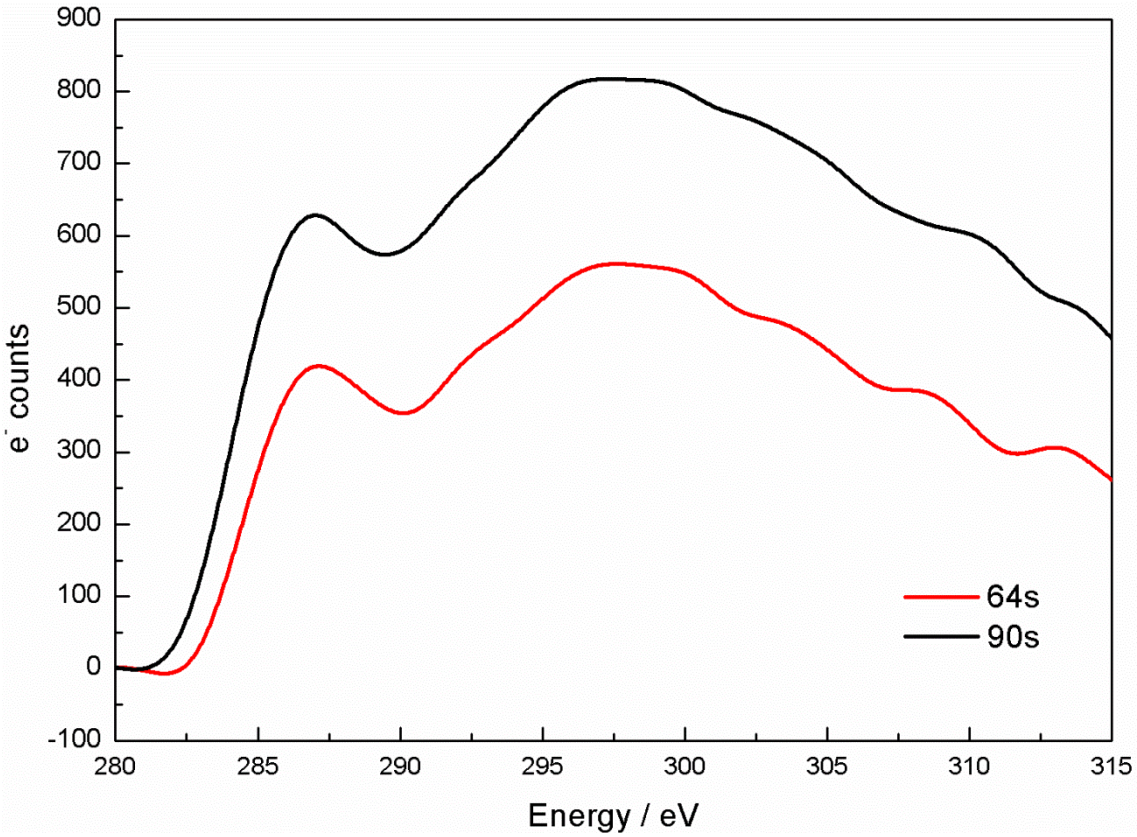

Figure 1.4 *Comparison of the EEL spectra obtained in different acquisition time in the same position of the sample Bu_4ATM_350 °C. No additional information can be achieved with a further increase of the exposure time. Structural or chemical modification introduced by the electron beam to the carbon phase was not observable. Specimen prepared by David Westfall.*

1.2.2 Energy Filtered TEM Elemental Map

Energy Filtered TEM (EFTEM) is an imaging method based on EELS technique. An imaging filter is the essential part to select the specific energy window in an EEL spectrum and to focus the selected energy loss electrons to form an image containing only the information from a selected ionization edge of the EEL spectrum. By applying a three window method to the ionization edge of interest, an intensity map can be created, which is referred as the elemental map. The three window method[51] is illustrated in **Figure 1.5**. EFTEM elemental maps are especially advantageous for revealing the spatial distribution of light elements (e.g. carbon, nitrogen, oxygen), which will be discussed in detail in the result part of this thesis later.

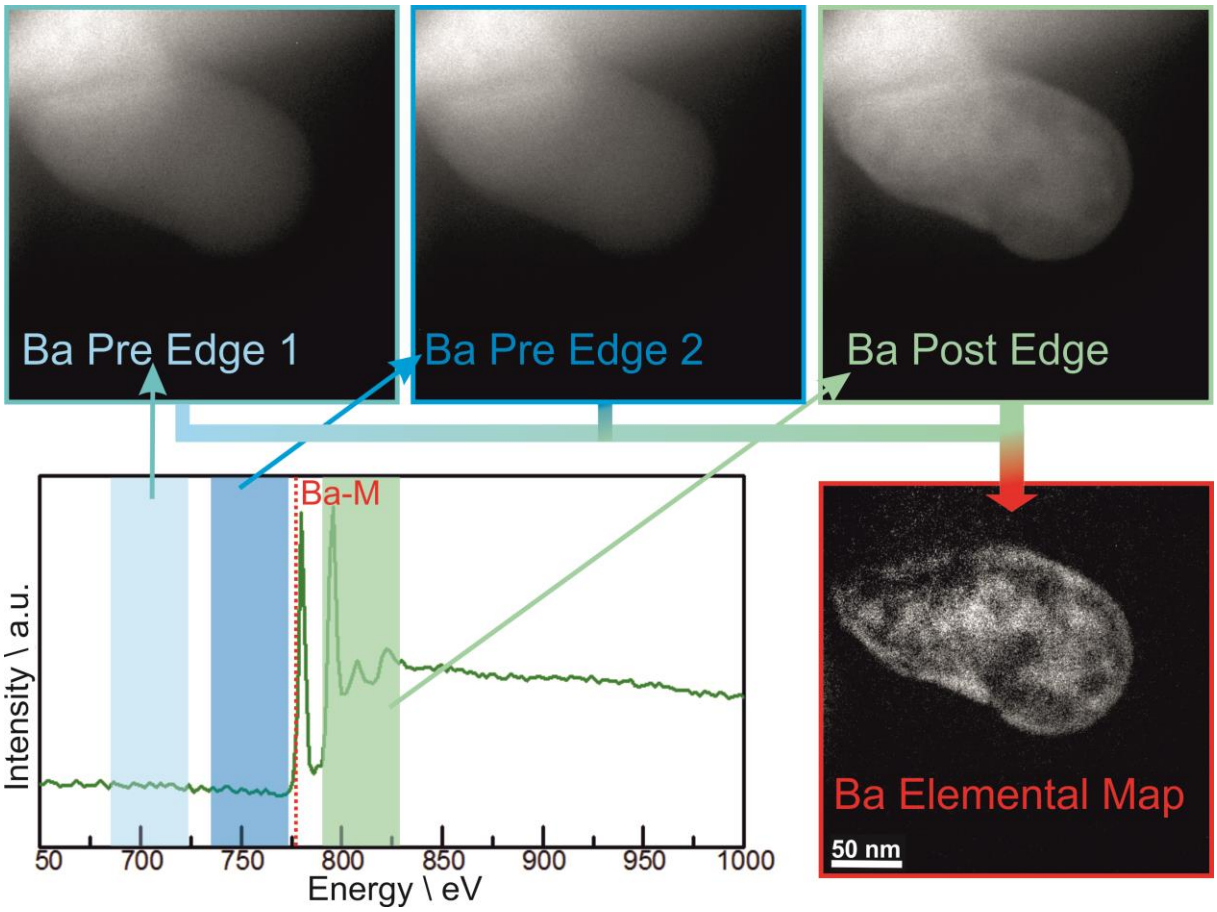

Figure 1.5 *A schematic illustration of the three window method for EFTEM elemental mapping. A Barium-M ionization edge (which is located at 781 eV) is shown in the EEL spectrum. The red broken line is assigned to the onset of the Ba-M edge. The three energy windows (slit width 40 eV) were chosen as shown: two pre edges which were located before the Ba-M edge and one post edge after the edge. The Barium elemental map is obtained by subtracting the intensities of the two pre edges from that of the post edge. A core-shell structure of the Ba-rich nanoparticle is clearly revealed in the Ba elemental map. Specimen prepared by Josef Eiblmeier.*

1.2.3 Thickness Measurement by the Log-Ratio Method

When the high energy electrons transvers through the specimen, the incident electron can undergo an inelastic collision with the valence electrons of the specimen, thus giving rise to a series of plasmon peaks after the presence of zero-loss peak in the low-loss region. The possibility of the plasmon excitation is related to the thickness of the sample, which can be determined by the log-ratio method: [52]

$$\frac{t}{\lambda} = \ln\left(\frac{I_t}{I_0}\right),$$

where t is the sample thickness, λ is the mean free path of the electron inside the sample, I_t is the intensity of all the plasmon peaks (including zero-loss peak) and I_0 is the intensity of zero-loss peak. An example of this method performed on an exfoliated MoS_2 sample is presented in **Figure 1.6**. Due to the layered structure of crystalline MoS_2 and its weak van der Waals bonding between the basal planes, an exfoliation of MoS_2 can be achieved by a straight

forward peeling method to obtain several layers or even single layer of MoS_2. The MoS_2 nanoparticles exhibit a wide variation of thickness. By applying the log-ratio method in EELS, the monitoring of the thickness of the MoS_2 layers obtained via the peeling process can be enabled.

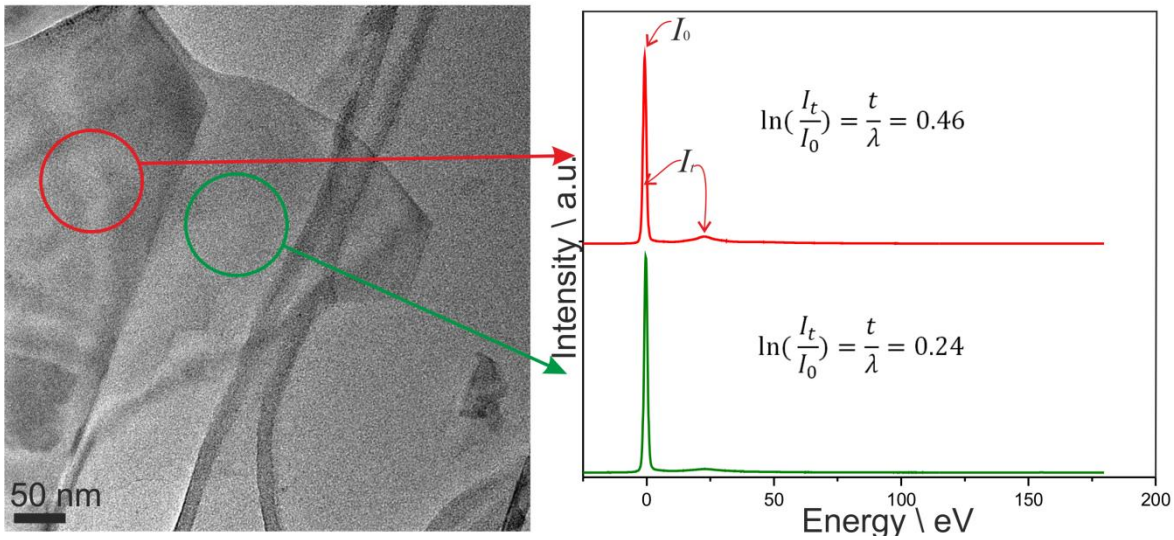

Figure 1.6 *Comparison of the low-loss EEL spectrum acquired from two regions on one nanoflake of scotch-tape-peeled MoS_2 specimen. The different Plasmon-to-ZLP ratios indicate distinct thickness differences on the two marked regions: the red marked region is thicker with a relative thickness of 0.46 λ, while the green area is thinner with a thickness of 0.24 λ. Meanwhile a qualitative thickness difference can be referred according to the contrast difference in the TEM micrograph on the left.*

Furthermore, the absolute value of the sample thickness can be determined when the inelastic mean free path λ is known, which can be calculated following a semi-empirical equation[52]:

$$\lambda\ (nm) \approx \frac{106F}{\ln(2\beta\ E_0/E_m)}\frac{E_0}{E_m}$$

Once the incident energy E_0 of the electron source, the collection semiangle β and the sample composition related factor E_m and the relativistic factor F are known, the mean free path (with the unit of nanometer) can be estimated. It should be noted that E_m is a factor requires the average atomic number of the sample, therefore this semi-empirical equation applies only for samples with known composition.

1.2.4 Thickness Map via Energy Filtered TEM Method

Using EFTEM mapping method, a thickness map of a region of interest can be generated. It is a fast and reliable approach to measure the sample thickness as compared to other TEM techniques.[53] The principle of this method is based on the log-ratio method, where the brightness of every pixel in the thickness map represents the ratio of thickness to mean free path ($\frac{t}{\lambda} = \ln(\frac{I_t}{I_0})$) of the region. With the selection of a scan direction, a thickness profile can

be obtained. A case study by means of EFTEM thickness mapping is presenting in **Figure 1.7**. In the left panel of **Figure 1.7**, a zero-loss peak image recorded from an iron oxide crystalline nanowire is depicted. The ZLP image filtered out the inelastically scattered electrons, thus the contribution of the image contrast only comes from the transmitted zero-loss electrons. However, a fraction of the zero loss electrons can undergo diffraction scattering when the Laue condition is satisfied, so the contrast of the ZLP image consists of both thickness and diffraction contrasts. A thickness map of the same region is shown in the middle panel of **Figure 1.7**: a brighter stripe in the middle of the nanowire indicates a region with a higher thickness. By generating a thickness profile from the marked region (**Figure 1.7**, green box), a more quantitative estimation can be enabled. It reveals unambiguously a bump in the thickness profile, indicating a wedge shape instead of a flat geometry of the nanowire (see right panel, **Figure 1.7**). This thicker stripe in the middle is later identified to be a twin boundary as well.[54]

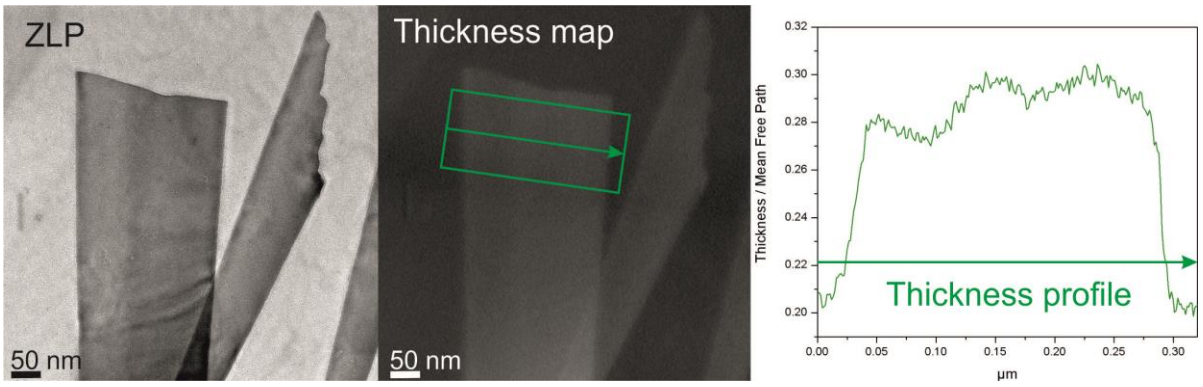

Figure 1.7 *Zero-loss peak EFTEM image (left panel) and the corresponding thickness map (middle panel) from an iron oxide microfiber. The thickness profile generated (right panel) from the green box marked region in the thickness map revealed a thick stripe in the middle of the wire. The arrow indicates the direction of the line scan from the starting point to the ending point. Sample synthesized by Dr. Dawit Gedamu. TEM measurement performed in collaboration with Dr. Burak Erkatal.*

1.2.5 Plural Scattering and Deconvolution Methods

In ideal conditions, the fast electron beam is scattered only once within the specimen. When the specimen is relatively thick ($\frac{t}{\lambda} > 2$), the incoming electron will undergo plural or even multiple scattering. The plural and multiple scattering affect the original shape of the energy loss edge, and further introduce error to the quantification of the EEL spectrum. Deconvolution is an approximate routine to remove the influence of plural scattering and to enable an enhanced signal-to-noise ratio of the core-loss edge. It is especially beneficial for quantification of the EEL spectrum. Three kinds of deconvolution method are of importance: *the Fourier-Log method*, *the Fourier-Ratio method* and *the multiple least-squares fitting*.[55] In this thesis, *the Fourier-Ratio method* is used since it is a more practical method as it takes the low-loss region spectrum as real time reference for background fitting. The principle of this method is to subtract the Fourier transform of the low-loss spectrum which contains plasma intensity arising mostly from plural scattering and inelastic scattering within the specimen. A comparison is shown before and after the deconvolution procedure in **Figure 1.8**.

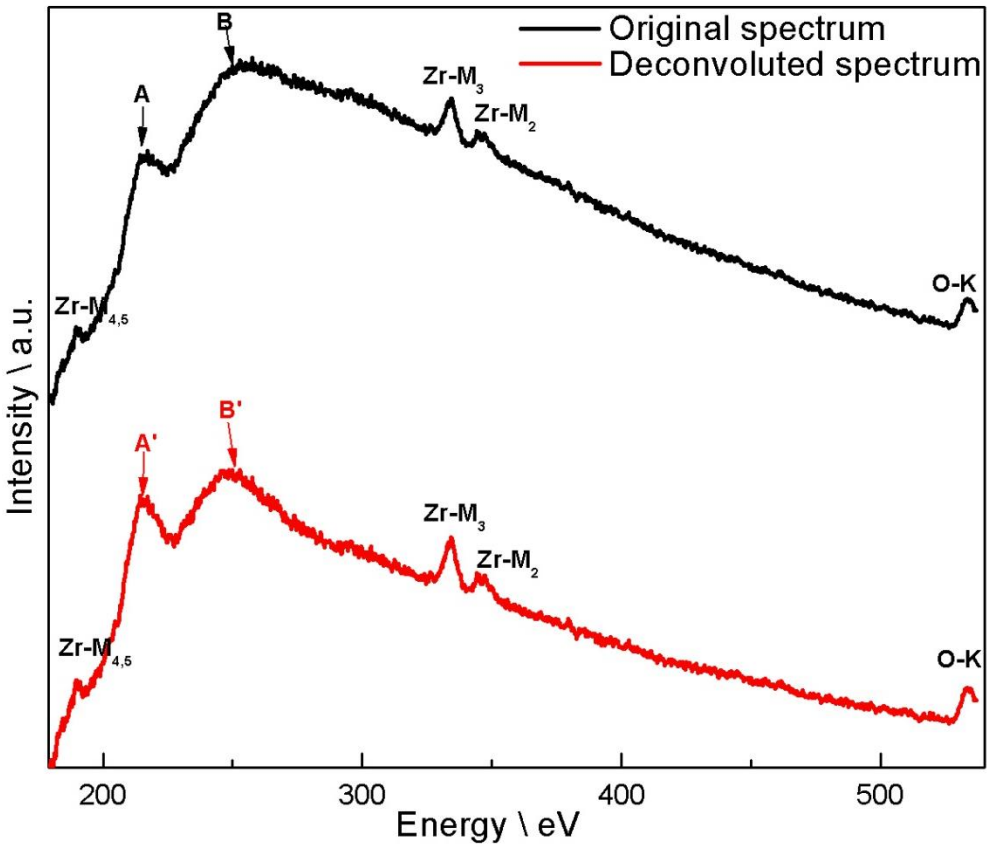

Figure 1.8 *Core-loss spectra of zirconium M ionization edges obtained from a FIB specimen of a zirconium oxide thin film. The upper black profile is the original spectra only after background extrapolation and subtraction, which shows a deformed shape of the peaks marked as A and B. The lower red one is after applying the Fourier-Ratio deconvolution method. The deconvoluted spectrum exhibits a higher signal-to-noise ratio and the ratio of near edge finestructure features A' and B', which provides important information about the oxidation state of zirconium within the sample, is different as compared with that of the original spectrum. Sample preparation and TEM measurement performed in collaboration with Dr. Ulrich Schürmann and Justus-Liebig-University, Giessen.*

1.2.6 White Lines in Transition Metal

White lines arise from the excitation of 2p electrons and their transition to the narrow unoccupied 3d electron orbit during the process of a high energy incident electron interacts with the electrons in a transition metal. The white line represents the features of the empty 3d states. In transition metals, the sharp double peaks of the white line are localized in the $L_{2,3}$ ionization edge. The splitting of the L edge of these elements is a result of spin-orbit splitting, where the transition from the $2p_{3/2}$ level (L_3 edge) has different ionization energy than from the $2p_{1/2}$ transition (L_2 edge). The ratio of the intense $L_{2,3}$ sharp peaks, the position of the peak onset and the width of the peak can provide pivotal information of the oxidation state or valence state of the transition metal elements.48 An example of the copper white line spectrum obtained via EELS method is shown in **Figure 1.9**. The double peak of the copper L_2 and L_3 edges has an energy separation of around 20 eV. The $L_{2,3}$ edge of pure copper exhibits a more broadened feature as compared to that of copper oxide, due to the completely filled 3d state of copper which cannot accommodate a transition from the 2p electrons. The

copper oxide is identified as Cu_2O due to the much sharper $L_{2,3}$ lines (referred as white lines) arising from the empty state of 3d orbit of copper oxide. [56]

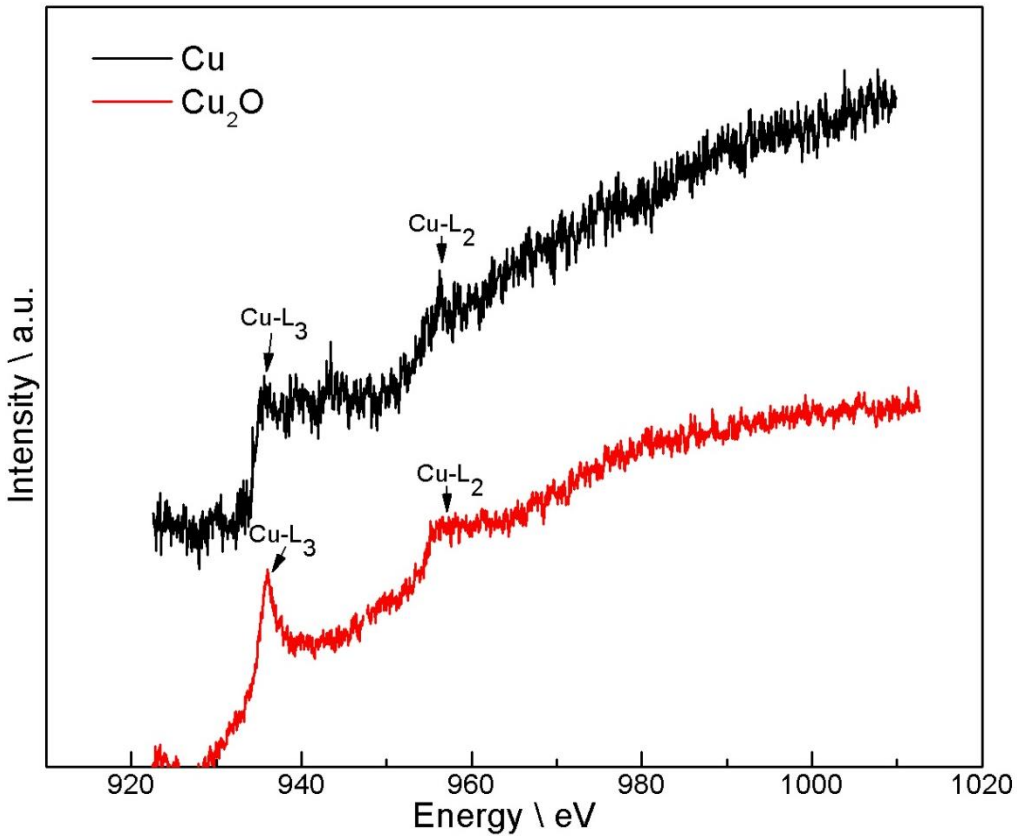

Figure 1.9 *A comparison of EEL spectrum and their ELNES of a metallic copper thin film (black line) and an oxidized region (red line) on the copper film. The oxidized region exhibits a different near edge fingerprinting from that of the metallic copper. Sample preparation and TEM measurement performed in collaboration with Dr. Viktor Hrkac, and Helmut-Schmidt-University, Hamburg.*

1.3 Instrumentation

In this section the instrumental setup, computer analysis software and the sample preparation methods are introduced.

1.3.1 Equipment and Parameter Setup for TEM Measurement

The measurements were performed on the following three transmission electron microscopes:

1) **FEI Tecnai F30 G2 STwin**: operated at 300 kV (Field emission gun (FEG), spherical aberration coefficient C_S = 1.2 mm) at TEM center, CAU Kiel.
    - TEM micrographs were recorded with a Gatan Multiscan CCD camera (2k x 2k).
    - EDX analyses were performed in TEM or STEM mode with a Si/Li detector (EDAX System).
    - EFTEM elemental maps were acquired with an entrance aperture size of 5 mm and a post-column Gatan Image Filter.
    - EEL spectra were acquired within a transmitted area with a diameter of 100~200 nm on different particles in the samples. The acquisition settings for different samples are specified in **Table 1.1**.

2) **Philips CM 30 ST microscope**: (LaB_6 cathode, 300 kV, C_S = 1.15 mm) performed by *Viola Duppel* at Max-Planck-Institute for Solid State Research.

3) **FEI Titan^3 G2 60-300 microscope:** (Extreme field emission gun (x-FEG)) Cs-corrected with a GIF Quantum Gatan imaging filter: operated at 80 kV for EELS analysis and performed by *Dr. Andriy Lotnyk* at Leibniz Institute of Surface Modification.

Table 1.1 *EELS acquisition settings for samples analyzed in this thesis.*

	$MoS_xC_yP_z$ (Section 3.1)	**Carbides and graphite references (Section 3.4)**	**MoS_xC_y (Section 3.4)**	**Aerographite (Section 5.2)**		**Amorphous carbon sample (Section 5.3)**
Acceleration voltage (kV)	300	300	300	80	300	300
Entrance aperture size (mm)	1	1	1	2.5	1	1
Energy dispersion (eV/pixel)	0.2	0.03	0.03	0.1	0.1	0.05
Acquisition time (s)	8~16	64	64	50	50~60	16 (High-loss) 2 (Low-loss)
Energy resolution (eV)	1.4	1.2	1.2	0.8	1.4	1.4

1.3.2 Software for TEM Data Analysis and Simulation

The TEM micrographs (including Fourier analyses), EEL spectra and EFTEM elemental maps were evaluated with a Gatan software package: Digital Micrograph 1.8. HRTEM micrographs were filtered by Wiener HRTEM filter[57] which is integrated in Digital Micrograph as software plug-in. The inverse FFT (IFFT) is generated by applying a band pass mask to the FFT pattern of HRTEM micrograph with a specific frequency range. In this manner, all spatial frequencies outside the mask are filtered out, and the resulting IFFT calculation exhibits the only wanted spatial frequency information from reciprocal space in real space region.

The EEL spectra were background subtracted and deconvoluted by applying the Fourier-ratio method[i] for further evaluation. The peak position is determined by calculating the first and second derivatives of the spectra using Origin software. The point is considered to be the local maxima of the spectrum where the first derivative equals to zero and the second derivative is smaller than zero.

The rotational average profiles of SAED patterns are generated via a plug-in script (Difftool)[58] of Digital Micrograph software. The Difftool integrates the intensities of each diffraction ring over an angular range from 0° to 359°, and the diffraction rings start from the origin of the primary beam in a SAED pattern. The vertical axis of the rotational average profile is the diffracted intensity of a corresponding diffraction ring, and the horizontal axis represents the scattering vector length in the reciprocal space. For the background subtraction of the rotational average profiles, a Matlab program written by *Torben Dankwort* and *Igor Barg* was applied to fit an exponential decay curve in the minima of the profile and then subtract the fitted background.

The computer simulation of the experimental HRTEM micrographs and the rotational average profiles were carried out by using a multi-slice approach incorporated in the software package JEMS[59].

The HAADF-STEM images, EDX spectra and STEM-EDX nanoprobe elemental analysis (line scans and elemental maps) were analyzed with TEM Imaging & Analysis (TIA) software version 4.2.

1.3.3 Sample Preparation

TEM sample preparation:

Powder samples were prepared mostly by *Christin Szillus*. The samples were suspended in butanol and ultrasonically dispersed for 3-5 min. Subsequently, the suspended powder was transferred onto a TEM support (a lacey carbon film on 200 mesh copper grid for normal samples, a SiN grid for samples for carbon EELS analysis, and molybdenum or gold grids for

[i] See Section **1.2.5**.

in situ TEM heating) by dropping 1-2 droplets of the solution onto the sample grid. The prepared TEM samples were dried at room temperature for several minutes.

Samples with morphology of hollow micro- or nano-tube were prepared via a solvent-free procedure to avoid the influence from solvent. A small amount of the powder was grind, a TEM sample grid contacted to the powder and a few particles were attached to the grid by Van der Waals force.

Synthesis methods for samples characterized in this thesis:

$MoS_xC_yP_z$ (Section 3.1):

The MoS_2 based carbon composite ($MoS_xC_yP_z$) is prepared by *John Djamil* from *Institute of Inorganic Chemistry, CAU Kiel.* A phosphorus and carbon containing organic precursor $(Ph_4P)_2MoS_4$ (Ph = Phenyl group) was thermal decomposed at different temperatures, i.e. 250 °C and 350 °C, to obtain composite samples.

PX (Section 3.2):

The amorphous MoS_2 based material named as PX is synthesized by *Felix Niefind* from *Institute of Inorganic Chemistry, CAU Kiel*. The precursor $(NH_4)_2MoS_4$ (ammonium tetrathiomolybdate, ATM) was first ball milled and stored in a desiccator together with the reducing agent $NH_2NH_2{\cdot}H_2O$ (hydrazine monohydrate) for 20-30 days. After drying in another desiccator, the final product has a chemical formula of $MoS_xN_yH_z$. The final product has a chemical formula of $MoS_xN_yH_z$. The value x of sulfur content is in a range of 2.0 ~ 2.2, and the value y of nitrogen content varies from 0.64 to 0.99. The hydrogen molar ratio z is between 3.2 and 3.8.

PXCo (Section 3.3)

Amorphous MoS_2 (PX) / Co composite sample is prepared by *Felix Niefind*. The PX sample synthesized in **Section 3.2** was used as a precursor here for obtaining MoS_2 as a HDS catalyst. The cobalt promoter is generated from another precursor tris-(N,N-dimethyldithiocarbamato)-cobalt(III) ($Co[S_2CN(CH_3)_2]_3$). The two precursors were mixed under argon atmosphere with an atomic ratio of Co / (Co+Mo) of 0.3 by ball milling, then the mixture was heated in two different gas environment and three different temperatures. As shown in **Section 3.2**, the PX precursor starts to crystallize at around 350 °C; therefore the starting temperature of the heat treatment for the samples is set to the initial crystallization temperature. It allows investigations into the influence of different synthesize conditions on the structural and catalytic properties of the different samples.

Table 1.2 *Overview of the preparation conditions of PX / Co samples. (Reprinted from ref. 60, Copyright (2015), with permission from Elsevier.)*

Sample before HDS	Sample after HDS	T / °C	Atmosphere
PXCo1	PXCo1m	350	H_2 / N_2 (Forming gas)

PXCo2	PXCo2m	380	H_2 / N_2 (Forming gas)
PXCo3	PXCo3m	410	H_2 / N_2 (Forming gas)
PXCo4	PXCo4m	350	Nitrogen
PXCo5	PXCo5m	380	Nitrogen
PXCo6	PXCo6m	410	Nitrogen

MoS_xC_y (Section 3.4)

The synthesis of MoS_2/carbon composite (MoS_xC_y) sample is completed by *David Westfall* from *Institute of Inorganic Chemistry, CAU Kiel*. Three samples were prepared and named as Bu_4ATM_350 °C, Bu_4ATM_750 °C and Me_4ATM_750 °C, by decomposition in argon atmosphere of tetraalkylammonium thiomolybdates ($R_4N[MoS_4]$). R is a general notation for an aliphatic hydrocarbon residue. Here in this study, it can be Bu = butyl ($-C_4H_9$) group, or Me = methyl ($-CH_3$) group, respectively, as it is denoted in the names of the three samples. Intrinsically, Bu-group has longer carbon chains than Me-group.

Decomposition was achieved with a linear heating ramp reaching the final temperature – 350 °C and 750 °C respectively - in 3 h and a dwelling time at the final temperature for 2 h. Subsequently the samples were quenched to room temperature within few minutes by removing them from the heating zone. Reference graphite sample was treated in the same heating ramp condition up to 750 °C for 2 h to provide a controllable comparison with the as prepared composite samples.

Aerographite and its variant (Section 5.1 and 5.2)

The synthesis of the Aerographite material is essentially a sacrificial CVD process on ZnO template. It includes two processes: (1) Preparing a template of a ZnO micro-tetrapod interconnecting network via Flame Transport Synthesis, a modified chemical vapor deposition (CVD) method.[61] (2) The growth of the carbon microtubes on the ZnO tetrapods is achieved by a conventional CVD procedure, where Toluene is the evaporation source for providing carbon element. Meanwhile in combination with a heat treatment in an argon/ hydrogen atmosphere, the ZnO network is simultaneously etched away.[62,63] By adjusting the CVD parameter a variation of the Aerographite can be produced, ranging from highly graphitic carbon layers to relatively amorphous glassy carbon variants.[62] Moreover, by varying the source materials, e.g. using reactive gases leading to GaN instead of carbon, the synthesis of hollow-tube-like network of a specific compound exhibiting similar morphology as Aerographite can be achieved.

GaN/Aerographite Composite (Section 5.3)

The GaN nano-/micro-crystallites are deposited directly on Aerographite network via a hydride vapor phase epitaxy (HVPE) method by the group of *Prof. Dr. Ion Tiginyanu*, where the metallic gallium, hydrogen chloride (HCl) gas, ammonia (NH_3) gas and hydrogen (H_2)

were source materials and carrier gases. GaN was nucleated on the surface of Aerographite at 600 ºC, and anealled at 950 ºC for 10 min to obtain crystalline GaN nano-/micro-particles.

Aero-GaN (Section 5.4)

The Aero-GaN sample is synthesized by the group of *Prof. Dr. Ion Tiginyanu* at 850 ºC and 950 ºC via the HVPE approach on the interconnecting ZnO tetrapod network. This approach can be analogue to the sacrificial CVD method for growing Aerographite.

MoO_3 nano-/micro-rod (Section 4.1)

The MoO_3 quasi 1D nano-/micro-rod samples were synthesized by *Dr. Oleg Lupan* with a rapid thermal processing (RTP) method where the commercially available bulk molybdenum was heated at 670 °C and 800 °C respectively for 10~20 min in ambient air.

1.3.4 Other Characterization Methods

The investigation of visible light-driven hydrogen production from water (see Section **3.1.4** and **3.2.5**) is performed by cooperation partner of *John Djamil* and *Felix Niefind* from *Institute of Inorganic Chemistry, CAU Kiel*. In the reaction, MoS_2 and MoS_2 based composite samples are used as water reduction catalysts together with a sacrificial electron donor (trimethylamine) and a photosensitizer component ($[Ru(bpy)_3](PF_6)_2$ (bpy = 2,2'-bipyridine)) in an acetonitrile/water mixture. The visible light source ($\lambda > 420$ nm) is generated by a 300 W Xe lamp with an optical cutoff filter. The principle of the photocataltic reaction with an additional photosensitizer is: During the water splitting reaction, the photosensitizer is firstly excited by the photons from the visible light and thus generates electrons transfer to the MoS_2 photocatalyst. Subsequently, the sacrificial electron donor re-reduces the photosensitizer to go back to the original unexcited state.[64]

2 Application Background

In this chapter a theoretical background of the materials studied in this thesis will be introduced. The principles for the materials as hydrodesulphurization catalyst, photocatalyst and gas sensor are briefly discussed to provide an overview of their application background. Furthermore, the correlation between their structural property and functional activity, e.g. the catalytic activity, sensitivity of the gas sensor, is emphasized from electron microscopy analysis point of view.

2.1 Hydrodesulphurization Catalyst

Diesel fuel is a crucial energy source worldwide, which is refined from crude oil. During the fuel combustion, several sulfur compounds in the diesel fuel generate harmful sulfur oxide which is considered as a major contribution to air pollution. Stringent environment regulations have been applied to limit the sulfur content to a very low level in fuel industry all around the world.[2] In addition, even a small trace of sulfur poisons other catalysts in the fuel hydrocracking and refining reactions. Therefore, catalyst to enhance the hydrodesulphurization is one of the essentials in the production of diesel fuel to reduce the sulfur content.

2.1.1 Hydrodesulphurization Reaction

In a simplified scenario, a Hydrodesulphurization (HDS) reaction includes steps such as hydrogenation of unsaturated bonds on the aromatic rings of sulfur species, and hydrogenolysis of carbon-sulfur bonds. Benzothiophenes (BTs) and dibenzothiophenes (DBTs) are the most common species containing sulfur in the crude oil.[65] The two routes of HDS are the hydrogenation pathway (HYD) and the direct desulfurization pathway (DDS), which are schematically shown in **Figure 2.1**. The final product generated via the DDS pathway is biphenyl (BP). From the HYD pathway there are an intermediate product tetrahydrodibenzothiophene (THDBT) and a final product cyclohexylbenzene (CHB). Therefore, the catalytic selectivity between HYD and DDS can be estimated by the ratio of the concentrations of the products from the two pathways:

$$S_{HYD} / S_{DDS} = ([CHB] + [THDBT]) / [BP]$$

To study the different reaction pathways and selectivity can give valuable clues to understand different active sites in the HDS catalysts (see **Section 3.3**) and further reveal the mechanism of HDS reaction.

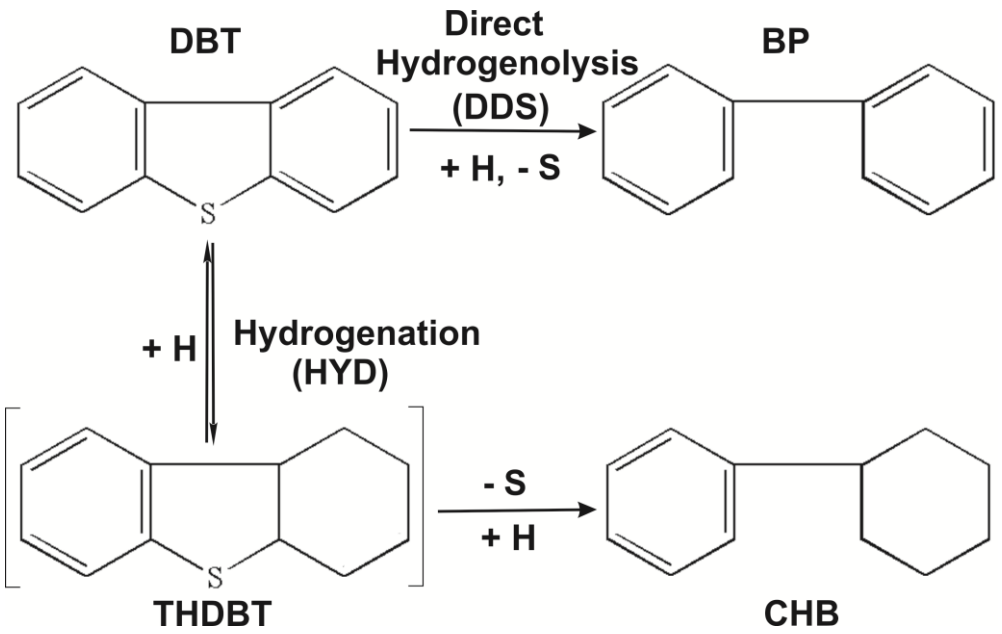

Figure 2.1 *Schematic representation of the two pathways occurring in hydrodesulphurization (HDS) of DBT.*

2.1.2 Hydrodesulphurization Catalyst

With increasing numbers of alkyl groups substituting the hydrogen atoms on the aromatic ring of the BTs or DBTs, the HDS process becomes more difficult, because the steric hindrance of such BTs and DBTs does not favor carbon-sulfur (C-S) bond cleavage[66], which is referred as the 'deep HDS' process.

An economical way to facilitate the deep HDS is to develop high performance HDS catalysts. The most cost efficient and commonly used HDS catalysts are transition metal sulfides as bulk material (unsupported catalyst) or nanoparticles dispersed on a carrier material (supported catalyst). Transition metal sulfides are mainly molybdenum disulfide (MoS_2) and tungsten disulfide (WS_2). The materials used as supports for the HDS catalyst exhibit generally high surface to volume ratios such as γ-Al_2O_3[67], TiO_2[68], carbon nanotubes[69], and mesoporous silica materials like SBA-15[70], MCM-41[71], Zeolites[72], etc.

The activity of the HDS catalysts is the total conversion percentage of DBT with respect of time. According to the conversion rate of DBT, the rate constant of the HDS reaction can be calculated. Commercial HDS catalysts adds a small amount of cobalt (Co) or nickel (Ni), which are considered as 'promoters', to increase the activity of the catalyst. The promoted catalysts are abbreviated as CoMoS/NiMoS or CoWS/NiWS, regardless of the exact stoichiometries. The catalytic activity can be enhanced by an order of magnitude[73] and the typical concentration of Co or Ni promoter is only 1-5 wt%[74].

Several models were proposed to explain the HDS catalytic activity in terms of the structure-property relation, and corresponding strategies are explored to optimize the performance of the HDS catalysts. The most widely accepted models are:

- *Coordinatively unsaturated sites (CUS):* For the unpromoted HDS catalyst, the catalytically active sites are considered to be the coordinatively unsaturated sites, i.e. molybdenum ions with dangling bonds due to the sulfur vacancies created during a reaction with hydrogen.[65] Such vacancy facilitates the adsorption of the sulfurs from the BTs or DBTs. The CUS are assumed to be more easily formed at the edges and corners of metal sulfides' structure.[65] Therefore it is one of the major reasons for the catalyst industry to reduce the size of the catalyst crystallites, mostly by utilizing support. In this way higher surface area and in turn more exposed edge- and corner sites in micro- or nano-sized catalyst particles can be achieved. Another strategy to increase CUS is to synthesize amorphous catalyst which contains intrinsic coordinatively undersaturated sites.[75,76]
- *Rim-Edge model:* For the unsupported and unpromoted HDS catalyst, the stacking height of the basal planes varies due to the heterogeneous size distributions of the bulk material. The rim-edge model is proposed to explain the catalytic activity and selectivity associated with the stacking number of the basal planes. The basal plane is in general inert. The 'rim' sites which are on the outer regions of the very top and bottom layers favor hydrogenation and breakage of C-S bonds, but the 'edge' sites on the edges of interior layers are only able to cleave C-S bonds.[77] The model is shown in **Figure 2.2**. Accordingly, the unsupported MoS_2 catalyst with higher stacking degree favors DDS pathway owing to more 'edge' sites on the layers, while MoS_2 with lower stacking height would show more HDS selectivity to HYD pathway because the most dominate active sites are the 'rim' sites.

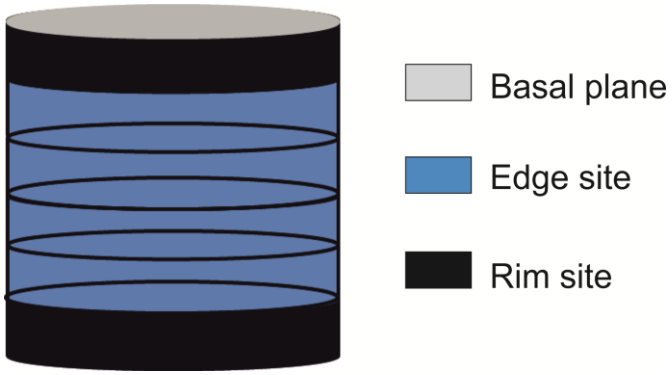

Figure 2.2 *Schematic representation of the Rim-Edge model.*

- *Co-Mo-S (or Ni-Mo-S) phase model:* The main concept of this model is that Co atoms are located on the edges of the MoS_2 layer, substituting Mo atoms.[78,79] This model has been validated by experimental results performed by various analytical methods, e.g. scanning tunneling microscopy (STM), extended X-ray absorption fine structure (EXAFS), and aberration corrected high resolution STEM (HRSTEM). From an electronic point of view, it is believed that the incorporation of the promoter atoms leads to a weakening of the Mo-S bonding, thus to more possibility of sulfur vacancy formation.[65] The promotion effect from the Co or Ni atoms increases the local electron density of sulfur atoms which may help C-S bond cleavage, and indeed, the promoted catalysts showed a preference to DDS pathway.[65]

2.1.3 Relevant Structure of MoS_2

Crystalline MoS_2 is a layered sulfide with three different structural polytypes: 1T (space group: *P*-3*m*1), 2H (space group: $P6_3/mmc$), and 3R (space group: *R*3*m*), where the 'T', 'H', and 'R' indicate the trigonal, hexagonal, and rhombohedral unit cells. The most stable and widely used one is 2H-MoS_2. A representative sketch of the structure of 2H-MoS_2 is illustrated in **Figure 2.3**. Inside each layer of the 2H-MoS_2, one layer of Mo^{4+} cations is 'sandwiched' between two layers of S^{2-} anions. Each Mo^{4+} cation is surrounded by six nearest S^{2-} anions, and the S^{2-} anions occupy the corner positions of a trigonal prism. The trigonal prisms are connected inside the layer via joined edges. The layers are stacked parallel to the c-axis. Between the layers there are van der Waals (vdW) gaps. The characteristic interlayer distance of MoS_2 is 0.615 nm (i.e., d-spacing of the (002) lattice plane). Due to the week van der Waals force between the layers, they can be easily peeled off by simple chemical and/or physical procedures.

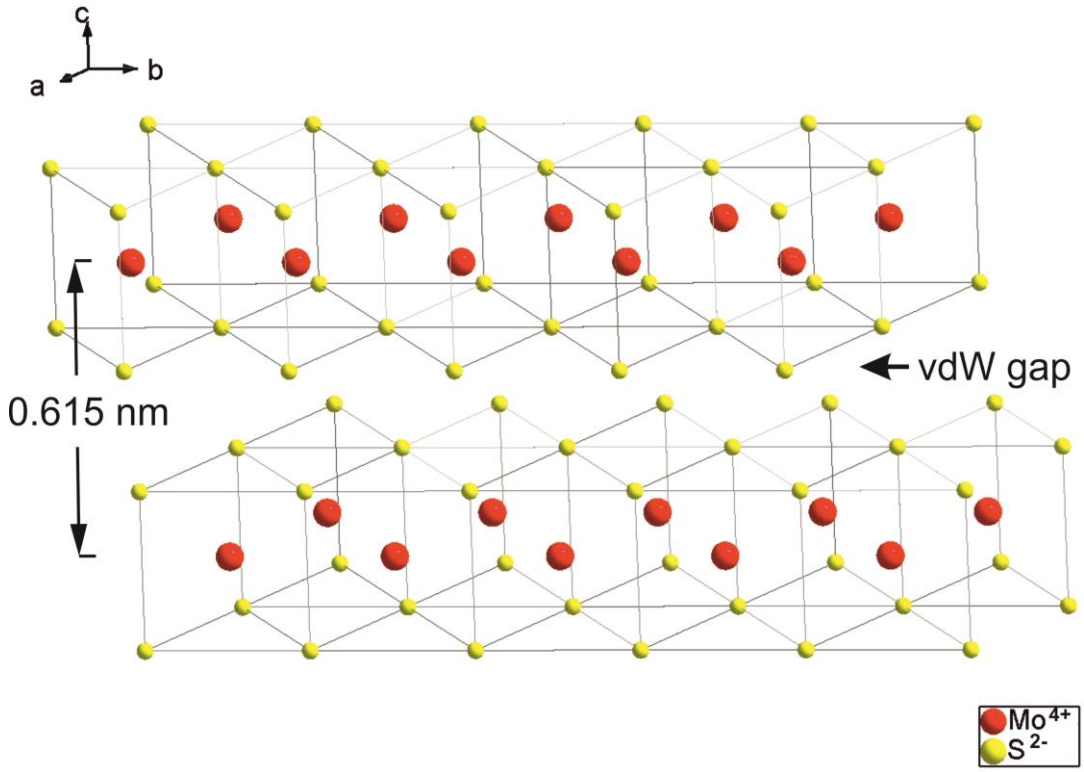

Figure 2.3 *Structure model of 2H-MoS_2.*

1T-MoS_2 is a metastable phase with an octahedral coordination arrangement of the S^{2-} anions around a Mo^{4+} cation. The electronic property of 1T-MoS_2 is reported to be metallic, while 2H-MoS_2 is a semiconductor.[80] The band gap of the semiconducting 2H-MoS_2 widens with decreasing numbers of basal plane stacking.[81] Due to the presence of an intrinsic band gap for 2H-MoS_2, the single sheet material is a good candidate for nanoelectronic devices compared to graphene. Recently the single layer two dimensional transition metal dicolgenides (2D-TMD) are drawing more and more interests due to the fascinating properties of the material when the dimension is reduced to the single atom thickness.[82,83]

2.2 Photocatalyst

Water splitting reaction is considered as a promising approach to obtain hydrogen as a clean and renewable energy to solve nowadays energy and environmental crisis.[3] Therefore, photocatalysts used to facilitate the water splitting reaction have gained increasing research interests.

2.2.1 Photocatalytic Water Splitting

Water splitting reaction can be achieved by a photoreaction including an oxidization-reduction process driven by the energy of light. The entire reaction can be written as:

$$H_2O \rightarrow H_2\,(g) + 0.5\,O_2\,(g)$$

The reaction needs a change of Gibbs free energy of 237 kJ/ mol or 1.23 eV.[3] A simplified scheme of the photocatalysis working principle is shown in **Figure 2.4**: Upon exposure to light, photo generated electron-hole (e^--h^+) pairs are produced in the photocatalyst. The e^--h^+ pairs which survive the recombination process on the defect sites and surface of the catalyst react with the water molecule to reduce the H^+ ions and oxidize the O^{2-} ions. Hereby hydrogen is obtained.

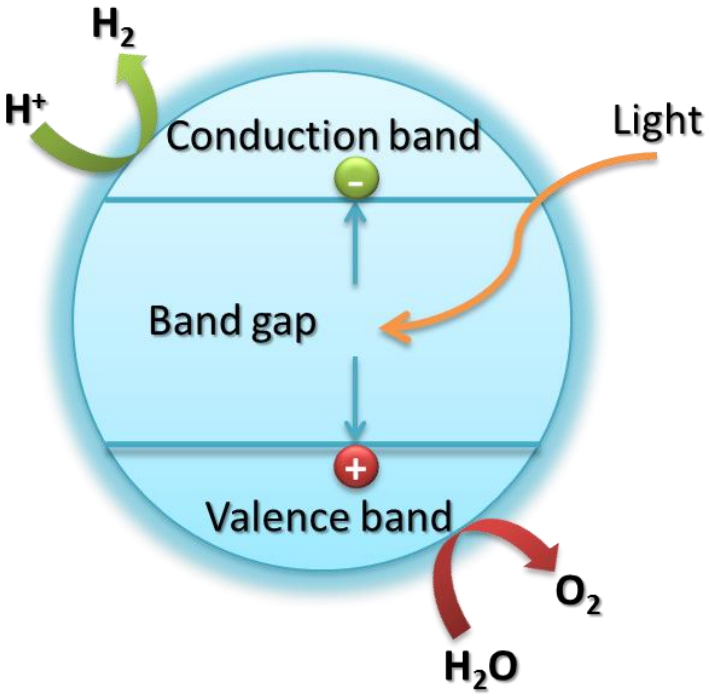

Figure 2.4 *A simplified scheme of the working principle of the photocatalysis process.*

2.2.2 Photocatalyst

In general, semiconductors with a band gap larger than 1.23 eV can act as potential photocatalysts for the water splitting reaction. An upper limit of the band gap is given to efficiently use the solar energy spectrum: the water splitting reaction driven by the visible

light requires a band gap less than 3.0 eV, as the visible light is the major contribution of the solar spectrum. Moreover, beside the basic band structure, several factors affect the hydrogen production from water splitting, e.g. charge separation, carrier mobility, and carrier recombination rate.[3] Nanosized MoS_2 mostly fulfills the aforementioned requirements: it has a tunable band gap in between 1.23 eV and 1.8 eV with decreasing particle size due to the quantum size confinement effect and it can be produced highly crystalline without defects, suppressing the H_2 and O_2 recombination process on the surface.[7] Up to now, nanostructured MoS_2 is a relatively new type of photocatalyst studied more intensively in the last two decades.[7] It has been reported that nano-MoS_2 and its modified variables or composites show promising photocatalytic activity for visible light driven hydrogen production from water splitting.[8, 9, 10, 11]

2.3 Carbon Allotropes and Bonding States

Carbon, as one of the most widely existing and utilized material, has gain increasing research interests due to its versatile properties in different phases and allotropes, especially in micro- and nano-scale. The correlation of its micro- and nano-structure and property is highly demanding to understand and to further optimize the performance of carbon based nanomaterials.

2.3.1 Electronic Configuration of Carbon

The ground state of carbon electronic configuration can be represented as $1s^2 2s^2 2p^2$, with a total of four valence electrons with two electrons each in 2s and 2p subshell. In the excited state, one of the 2s electrons can be promoted into an empty 2p orbital, causing a change in the electronic configuration into $1s^2 2s^1 2p^3$, or more specifically, $1s^2 2s^1 2p_x^1 2p_y^1 2p_z^1$, with $2p_x$, $2p_y$, $2p_z$ as the three sub-orbitals from the 2p shell. In this configuration the 2s and 2p subshells are both half occupied. The excited carbon is capable of forming four covalent bonds which can adopt multiple types, e.g. single, double and triple bonds. These bonds correspond to the sp^3-, sp^2- and sp- hybridization of the 2s and 2p orbitals, respectively. The variety of carbon-carbon bonds is the atomic origin diverse carbon allotropes.[23]

2.3.2 Sp^2- and Sp^3-bonded Carbon Materials

Sp^2- and sp^3-bonded carbon materials present versatile applications in electronic[17,18], mechanical[17, 18], optical and catalyst[84] fields. Typical sp^3-bonded carbon is diamond, where the four equivalent sp^3 orbitals are hybridized from the 2s and $2p_x$, $2p_y$, $2p_z$ sub-orbitals and form four strong σ bonds which adopt a 3-dimentional tetragonal geometry. For the sp^2-bonded carbon materials, the most renowned one is graphite. The three σ bonds (i.e. sp^2-orbitals) are rearranged from the 2s and $2p_x$, $2p_y$ orbitals and located within one plane. The σ plane has a 2-dimentional trigonal geometry. While the remaining $2p_z$ sub-orbital forms a

weak π bond as a second bond of the carbon-carbon double bond. Both the σ and π bonds give rise to the occupied bonding (σ or π) states in the valence band and the empty antibonding (σ* or π*) states in the conduction band.[85]

In EELS analysis (cf. **Section 1.2.1),** the energy differences of transitions from the localized 1s electron to the unoccupied LDOS can be observed via, e.g. 1s→π* and 1s→σ* transitions in carbon give rise to a π* peak and a σ* peak in the spectrum (cf. **Figure 1.2**). The sp^3-bonded carbon materials exhibit no 1s→π* transition due to absence of π bonding and π* antibonding. Hence, this key difference is the foundation of distinguishing sp^2- and sp^3-hybridized carbon atoms. The quantification of the sp^2/sp^3 ratio in carbon materials is further established by evaluating the ratio of the π*/σ* peaks in the EELS spectrum.[25] For amorphous carbon or carbonaceous material, the sp^2/sp^3 ratio is one of the determinate quantities for its property. If the dominate bonding state of carbon is sp^2-hybridized, higher degree of graphitic carbon is present. Amorphous diamond consists of a significant amount of sp^3-bonded carbon without any long-range ordering with similar chemical, electronic and mechanical properties as crystalline diamond.[17] Another key difference appears in EEL spectra of carbon K-edge is the energy shift of the π* and σ* peaks, which is a result of the hybridized orbitals overlap with orbitals from the different neighboring atoms.[25] To conclude, the two determinate features of the carbon edge should be the ratios (i.e. intensity difference) and positions (i.e. energy shift) of the characteristic peaks.

2.4 Metal Oxide Gas Sensor

Semiconducting metal oxide based gas sensors utilize the changes in conductivity of the metal oxide when its surface absorbs certain gas molecules or ions. Depending on the types of semiconductor metal oxides, two major species of gases can be detected: (1) reducing gas (like H_2, H_2S, HCHO, CO and ethanol) which acts as an electron donor when it is absorbed on n-type semiconductors (e.g. ZnO, SnO_2, TiO_2, In_2O_3, Ga_2O_3, WO_3 and MoO_3), and (2) oxidizing gas (for example: O_2, NO_2, Cl_2, F_2 and HF) as an electron acceptor on the surface of p-type metal oxides (e.g. CuO, NiO and TeO_2).[86,87]

2.4.1 Sensitivity of Gas Sensor

The performance of a gas sensor is described by sensitivity, selectivity, response time, recovery time and operation temperature etc. Sensitivity of a gas sensor (S) is the most important parameter, which is the ratio of the resistance of the sensor in ambient air (R_a) over that in the target gas (R_g):

$$S = R_a / R_g.$$

Nanostructured especially one dimensional metal oxides are found to be of advantageous performance as gas sensors, mainly due to their high aspect ratio, large specific surface area and lower operation temperature. Furthermore, gas sensors manufactured with metal oxide composite are considered to have a better gas response owing to the synergistic effect and/or heterojunction interface between two different oxide components.[88]

2.4.2 Relevant Structure of Sample Materials: α-MoO_3

α-MoO_3 is an n-type semiconductor which exhibits good gas response towards several gases, such as O_2[89], NO_2[90] and ethanol[91]. Crystalline α-MoO_3 (space group *Pbnm*) has a layered morphology as shown in **Figure 2.5**. The layers are alternatively stacked along the crystallographic b-axis via van der Waals interaction. Each layer is composed of two sublayers formed by [MoO_6] octahedra via joined corners along the *a*-axis (see **Figure 2.5**(a)), and edge-sharing along the *c*-axis (see **Figure 2.5** (b)). Furthermore, the projection of the basal plane along the *b*-axis can be represented as a corner-sharing network which is characteristic of the α-MoO_3 structure (see **Figure 2.5**(c)).

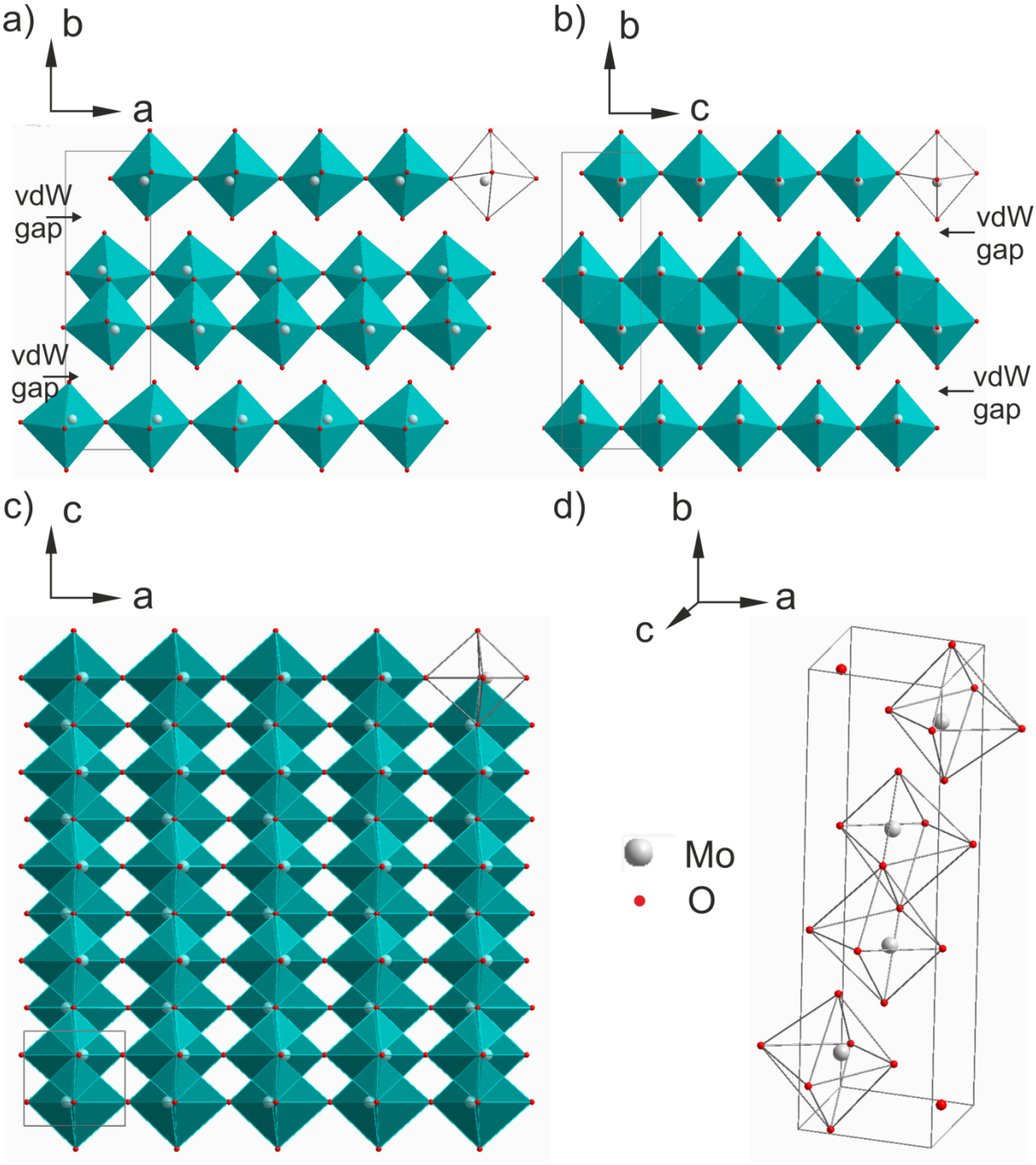

Figure 2.5 *Structure model of α-MoO_3: (a) Arrangement of [MoO_6] polyhedra along the a axis, unit cell and the van del Waals gap are shown. (b) Arrangement of [MoO_6] polyhedra along the c axis. (c) Projection along b axis showing the [MoO_6] polyhedra share common corners in the (010) plane. (d) [MoO_6] octahedra inside one unit cell, indicating a coordination number of six for a molybdenum atom. (Adapted with permission from ref. 91. Copyright (2014) American Chemical Society.)*

Results and Discussion

3 MoS_2-based Catalysts

In this chapter, MoS_2 and its composite materials are characterized via various TEM techniques. Their catalytic activities, e.g. photocatalytic and HDS catalytic activities are discussed in correlation with their structural property. Furthermore, the structural evolutions of the catalysts with respect to external stimuli are visualized *in situ* inside TEM up to atomic resolution.

3.1 MoS_2-based Inorganic-Organic Nanocomposite ($MoS_xC_yP_z$) as Photocatalyst

Conventional TEM study is first carried out to analyze the chemical and structural properties of two MoS_2-based nanocomposite samples ($MoS_xC_yP_z$) decomposed at 250 °C and 350 °C, respectively. *In situ* TEM investigation sheds light on the structural stability of the $MoS_xC_yP_z$ composite sample. Furthermore, EELS studies on the carbon species within the specimen give insight into the chemical bonding states of the incorporated phases in the MoS_2 based composite. The photocatalytic activities of the $MoS_xC_yP_z$ are discussed in comparison with that of bulk MoS_2 material.

3.1.1 TEM investigation

First structural investigations were performed on the samples decomposed at 250 °C and 350 °C to gain morphology and crystallinity information. Representative HRTEM micrographs of the 250 °C sample are shown in **Figure 3.1**. The samples are poorly crystalline with short range ordered slab structures. The slab-like contrast of the structure on the micrographs originates from the basal planes of MoS_2. In FFT pattern two faint intensity rings can be assigned to the (002) and (101) planes of MoS_2. Moreover, an additional reflection with a d-value of 1.36 nm is revealed which cannot be assigned to any lattice spacing of MoS_2 (**Figure 3.1** (a)). To better resolve the additional slabs in the real space, Bragg filtering was applied only on the additional rings in the FFT to obtain the inverse FFT (IFFT) image (**Figure 3.1**(b)). The IFFT of the marked region in **Figure 3.1**(a) displays the strong contrast arising from slabs with expanded d-spacings ranging from 1.32 nm to 1.36 nm.

In contrast, the additional d-spacing is not present in the 350 °C sample neither in the HRTEM micrograph (**Figure 3.1**(c)) nor in the FFT pattern (**Figure 3.1**(d)). The diffuse 002 ring from the FFT pattern indicates a disordered and expanded (002) planes, which is observable from the HRTEM micrograph. These findings are confirmed via XRD performed by *John Djamil*. However, the additional d-spacing observed in the 250 °C sample in XRD is about 0.2 nm larger than the one from TEM. The deviation might be rationalized by electron beam modification introduced to the sample, e.g. by knocking out intercalated molecules serving for decrease of layer spacing in TEM. The electron beam modification to the 250 °C sample is indeed observed *in situ*, see **Section 3.1.2**. Further studies via nuclear magnetic resonance spectroscopy (NMR), infrared spectroscopy (IR) and XRD simulation by *John Djamil* suggested an intercalation of Ph_3PS and $(Ph_4P)_2S$ organic molecules in between the (002) planes of MoS_2, causing the expanded structure in the 250 °C sample.

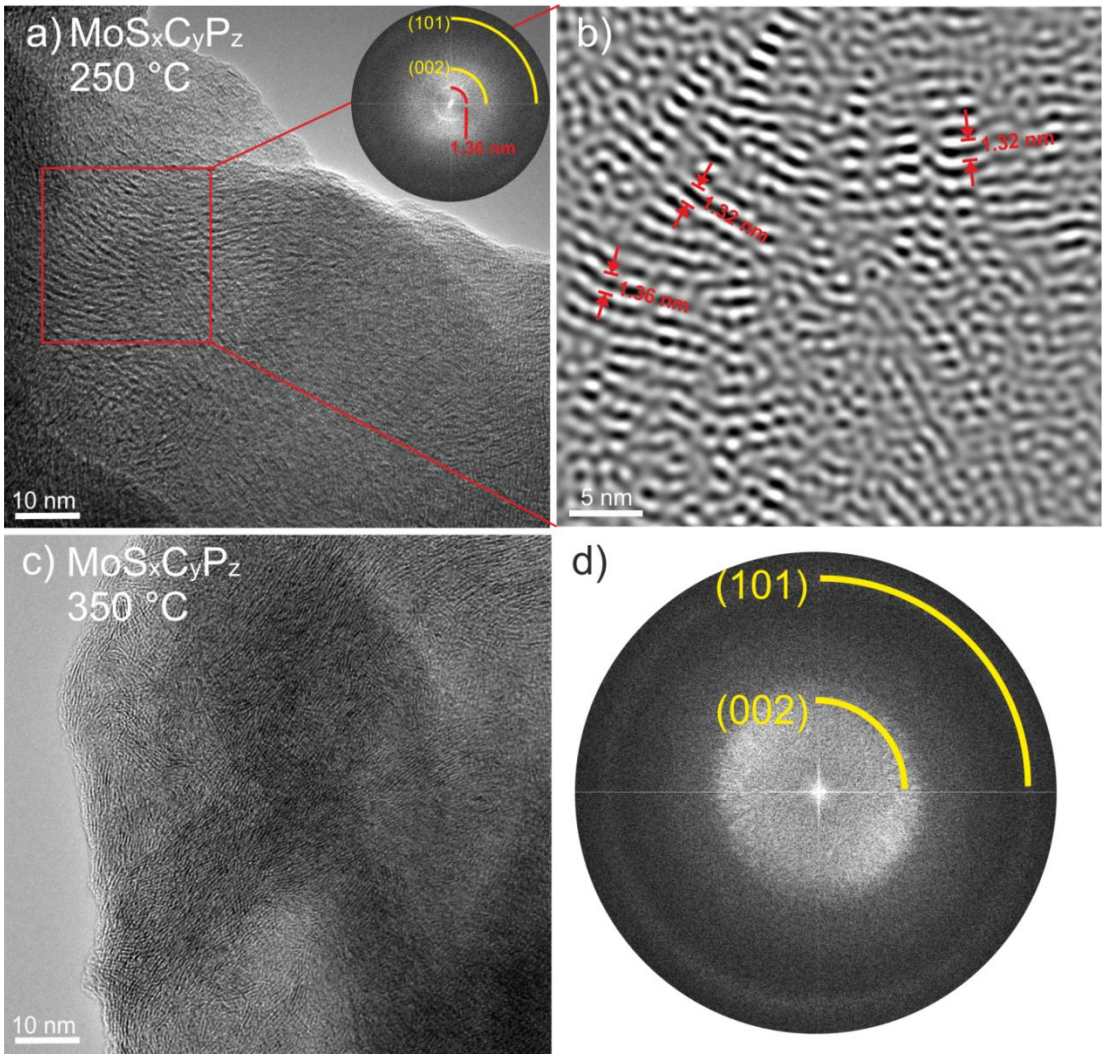

Figure 3.1 *(a) HRTEM micrograph of the 250 °C sample with a corresponding FFT pattern in the inset. (b) Enlarged inverse FFT of the squared area in (a) indicating the additional d-spacings (red arrows). (c) HRTEM micrograph of the 350 °C sample with (d) the corresponding FFT. In the FFT pattern the diffuse rings correspond to the (002) and (101) planes of MoS_2. No additional d-spacing is identified in 350 °C sample. (Adapted from ref. 92. Copyright of John Wiley and Sons.)*

3.1.2 *In situ* Transformation under Electron Beam Irradiation

The structural stability of the intercalated composite sample is analyzed *in situ* in TEM. Before electron beam irradiation, the FFT pattern indicates the characteristic 002, 101 intensity rings and the expanded planes with a d-spacing 1.36 nm (**Figure 3.2**(a)). Furthermore, the expanded d-spacings are better resolved in the IFFT image (arrows in **Figure 3.2**(c)). After 1~2 minutes of exposure to the electron beam (acceleration voltage: 300 kV, extraction voltage: 4400 V, beam charge density on the specimen: ~nA · s/cm^2), the expanded slabs disappears in the irradiated region, leaving only diffuse 002 intensities (FFT pattern in **Figure 3.2**(b)). The same IFFT mask is applied to the FFT pattern from the HRTEM micrograph after beam irradiation. No indications for the expanded slabs can be traced in the IFFT (**Figure 3.2**(d)).

The comparison before and after the electron beam irradiation suggests the incorporated compounds in between the layers of MoS_2 is unstable under *in situ* conditions. The knock-on effect may be the dominated driving force to modify the structure of the 250 °C sample, i.e. the incorporated molecules in the MoS_2 slabs undergoes an elastic interaction where electron beam hits them out.

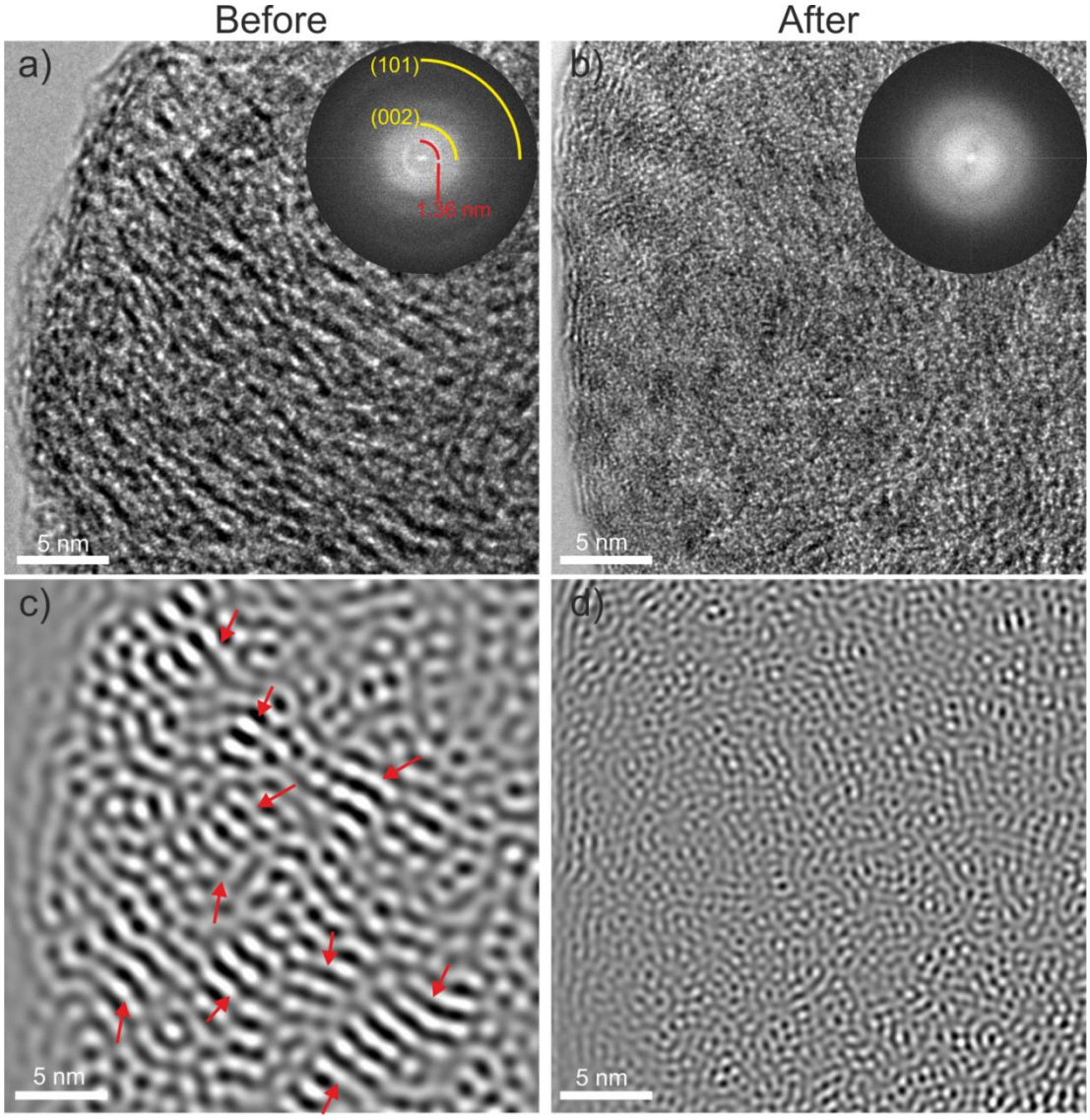

Figure 3.2 *In situ electron beam irradiation of the 250 °C sample in TEM. (a) HRTEM micrograph before irradiation with a corresponding FFT pattern in the inset. The expanded d-value of the 002 intensity ring is indicated by a red ring. (b) HRTEM micrograph and corresponding FFT pattern after irradiation. (c) IFFT image filtered from the HRTEM micrograph in (a). Red arrows assign the expanded slabs. (d) IFFT image obtained from the HRTEM micrograph in (b). The expanded slabs vanished after irradiation.*

3.1.3 EELS Study of the Carbon species in $MoS_xC_yP_z$

The carbon species in the intercalated $MoS_xC_yP_z$ composite are investigated by EELS. The spectra from different positions of the sample are labeled as P1, P2 and P3, respectively (**Figure 3.3**). A reference spectrum was obtained from the amorphous lacey carbon film on the TEM sample grid (labeled as LC).

A comparison of the EEL spectra of the carbon K ionization edge from different regions of the sample and from the reference amorphous lacey carbon is depicted in **Figure 3.3**(a). The carbon K-edge has an onset at ~ 284 eV, and consists of two characteristic features: the π* peak starting from 284 eV and the σ* peak ranging from 290~310 eV. The π* peak represents the transition of the electrons in carbon from the 1s state to the π* conduction band, while the σ* peak originates from the transition of 1s → σ* conduction band. The positions and ratio of the maxima of the π* and σ* peak indicate different carbon species inside the sample. The EEL spectra of the three regions demonstrate a more pronounced π* peak, and a σ* peak with more fine structures as compared to the lacey carbon. The maxima of the σ* peak all appear before 300 eV (arrows in **Figure 3.3**), indicating a graphitic feature of carbon bonding within the sample.[93, ii]

In comparison, the EEL spectrum of the lacey carbon reference exhibits a featureless σ* peak, suggesting an amorphous carbon structure. The calculation of the π* and σ* peak ratios exhibits a higher value in each case from the composite sample (P1: 0.70, P2: 0.64, P3: 0.55) with respect to the lacey carbon reference (0.41) (**Figure 3.3**(b)). This finding indicates a graphitic carbon state potentially stemming from intercalated aromatic carbon rings with more crystalline and ordered structure in the composite.[94,95]

NMR and IR spectroscopy further performed by John Djamil confirm the incorporation of the aromatic carbon rings (phenyl groups) in between the MoS_2 layer. The sp^2 hybridization of the bonding on the carbon ring might be most probably the origin of the graphitic feature, i.e. a more prominent π* peak, detected via EELS.

The reproducibility of the EEL spectrometer has been demonstrated in **Figure 1.4**. Therefore, the differences of the EEL spectra present in the same sample can be assigned to the inhomogeneity of the sample. The varying sample thickness can introduce complex plural scattering, hence induces oscillations of the spectrum. Additionally, the non-uniform crystallinity of the composite sample will result in different coordination environments and

[ii] For a detailed comparison of the fine structure of the C-K edge between a graphitic carbon and a carbidic carbon, please refer to the discussion in section 3.5 in this thesis.

local structures of carbon atoms. It will lead to diverse ELNES fingerprints in the near edge region. Besides the varying intrinsic features of the sample, the modification introduced by electron beam can result in differences in the EEL spectra within the same sample. Beam sensitivity of the carbon species should be taken into account, which is further discussed in **Section 5.1**. However, by utilizing the same acceleration voltage and acquisition time, the modification by the beam at each position can be considered the same, and thus can be neglected when the spectra are compared under the same experimental setups. Despite of differences stemming from both the intrinsic and extrinsic factors, the most determinate features of the carbon edge are discussed in **Section 2.3.2**, and they should be the positions and ratios of the characteristic peaks, especially the onset of the π* peak in the C-K edge.

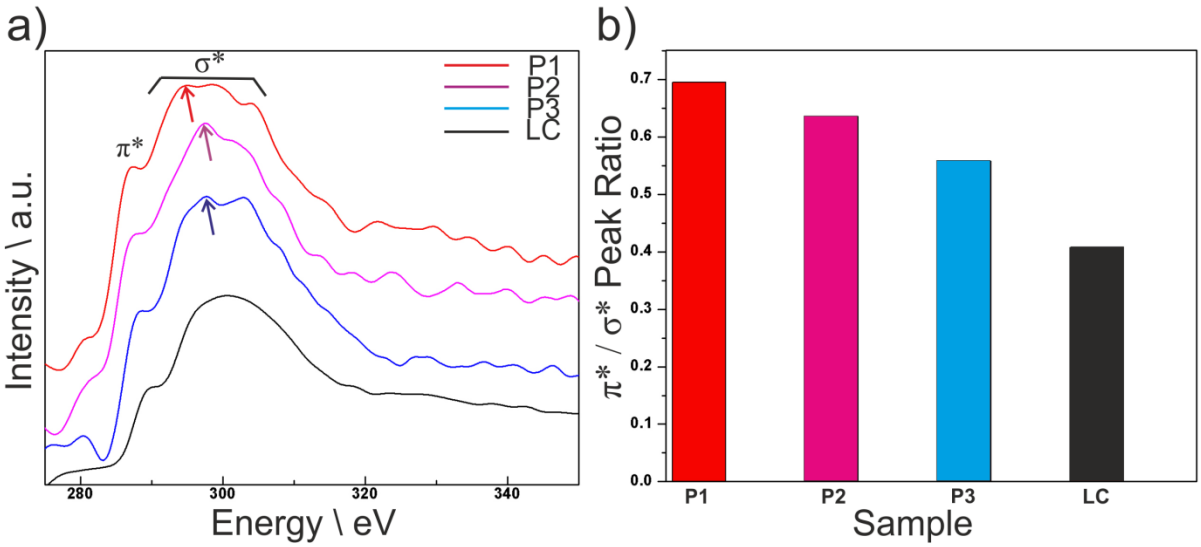

Figure 3.3 *(a) ELL spectra recorded on the 250 °C $MoS_xC_yP_z$ composite sample at different regions (P1: red curve, P2: purple curve, P3: blue curve) and at a reference region in amorphous lacy carbon film (LC: black curve). The energy loss region of the π* and the σ* peaks are indicated. The maxima of the σ* peaks from the sample are marked out with arrows. (b) The π* / σ* peak ratios of the composite sample and of the lacy carbon determined from the corresponding spectra in (a).*

3.1.4 Photocatalytic Activity of $MoS_xC_yP_z$

The visible light driven hydrogen production experiments in water were carried out as described in **Section 1.3.4**. The results of the reaction demonstrate that both 250 °C (≈ 230 µmol /14 h) and 350 °C (≈ 320 µmol /14 h) $MoS_xC_yP_z$ composites are much more active than the bulk MoS_2 (≈ 30 µmol /14 h) (cf. **Figure 3.4**). The 350 °C sample exhibits the highest photocatalytic activity. The differences in catalytic performance can be attributed to the different chemical and structural properties of the samples. The 250 °C sample is intercalated with organic molecules in between the MoS_2 slabs with carbon species of graphitic nature. The graphitic carbon might be theoretically suppressing charge recombination, improving carriers transfer and enhancing light adsorption properties as well as the amount of photocatalytic reaction centers as it has been observed by other studies.[96, 97] The intercalation of phosphorus species may facilitate the catalytic activity.[98] However, the

bonding of Ph_3PS to Mo atoms of the molybdenum sulfide might block active sites for hydrogen generation, thus compromising the photocatalytic performance as compared to the 350 °C sample. While on the other hand, the 350 °C $MoS_xC_yP_z$ composite sample has less intercalation with carbon, hydrogen nor phosphorous molecules. Moreover, the results from XRD and Raman spectroscopy of the 350 °C sample show a lower stacking degree of disordered/defective MoS_2 slabs than the 250 °C sample, inferring more edge-sites in the MoS_2 slabs which promote the photocatalytic activity.

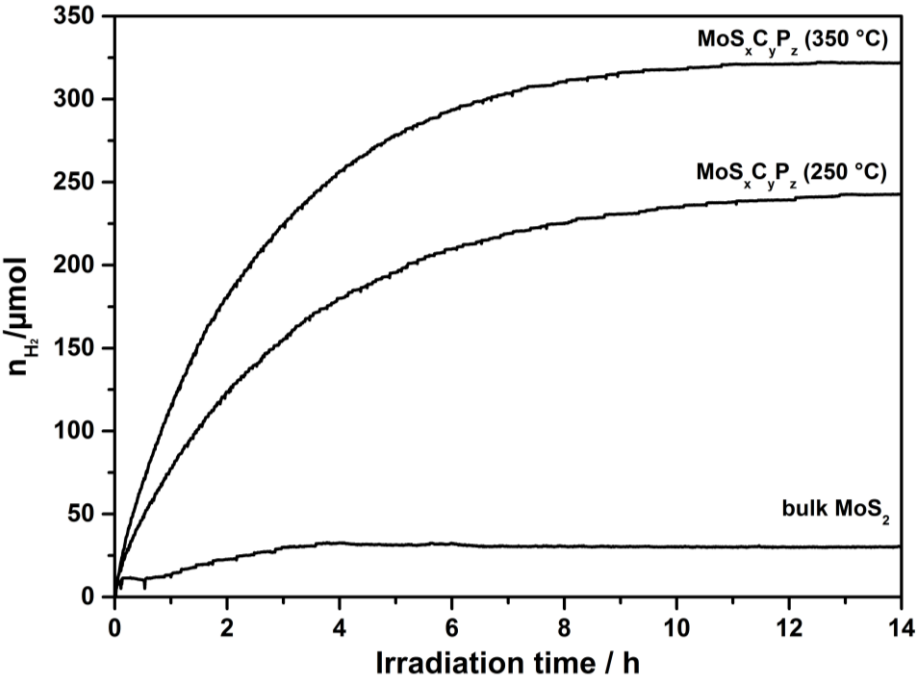

Figure 3.4 *Kinetic studies of the photocatalytic hydrogen production reaction from a mixture containing triethylamine (8 mL), water (3 mL) and $[Ru(bpy)_3](PF_6)_2$ in acetonitrile (10 mL).The MoS2 composite sample prepared at 350 °C shows an enhanced photocatalytic activity. Measurement performed by John Djamil.*

3.2 Amorphous MoS_2 (PX) as Photocatalyst

In this part, structural analysis is performed and crystallization phenomena are subsequently studied during *in situ* electron beam irradiation and *in situ* annealing experiments for amorphous MoS_2 (PX) sample inside TEM.

3.2.1 *In situ* Electron Beam Irradiation inside TEM

Fundamental investigations of the microstructure are performed by HRTEM and associated FFT on the PX sample before *in situ* electron beam irradiation. The result confirms an almost amorphous structure of the sample with only an indication of the faint 011 intensity ring, as shown in **Figure 3.5**(a).

In addition, an *in situ* irradiation experiment is conducted on the pristine PX sample with an equivalent setting of the incoming electron beam as indicated in Section **3.1.2.** The structure evolution of a particle of the PX sample with respect to the irradiation time is presented in **Figure 3.5**. The characteristic (002) single slabs of crystalline MoS_2 exhibit first sign of formation after an exposure of several minutes to the electron beam (**Figure 3.5**(b)). Long-term irradiation experiments shows increased stacking height and slab length with extended exposure times up to 1 h (see **Figure 3.5**(c) and (f)). A closer examination of the FFTs of **Figure 3.5**(e) and (f) reveals increasing ordering of (011), (013), and (-120) lattice planes under the electron beam irradiation. The literature[99] and experimentally obtained d-spacings of the assigned lattice planes are (002): 0.615 nm|0.64 nm, (011): 0.267 nm|0.26 nm, (013): 0.228 nm|0.22 nm, (-120): 0.158 nm|0.16 nm, respectively. The 002 d-spacing is much larger than the literature one, indicating a bended and disordered arrangement of the *in situ* formed planes, as it is confirmed by the HRTEM micrograph (**Figure 3.5**(c)).

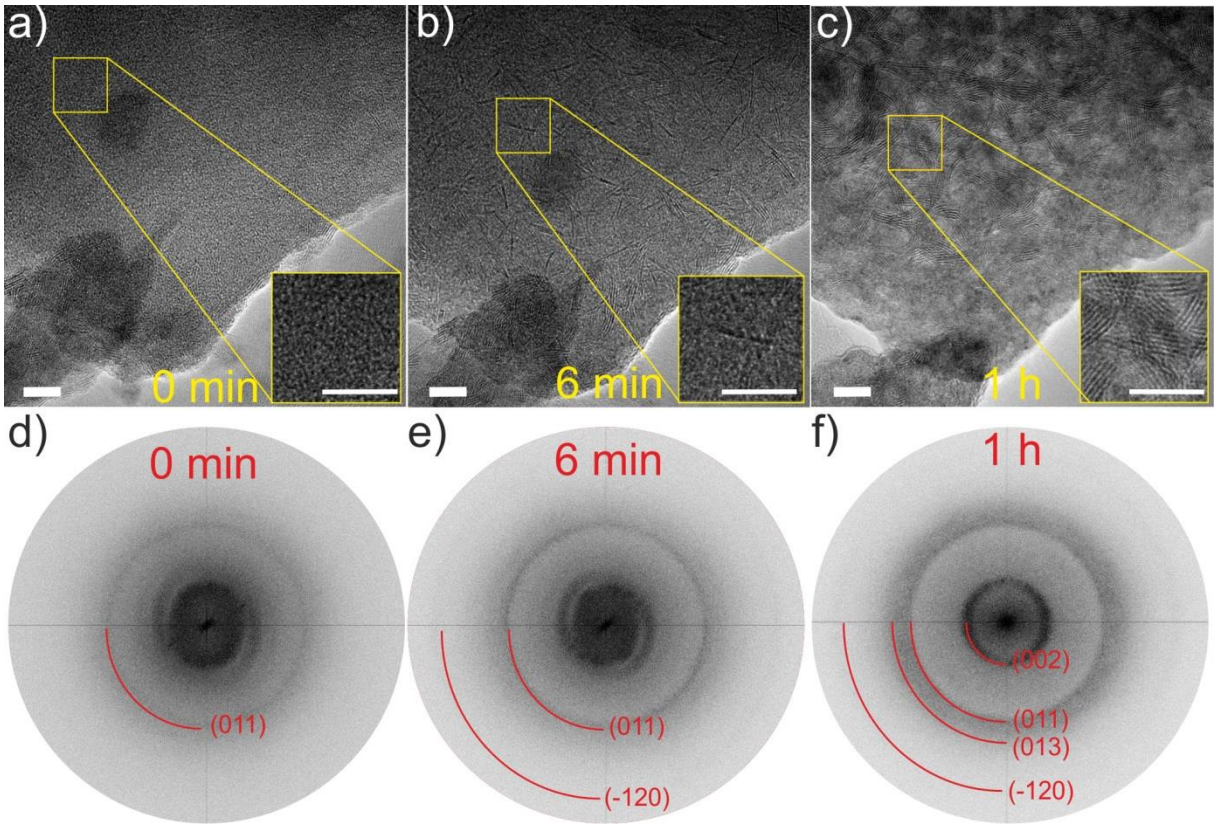

Figure 3.5 *Time resolved series of HRTEM micrographs of a representative particle of the PX sample showing the evolution of the crystallographic structure under electron beam irradiation for (a) 0 min, (b) 6 min, (c) 1 h, and the corresponding FFT patterns (d), (e) and (f). Insets show enlarged areas of the growth of (002) slabs in the same position of the bulk particle. Scale bar is 10 nm.*

3.2.2 *In situ* Heating in TEM (by a Heating Stage)

To study the crystallization process of the PX sample under a thermal annealing procedure, an *in situ* heating experiment was conducted while applying a lower dose of electrons by *Dr. Andriy Lotnyk*. The findings reveal an increase in crystallinity of the as prepared PX as the temperature rises. Overviews of TEM bright field images from the same location of a sample particle are illustrated in **Figure 3.6** from 300 °C to 500 °C. By applying an IFFT calculation, the evolution of the (002) slabs of crystalline MoS_2 is emphasized (see **Figure 3.6**(c), (f), (i), and (l)). The mask has a spatial frequency range from 2.35 to 7.50 nm^{-1}, exhibiting exclusively the MoS_2 lattice planes with d-values from 0.267 nm to 0.85 nm in real space.

Up to 300 °C, the sample remains in an amorphous state (see **Figure 3.6**(c) and confirms the observation in **Figure 3.5**(a)). Starting from 350 °C the first indications of (002) slab development can be detected (**Figure 3.6**(f)). The measured spacing of the slabs (0.63 nm) is similar to that formed under electron beam irradiation (0.64 nm). Furthermore, XRD result from an *ex situ* heating experiment of the PX sample performed by *Felix Niefind* suggested that a formation of (002) planes starts at a temperature lower than 450 °C (see **Section 3.2.4**). At 450 °C and 500 °C, the stacking number and the length of the slabs further increase

(**Figure 3.6**(i) and (l)). They are developing into a more ordered stacking structure, suggesting an increase of crystallinity of the PX sample upon heating.

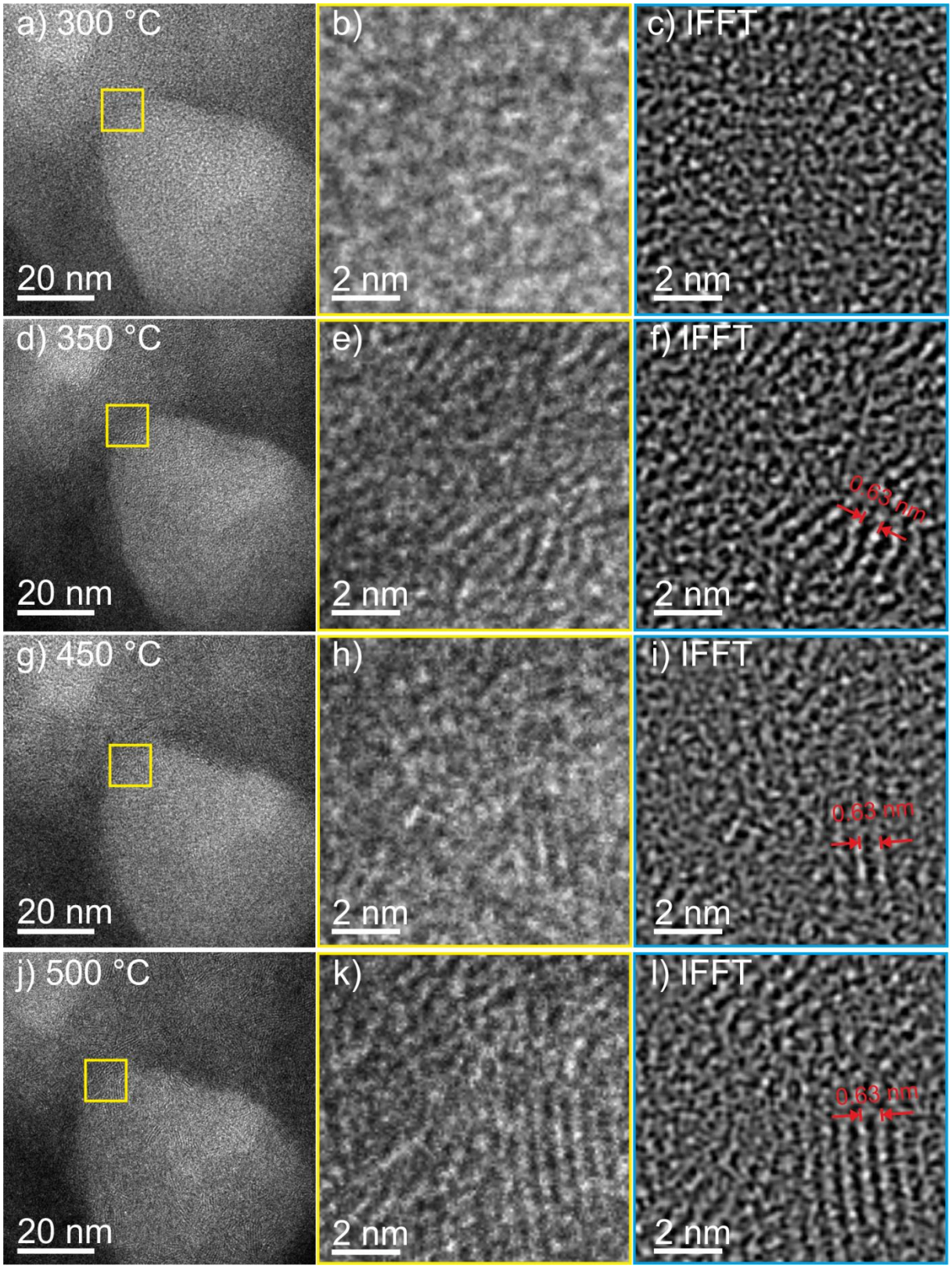

Figure 3.6 *Temperature resolved series of TEM bright-field images of the as prepared PX sample during the in situ heating experiment at a temperature of: (a) 300 °C, (d) 350 °C, (g) 400 °C, and (j) 450 °C. (b), (e), (h), and (k): Magnified view on the development of (002) slabs from the same region*

(marked with a red square) of the sample. (c), (f), (i) and (l): corresponding IFFTs with an enhance view on the characteristic (002) slabs of MoS_2. The measured d-spacing of the slabs is 0.63 nm.

3.2.3 Different Crystallization Mechanisms Implied by *in situ* Irradiation and Heating of PX

By comparing the experimental results of the in situ electron beam irradiation and in situ heating inside TEM, there are some noticeable differences between the two crystallization processes. The stacking numbers and the length of the (002) slabs formed under the in situ electron beam irradiation for 1 h are more heterogeneous, signifying an evolution of different particle sizes of the MoS_2 grains under the two pathways. A size distribution histogram determined after in situ irradiation for 1 h is more broadened, with a most possible stacking number of 5 and a longer basal plane length of ~4 to 5 nm (**Figure 3.7**(red cylinders)). In contrast, the grain sizes are more uniform for the in situ heating of the PX up to 500 °C (**Figure 3.7**(blue cylinders)). The histogram for the in situ annealing up to 500 °C shows a narrower distribution, with a most frequently observed stacking number of 4 basal planes, and a plane length of 2 nm. These values are in good agreement with those determined from the XRD data of the sample *ex situ* heated to 450 °C (see **Section 3.2.4**).

Apparently, different mechanisms are present in the two *in situ* crystallization procedures within nano-sized materials.[100] In the case of *in situ* irradiation, the inelastic interaction between the localized electron beam and the specimen produces highly concentrated heating in the sample particles as compared to the *in situ* heating.[100] The beam heating can be especially significant when the thermal conductivity of the specimen is relatively low and cannot well dissipate the thermal energy.[100] In the case of monolayer MoS_2 or amorphous MoS_2, which is the dominant phase in the PX sample with lower thermal conductivity[101], the highly confined beam heating is likely to occur inside the PX particles, leading to an anisotropic thermal energy distribution to activate the crystallization of MoS_2 slabs. In other words, the pre-existing MoS_2 single or multiple slabs can serve as crystallization seeds and be heated preferably due to the heat confinement between the slabs and the amorphous matrix. Furthermore the heating is uniform due to the low thermal conductivity of the matrix. Therefore, a broader size distribution of the MoS_2 crystallites can be produced. While in the thermal annealing process, a better thermal conductivity of the carbon lacey network created a more uniform heat distribution over the whole sample grid, thus more uniform sizes of MoS_2 particles was generated.[100]

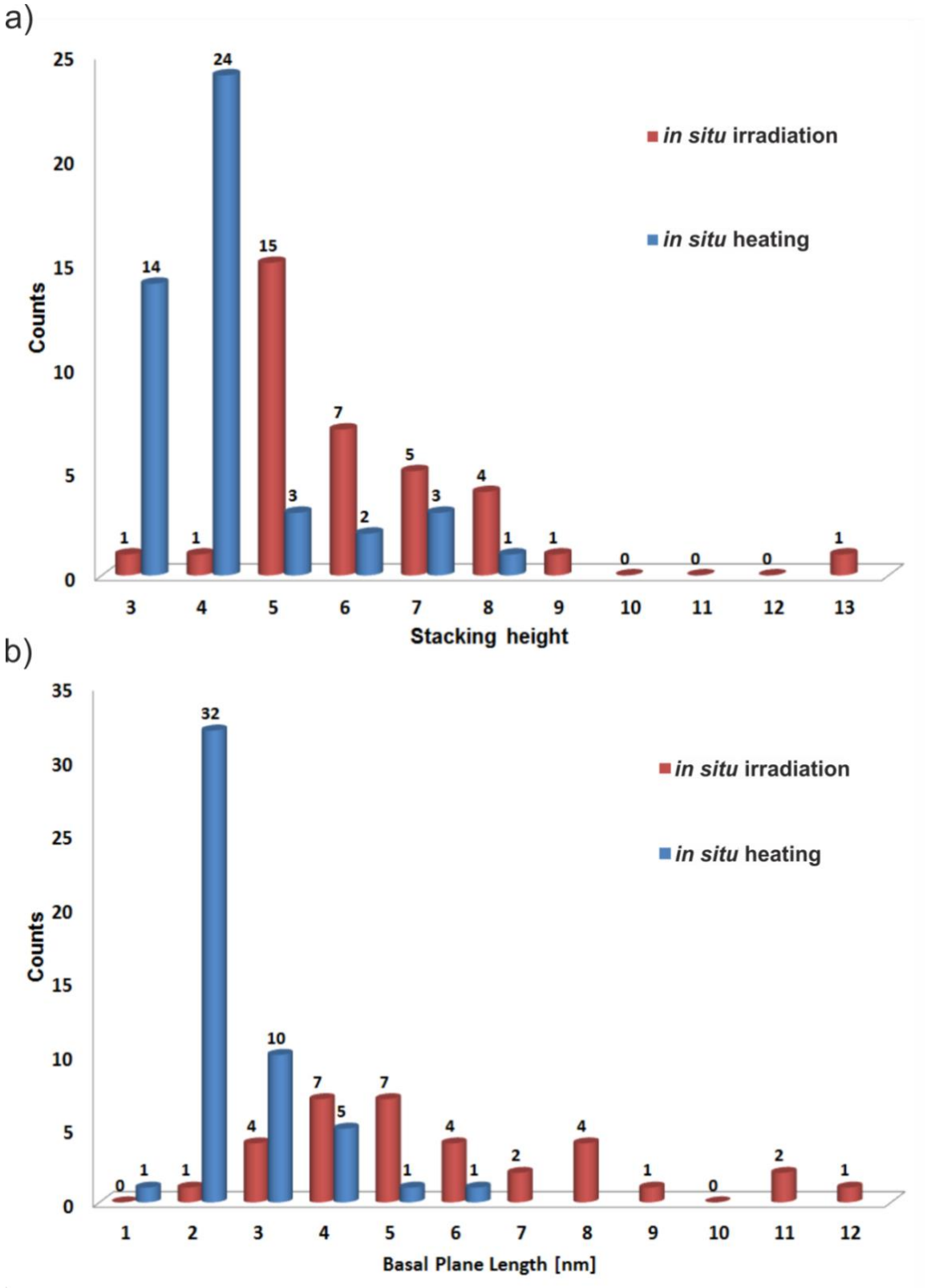

Figure 3.7 *(a) The stacking height distribution determined from the HRTEM micrograph* ***Figure 3.5****(c) (in situ electron irradiation for 1 h: red cylinders), and from* ***Figure 3.6****(f)(in situ heating to 500 °C: blue cylinders). (b) The length distribution of the basal plane of the formed MoS_2 after in situ electron irradiation (red cylinders) and after in situ heating (blue cylinders).*

3.2.4 *Ex situ* Heating of PX

Ex situ heating experiments of the PX sample were carried out by *Felix Niefind*. Two PX samples were heated to 450 °C and 900 °C (labelled as PX450 and PX900) respectively. Additionally a commercially available bulk MoS_2 is studied as a comparison.

The green diffractogram of the as prepared PX indicates an amorphous nature of the sample, because no clear reflections can be identified, which supports the aforementioned HRTEM/FFT investigation as depicted in **Figure 3.5**(a) and (d).

Similar to the *in situ* heating of the PX sample in TEM, nucleation and crystallization of a layered MoS_2 started after heating at 450 °C in the ex situ heating process. The (002) d-spacing is determined to be 0.660 nm from the 2θ angle of the 002 reflection in the XRD diffractogram which is larger than that determined by the FFT pattern from TEM analysis (0.637 nm). The discrepancy might be owing to the fact that the fast electron beam knocks out impurities between the layers and thus a decreased interlayer distance was observed. A calculation based on the Scherrer formula[102] suggested a size of coherently scattering domains of 2.67 nm, and in turn a stacking number of 4 for the MoS_2 basal planes, which are consistent with the histogram obtained from *in situ* TEM heating (cf. **Figure 3.7**). However, the stacking number estimated by XRD was based on the Debye-Scherrer equation which is applied to the 002 reflection. This estimation can be slightly larger than the value determined via TEM, because the monolayers are neglected.[6] A more crystalline sample was obtained by *ex situ* heating at 900 °C. The size of coherently scattering domains is determined to be about 10.8 nm, corresponding to an average of 17 stacked MoS_2 basal planes.

Both localized, the high spatial resolved study (*in situ* TEM) and statistical, averaged analysis (*ex situ* XRD) confirm the structure evolution of the PX under annealing or electron irradiation, thus, it can be speculated that a controlled crystallization of the PX can be manipulated by varying the external stimuli, and even single slabs of MoS_2 can be produced for further applications.

3.2.5 Photocatalytic Activity of PX

The visible light driven hydrogen production experiments in water were carried out in the same experimental setup as described in **Section 1.3.4**. The photocatalytic activity of the PX sample is described by the total amount of the produced hydrogen gas with respect to the time of light illumination. The comparison of the catalysts activity for PX, PX450, PX900, MoS_2 obtained by thermal decomposition of ATM and commercial bulk MoS_2 is is illustrated in **Figure 3.8**. The as prepared PX sample shows the highest activity (≈350 µmol/14 h), the MoS_2 sample thermally decomposed from ATM at 350 °C (≈280 µmol/14h) is fairly good for the hydrogen production, while the heated PX samples (PX450: ≈100 µmol/14h and PX900: ≈50 µmol/14h) exhibit much lower activity. Bulk MoS_2 has the lowest catalytic activity (≈30 µmol/14h). Additionally, a comparison of the photocatalytic activity with other materials

form literatures demonstrates that the as prepared PX is a promising candidate for the visible light driven water splitting process.[103]

The charge separation and migration of the carriers to the surface is believed to be affected by the crystallinity, defects and particle size of the catalyst strongly. [104,105] Thus, the structural factors in turn influence the activity of the photocatalyst for the visible light driven water splitting reaction.[104,105] However, when the particle size of the catalyst decreases down to the nanometer or amorphous scale, the situations can be completely different. The amorphous catalyst with the highest hydrogen production rate might be due to the presence of more coordinatively unsaturated sites which can serve as catalytically active sites.[75] Further XPS results done by *Felix Niefind* show Mo-N binding detected in the pristine sample vanish after heated to 450 °C. This observation could suggest that the Mo-N sites are possibly catalytic active sites.

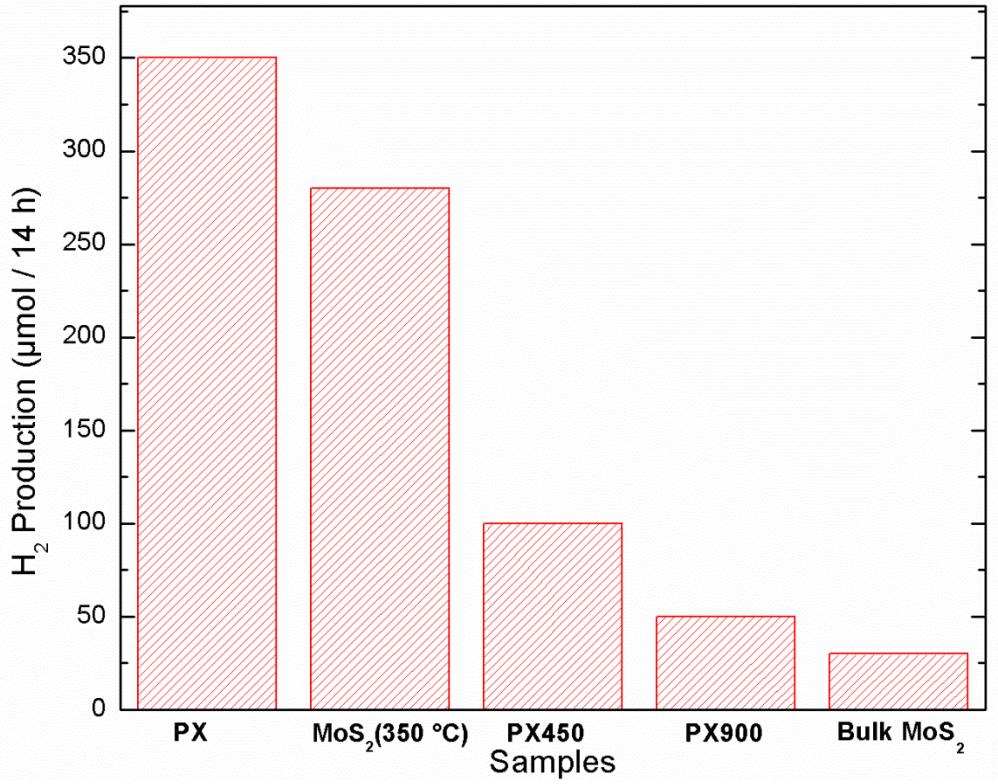

Figure 3.8 *Photocatalytic hydrogen production reaction from a mixture containing a sacrificial electron donor triethylamine (8 mL), water (3 mL) and a photosensitizer $[Ru(bpy)_3](PF_6)_2$ (1 mM) in acetonitrile (10 mL). The y-axis denotes the total amount of the produced hydrogen gas within the 14 h reaction time. The results of PX as obtained, a MoS_2 sample thermally decomposed from ATM at 350 °C, PX heated to 450 °C (PX450), PX heated to 900 °C (PX900), and bulk MoS_2, are shown. Measurement performed by Felix Niefind.*

3.3 Amorphous MoS_2 (PX) / Co as HDS Catalyst

In the following sections, the HDS selectivity and catalytic activity of the samples prepared in different conditions are discussed. Then qualitative and quantitative TEM structural analyses are carried out to study the structural-property correlations of the as prepared samples.

3.3.1 HDS Catalytic Activity and Selectivity of the PXCo Catalysts

The HDS catalytic conversion rate and selectivity of the as prepared PXCo catalyst are determined according to the methods introduced in **Section 1.3.4**. As shown in **Figure 3.9**, the catalysts PXCo1, PXCo2 and PXCo3 (synthesized in forming gas) exhibit higher conversion rates than PXCo4, PXCo5 and PXCo6 (formed in nitrogen), except that PXCo6 shows a larger conversion rate (42%). The rate constants of the catalysts prepared in N_2 increase with elevated activation temperature (PXCo4 → PXCo5 → PXCo6). While an opposite trend is observed for the catalysts activated in forming gas, i.e. the conversion rate decreases with increasing activation temperature for catalysts PXCo1 and PXCo2.

Moreover, the significant difference in selectivity of the two series of catalysts and a change of activity of the samples is observed during HDS reaction. As it can be concluded from **Figure 3.9**, the catalysts formed in forming gas show a strong preference to the DDS pathway (S_{HYD} / S_{DDS} ~ 0.3), while the samples activated in nitrogen atmosphere are more favorable for the HYD pathway (S_{HYD} / S_{DDS} = 0.70 ~ 0.85).

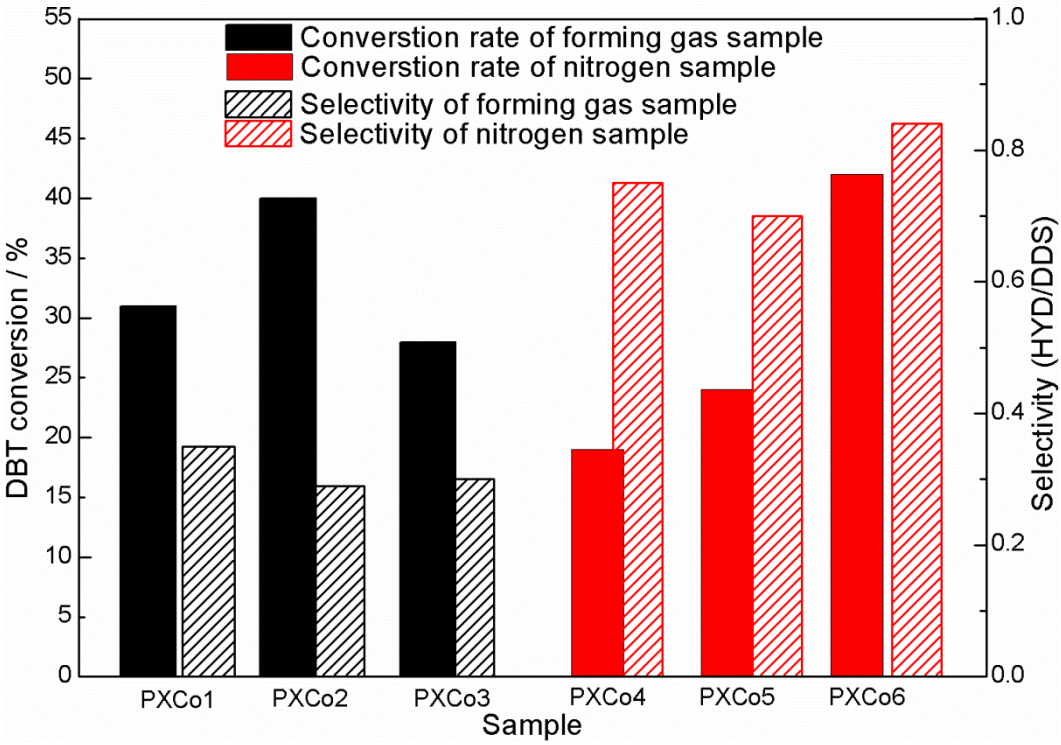

Figure 3.9 *Plot of DBT conversion rates and selectivity of different PXCo samples. (Reprinted from ref. 60 , Copyright (2015), with permission from Elsevier.)*

3.3.2 Structural and Crystallinity Analysis via TEM

Before and after the HDS reaction, TEM analyses were conducted to compare the microstructures of the two most active catalysts (PXCo2 (prepared in forming gas) and PXCo6 (prepared in N_2)).

In **Figure 3.10**, representative HRTEM micrographs illustrate the evolution of the microstructures of the catalysts under different synthesis conditions and HDS reaction. For the sample PXCo2, it is evident that the length and stacking number of the MoS_2 layers became larger after the HDS reaction (cf. **Figure 3.10**a) and (b)). On the other hand, the sample PXCo6 consists of more randomly arranged and bended single slabs of MoS_2 as compared to PXCo2 (cf. **Figure 3.10** (c)). Such microstructural feature is considered as the origin of catalytically active sites located mostly on the edges of the single slabs and thus leads to the highest HDS activity of all the as-prepared catalysts. After HDS the MoS_2 layers in PXCo6 changed into longer slabs with higher stacking (cf. **Figure 3.10**(d)). The HDS reaction seems to have more influence on the ordering of MoS_2 slabs in the sample prepared in N_2 than that in forming gas, since the increase after HDS in the stacking number for the sample PXCo6 is more pronounced than PXCo2.

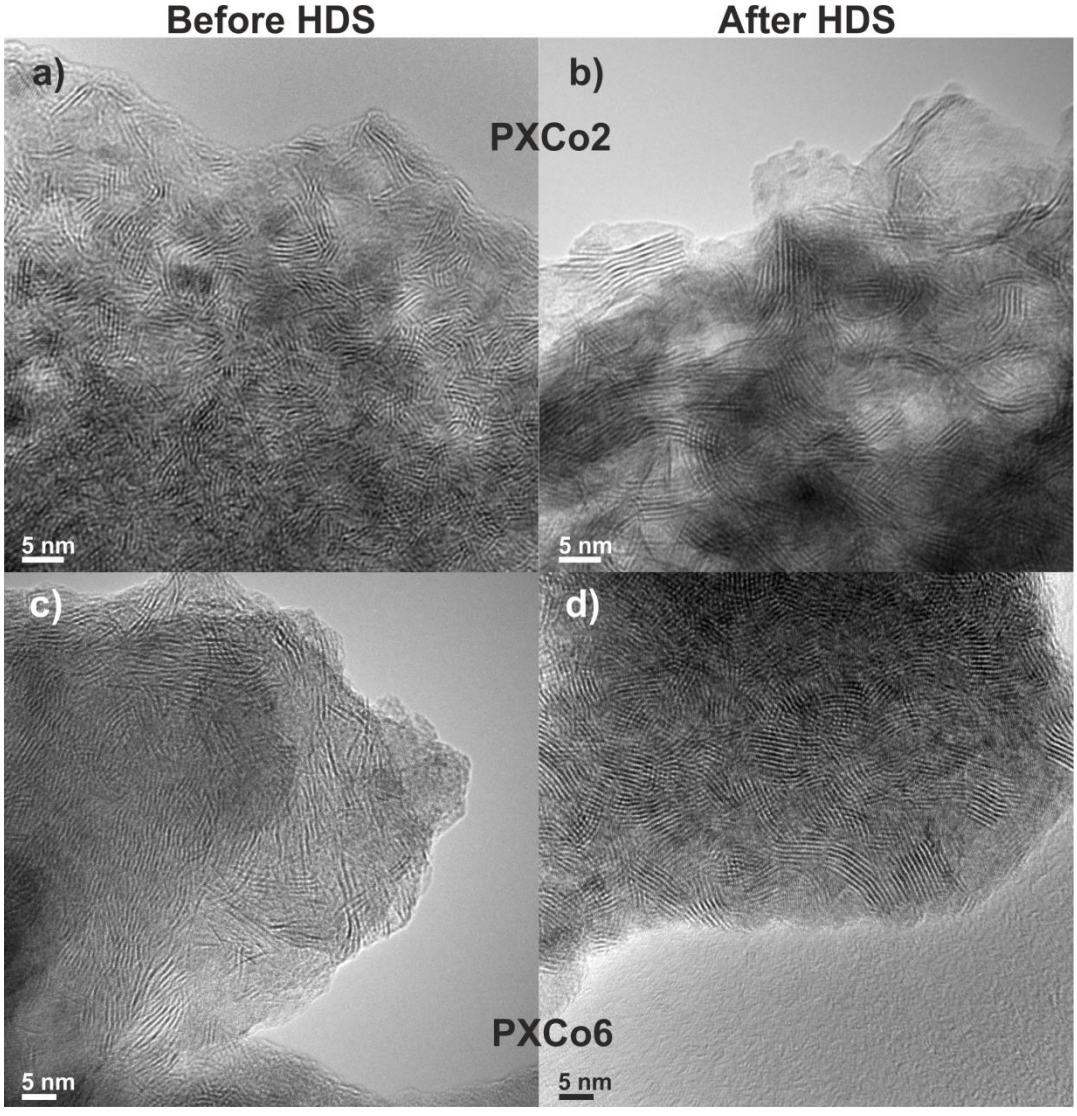

Figure 3.10 *HRTEM micrographs of PXCo2 and PXCo6 both before and after the HDS reaction. (a) and (b): Morphologies of Mo-S phase aggregates containing characteristic MoS_2 slabs in PXCo2 before and after HDS. The arrows signify the distinct stacking of the slabs. (c) and (d): Morphologies of the MoS_2 slabs of PXCo6 before and after HDS. The arrows in (c) are general guide lines to single and double slabs of MoS_2. (Reprinted from ref. 60, Copyright (2015), with permission from Elsevier.)*

Furthermore, electron diffraction and HRTEM simulation were carried out to investigate the distribution of the cobalt promoter among the MoS_2 phase. The most active catalyst PXCo6 is of high interest. Before HDS, the presence of cobalt sulfide (space group: $P6_3/mmc$) polycrystals in PXCo6 is confirmed, as it can be inferred from the SAED pattern shown in **Figure 3.11**(b): The d-values of the Bragg reflections on concentric diffraction rings can be assigned to those of CoS. The presence of the CoS phase is in good agreement with XRD results.[60] As no lattice fringes assigned to cobalt sulfide crystals can be identified in the HRTEM study (**Figure 3.11**(a)), it suggests they are well dispersed in the MoS_2 matrix. It should be noted that in the SAED pattern the reflections from the MoS_2 phase are exceptionally weak due to the presence of single slabs in the sample PXCo6, which is a further support to the HRTEM studies (cf. **Figure 3.10**(c) and **Figure 3.11**(a)).

After the HDS reaction, the HRTEM micrograph reveals a more condensed stacking of the MoS_2 slabs as well as more pronounced aggregations of the cobalt sulfide promoter crystals (**Figure 3.11**(c)). **Figure 3.11**(d) presents a Wiener filtered HRTEM micrograph of the lattice fringes of highly crystalline Co_9S_8 phase (space group: Fm-3m), indexed to be along the [101] zone axis.

Moreover, to further confirm the cobalt sulfide species identified by the HRTEM imaging, a computer simulation with a multislice approach was performed with the aid of JEMS software.[59] The best matched simulated micrograph was achieved with a sample thickness of 32.29 nm, which is approximately the thickness of 32.6 unit cells of Co_9S_8, and a defocus value of 242.7 nm (underfocussed). However, it can be inferred from **Figure 3.11**(c) that the lower part of the agglomeration of the MoS_2 slabs is actually in focus; therefore the large defocus value for the simulation of Co_9S_8 can be considered reasonable. The bright Fresnel fringes on the edges of the Co_9S_8 particles arise from the different height level of these crystallites as compared to the in-focused MoS_2, i.e. the different distance to the objective lens of the microscope.

The simulated micrograph is incorporated together with experimental micrograph as shown in **Figure 3.11**(d), presenting a fairly good compatibility with the experimental data. However, the contrast modulation of brighter and darker fringes in the experimental HRTEM micrograph is not reproduced by the simulation. It could probably originate from two reasons: (1) An overlapping of the Co_9S_8 nanocrystal with an amorphous cobalt sulfide region or with another orientation of Co sulfide crystallite underneath leads to a Moiré like pattern.[106] As it is demonstrated in **Figure 3.11**(c), there is a large aggregation of the Co-sulfide particles joining together; therefore, the overlapping is highly possible to occur. (2) Such nanosized crystallite can be under external strains which can possibly cause a distortion in the crystalline lattice,[107]

e.g. twining or stacking fault, and further induces the contrast modulation in the HRTEM micrograph.[108]

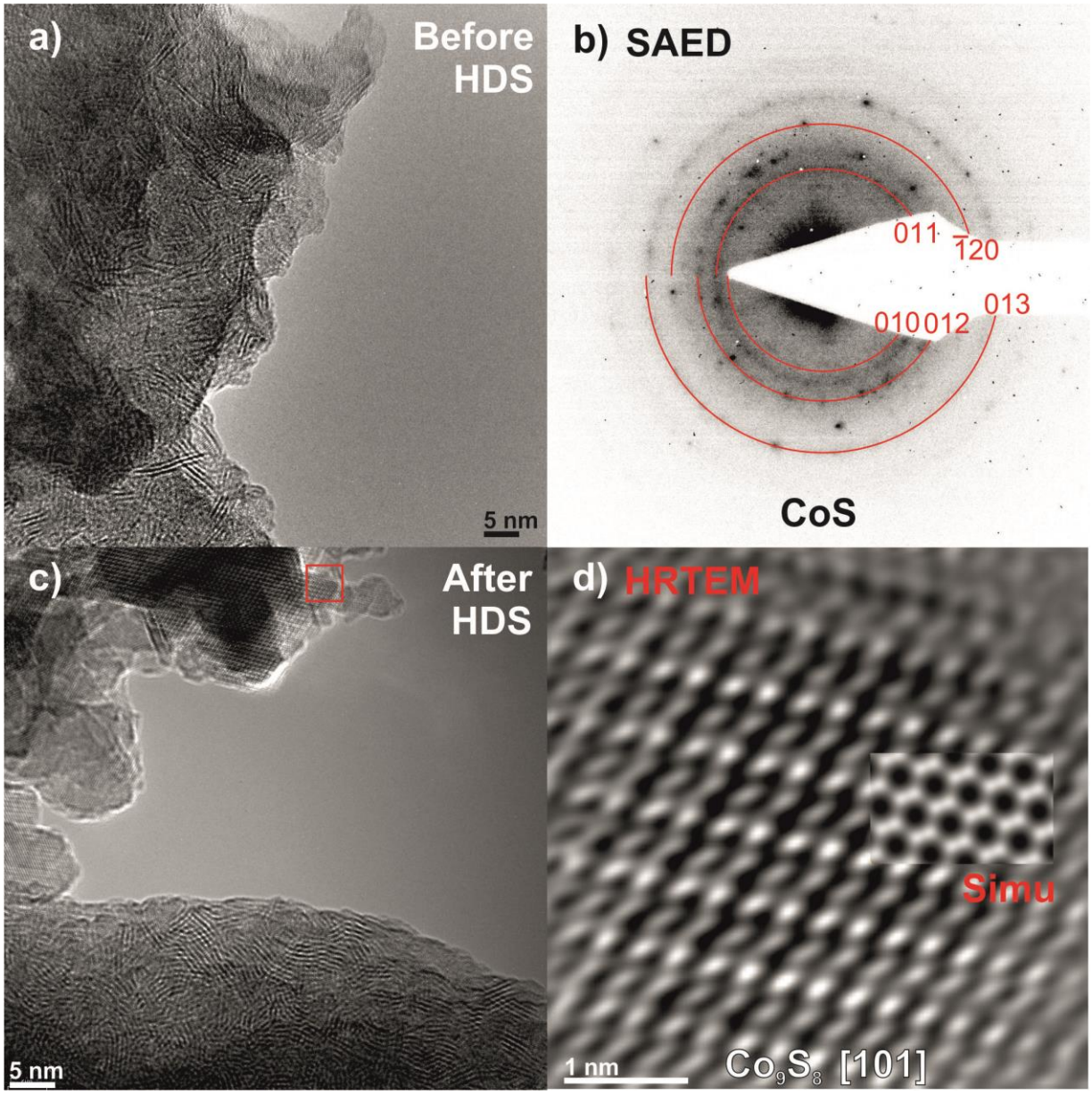

Figure 3.11 *Comparison of the slab arrangement of MoS_2 and different phases of the cobalt sulfide crystals in PXCo6 before and after HDS. (a) Typical MoS_2 microstructures of PXCo6 before HDS. (b) SAED pattern from a large region by applying a 250 nm diameter aperture, the center part of the selected region is shown in (a). (c) Highly ordered and condensed MoS_2 slabs of PXCo6 after HDS in the lower part, and highly crystalline Co_9S_8 agglomerations in the upper part of the micrograph. (d) The enlarged and filtered HRTEM micrograph along the zone axis of [101] of Co_9S_8 from the nanocrystal marked with a square in (c), (d) inset: a simulated micrograph. (Reprinted from ref. 60, Copyright (2015), with permission from Elsevier.)*

3.3.3 Quantitative Analysis of Rotational Average Profiles from SAED Patterns of MoS_2 Phase

Due to the intrinsic 'localized' nature of TEM, a statistic analysis of the crystallinity of the MoS_2 catalysts was performed. An evaluation of rotational average profiles of the SAED patterns can enable an interpretation of the SAED patterns on a quantitative base and examine structural ordering within circular transmitted areas of 250 nm in diameter. In the following the crystallinity of MoS_2 in the most catalytically active sample PXCo2, PXCo6 is compared to two other catalysts (PXCo3 and PXCo4) which were the least active in the HDS reaction.

The SAED patterns were acquired from selected regions containing only the MoS_2 phase. Generally, the rotational average profiles correspond to the 1D intensity profile of a 2D diffraction pattern. As shown in **Figure 3.12**, the rotational average profiles are background subtracted using a Matlab program and normalized. Each peak on the profile is correlated to a specific diffraction ring (or non-resolved multiple reflection rings) inside the SAED pattern.

Before HDS, the 002 reflection showed the highest intensity in the rotational average profiles in all cases. After HDS, the intensity of 100 and 103 reflections were much more pronounced or even exceeded that of the 002 reflection (c.f. intensity ratios presented in **Table 3.1**). These observations indicate a development of more ordering within the (100) and (103) planes, e.g. less turbostratic defects. This finding is surprising when taking into account the more pronounced stacking of the (002) planes after HDS as observed by HRTEM (cf. **Figure 3.12**(b) and (d)). However, it can be rationalized by considering a structural model evolution from nanosized single or a few stackings of the high aspect ratio MoS_2 nanobelts into a more pronounced 2D layered structure of the MoS_2 flat flakes. In other words, after the HDS reaction, even if the stacking of the MoS_2 (002) basal planes increases, the lateral dimension of the basal planes further develops, leading to a more prominent layered morphology of MoS_2 particles. Thus there is more ordering in the (100) and (103) planes inside the layers. As a result, the layered texture becomes dominant, i.e. the MoS_2 flakes flip over. Consequently, (002) planes are preferably lying perpendicular to the electron beam, thus, less contributing to the diffracted intensity of the (002) reflection.

Furthermore, the d-value of the (002) plane is in general decreasing after HDS (measured from the rotational average profile, not shown), becoming more comparable to the theoretical value for the bulk material. It can be inferred from this evolution that after HDS the arrangement of MoS_2 basal planes approximates that of randomly distributed bulk particle material under dynamic approximation (see **Figure 3.15**(d)). The observations of a higher crystallinity of MoS_2 in the samples PXCo2, PXCo3 and PXCo4 after HDS are in good agreement with the XRD result obtained by *Felix Niefind*. The rotational average profiles did not vary significantly for PXCo4 and PXCo6 both before and after HDS, which are further verified in the XRD analysis.

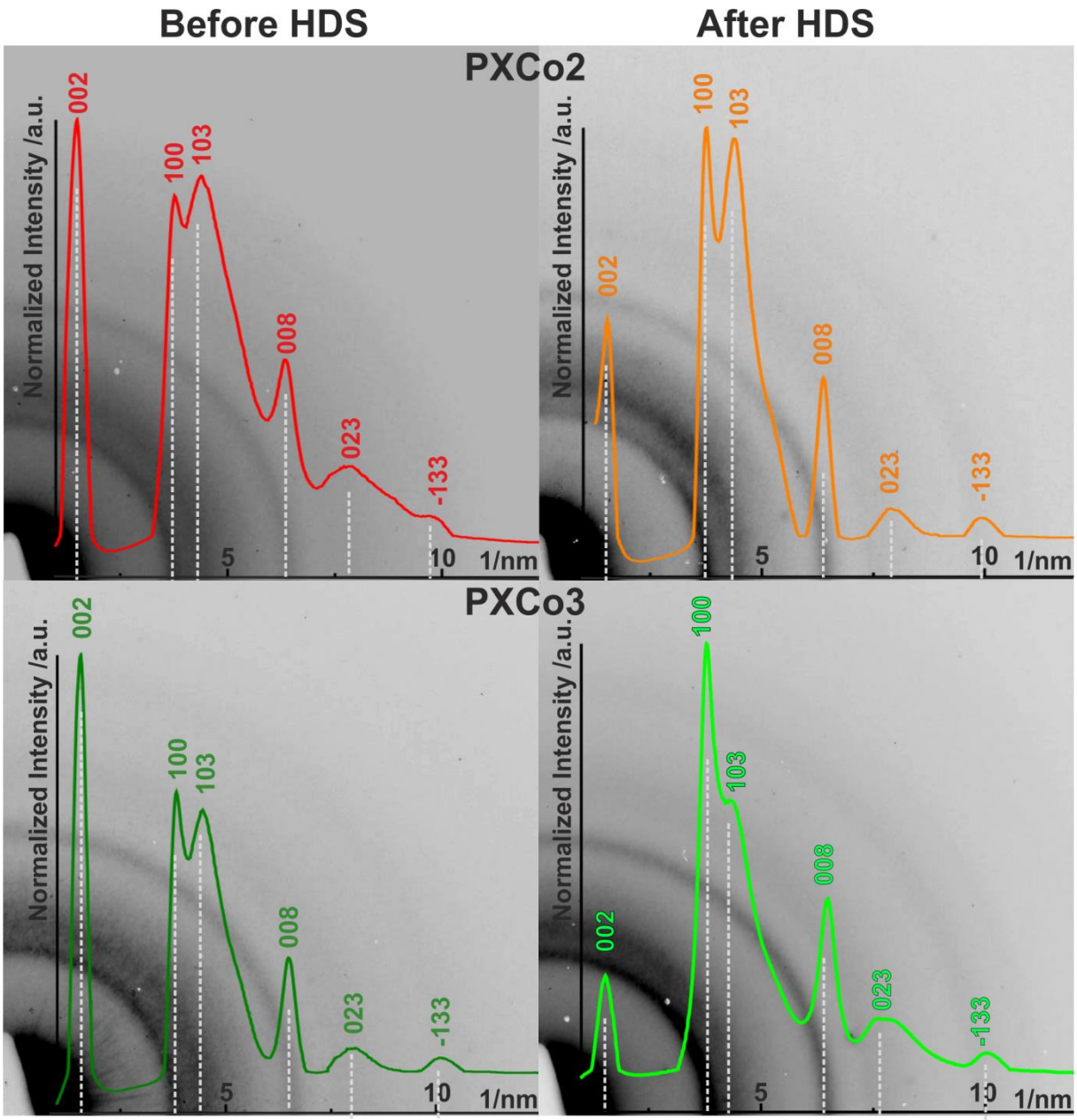

Figure 3.12 *Contrast inverted SAED patterns (a quarter of the pattern is shown) and the resultant rotational average profiles obtained from the typical MoS_2 aggregates for samples PXCo2, PXCo3, PXCo4, PXCo6 both before and after the HDS reaction. The small noise-like spikes in the rotational average profiles of PXCo4 and PXCo6 are created by stray X-ray intensity (point blemish). (Reprinted from ref. 60, Copyright (2015), with permission from Elsevier.)*

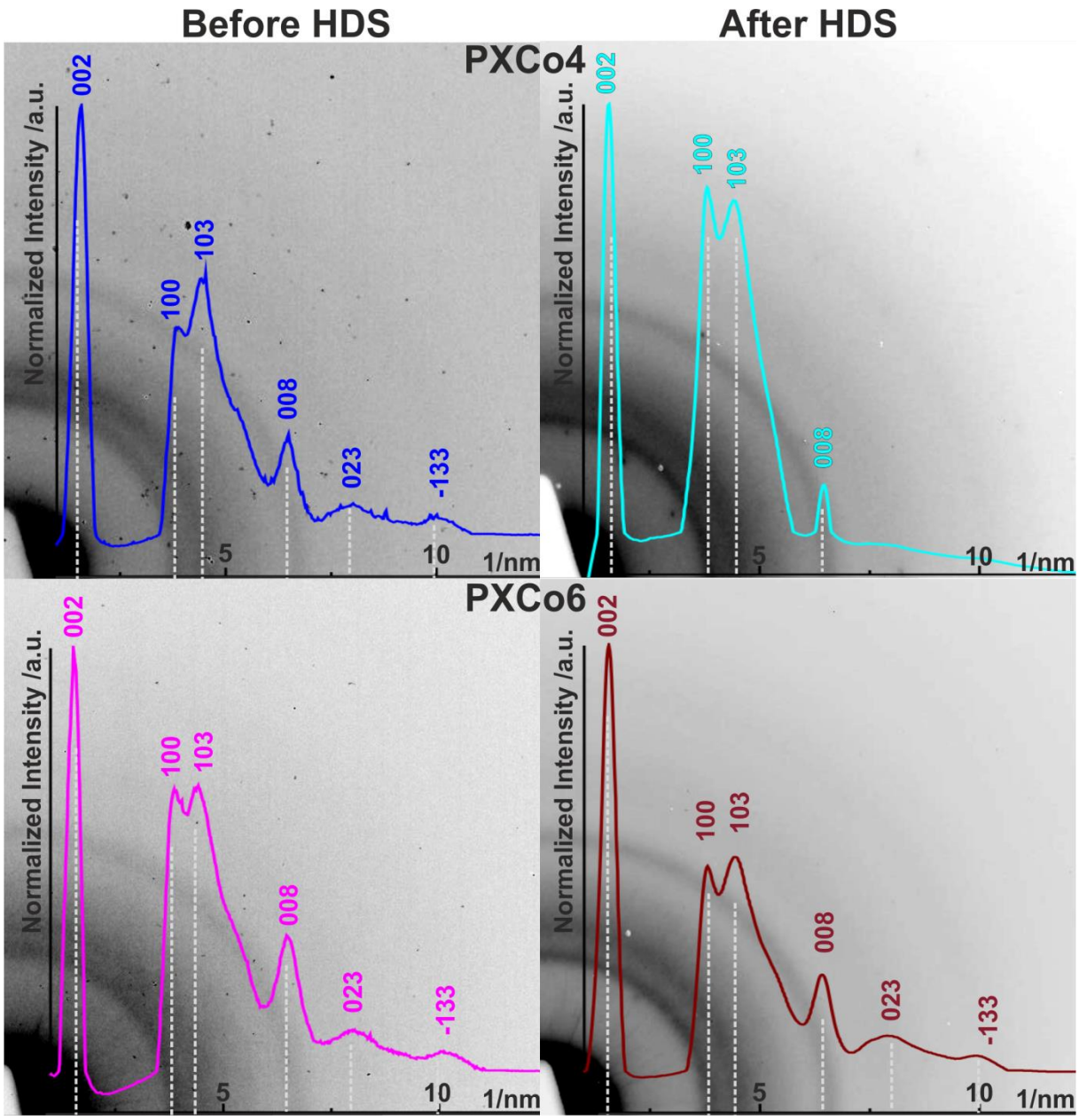

Figure 3.12 (Continued). *Contrast inverted SAED patterns (a quarter of the pattern is shown) and the resultant rotational average profiles obtained from the typical MoS_2 aggregates for samples PXCo2, PXCo3, PXCo4, PXCo6 both before and after the HDS reaction. The small noise-like spikes in the rotational average profiles of PXCo4 and PXCo6 are created by stray X-ray intensity (point blemish). (Reprinted from ref. 60, Copyright (2015), with permission from Elsevier.)*

Table 3.1 *Comparison of the ratio of normalized intensities of the (100) and (103) reflections to that of the (002) reflection (the intensity of the (002) peak is used for normalization and set to unity) before and after the HDS reaction. (Reprinted from ref. 60, Copyright (2015), with permission from Elsevier.)*

Sample	MoS_2 hkl	I_{hkl} / I_{002} before HDS	I_{hkl} / I_{002} after HDS
PXCo2	100	0.82	1.89
	103	0.87	1.84
PXCo3	100	0.67	4.54
	103	0.63	2.87
PXCo4	100	0.48	0.81
	103	0.60	0.78
PXCo6	100	0.66	0.48
	103	0.67	0.50

The observation from the rotational average profiles is further supported by the histograms based on the HRTEM investigation (see **Figure 3.13** and **Figure 3.14**) (calculated by *Felix Niefind*). For the samples PXCo2 and PXCo3, their stacking height did not vary a lot before and after HDS. On the other hand, the increased slab length after HDS, i.e. the lateral dimension of the MoS_2 basal planes, could result in a higher ordering of the (100) and (103) planes. As a result, the intensity of the (002) reflection from the rotational average profile is lower while those of (100), (103) are more prominent after HDS. The stacking degree of the sample PXCo6 increased after HDS, while its slab length did not change significantly. Therefore, the (002) reflection of PXCo6 can be still dominate in the rotational average profile after HDS. Hence PXCo6 exhibits similar intensity distributions of the rotational average profiles before and after HDS. For the sample PXCo4, the longer slab length evolved after HDS is the reason for an increase in the intensities of the (100) and (103) reflections. However, since the stacking height of PXCo4 slightly reduced after HDS, according to the histogram, the strong intensity of the (002) reflection can be probably attributed to a dynamical excitement because of its proximity to the primary electron beam.

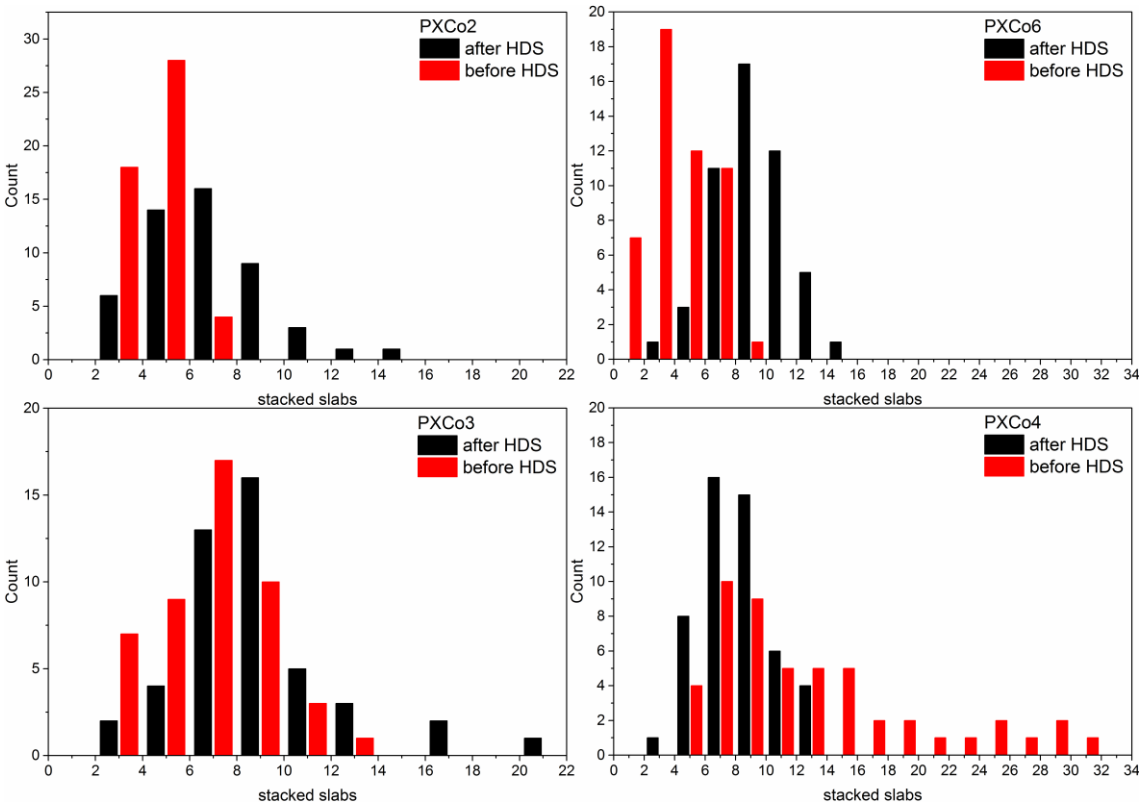

Figure 3.13 *Histograms of the stacking height of MoS_2 slabs of catalysts PXCo2, 3, 4 and 6 before and after HDS. Calculation performed by Felix Niefind. (Reprinted from ref. 60, Copyright (2015), with permission from Elsevier.)*

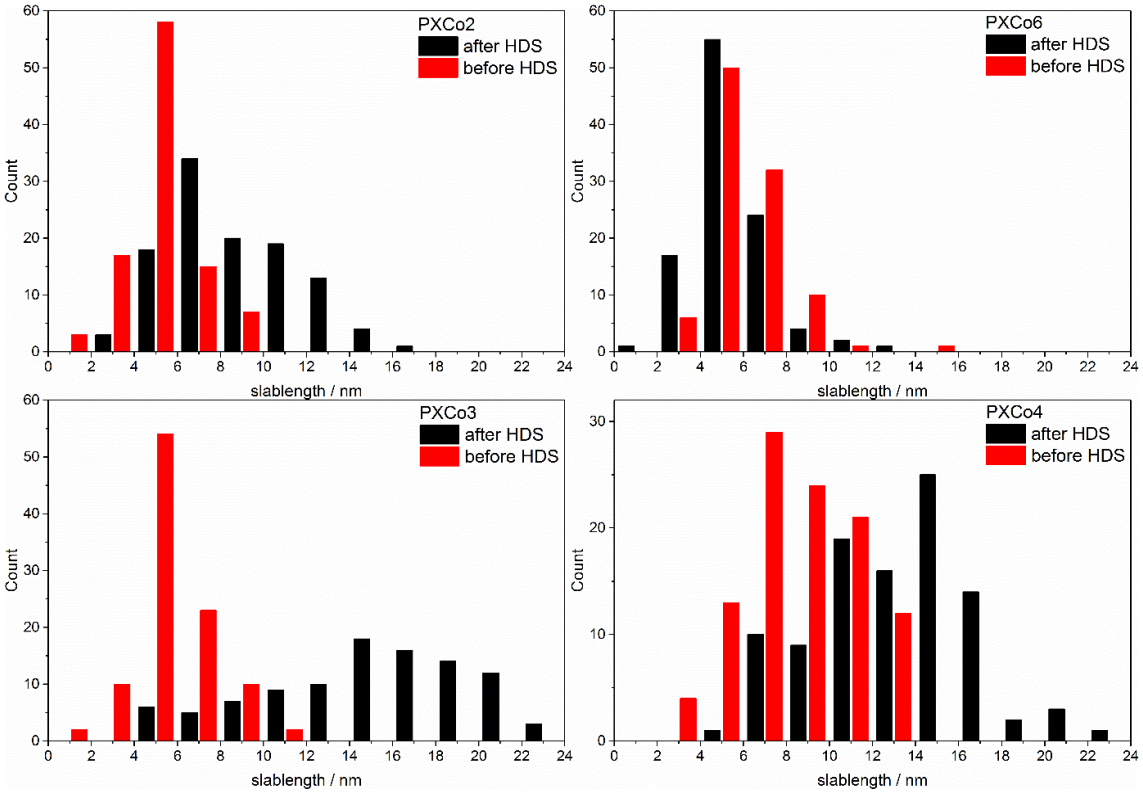

Figure 3.14 *Statistical analyses of the slab lengths of catalysts PXCo2, 3, 4 and 6 before and after HDS. Calculation performed by Felix Niefind. (Reprinted from ref. 60, Copyright (2015), with permission from Elsevier.).*

3.3.4 Kinematical and Dynamical Simulation of Rotational Average Profiles of MoS_2 Phase before and after HDS

By conducting a simulation of the SAED ring patterns and their corresponding rotational average utilizing the JEMS program, there is a coincidence between the simulated profile and the experimental one before HDS reaction (cf. **Figure 3.15**(a), and (b)). The experimental SAED pattern of the MoS_2 clusters in sample PXCo2 before HDS (depicted in an inverted gray scale in **Figure 3.15**(a)) shows a fair match with the simulated pattern (**Figure 3.15**(b)). The intensity difference between the 100 and 103 reflections might be attributed to the residual background in the experimental pattern. Furthermore, the unresolved 105 reflection as marked out in the experimental pattern can be hidden from the diffuse background in the circular region between the 103 and 008 reflections. The background can stem from two factors:

(1) The influence from the strong primary beam, therefore the 100 reflection is more excited than 103 due to its proximity to the transmitted beam;

(2) The contributions of some amorphous phases inside the examined area of the SAED study, e.g. amorphous Mo-S derived from the PX precursor, or amorphous Co sulfide promoter, might result in the broadened and diffuse background.

A more clear and quantitative investigation is achieved by comparing the rotational average profile from the experimental data (red curve in **Figure 3.15**(c) and (d)) and the simulated data (black curve in **Figure 3.15**(c)). The unresolved peaks such as 105 and 118 are shown as shoulders beside the main peaks. It is probably because the background subtracting Matlab program does not take into account the second factor which causes a diffuse background in the SAED pattern, i.e. the contributions from the amorphous components.[38]

Despite of the residual background, the rotational average profile of the experimental diffraction pattern before HDS reaction is quite close to the intensity profile from a kinematic calculation based on randomly dispersed MoS_2 crystallites for X-ray diffraction (blue profile in **Figure 3.15**(c)). It should be noted that the integrated intensity of the electron diffraction and that of the X-ray diffraction cannot be compared directly. Nonetheless, the integrated intensity distribution of the simulated ring pattern can be considered as an approximation close to the kinematical diffraction condition in XRD, since the simulation is carried out by following the Debye assumption[109], i.e. by constructing a structure model of a finite spherical MoS_2 crystal with a dimension of 10×10×10 unit cells in x, y and z direction respectively. Within these dimensions the electron beam can be considered to be interacted with the sample material similar as X-ray, i.e. neglecting the multiple scattering and thus fulfilling kinematic diffraction condition. Therefore the simulated electron diffraction and its corresponding rotational average profile are comparable to that derived from the kinematic calculation.

After HDS the intensity distribution of the rotational average profile for PXCo2 are more similar to the intensity profile of dynamic approximation (see **Figure 3.15**(d)). The dynamic approximated profile is calculated based on an infinite crystal of MoS_2 and includes the Blackmann correction[110] for dynamic scattering condition.

Moreover, the decrease of the 002 peak after HDS can be explained in terms of the difference between the dynamical and kinematical theory. The ratio of the dynamical to the kinematical integrated intensities of a powder sample has been obtained by Blackmann as described in the following equation[111]:

$$\frac{I_{dyn}}{I_{kin}} = \exp(-2BH^2) A_H^{-1} \int_0^{AH} J_0(2x)dx$$

$$A_H = 2.09 \times 10^{-2} D\lambda |V_{0H}| \exp\left(-BH^2\right),$$

where subscripts T and 0 refer to the temperature T and to absolute zero, respectively. D is the size of the mosaic blocks or the dynamical crystal size in the direction of the beam, V_{0H} is the Fourier coefficient of the crystal potential and J_0 is the zero-order Bessel function. The most important factor in this function is $\exp(-2BH^2)$, i.e. the Debye-Waller factor, and B represents the relative vibrational motion of different parts of the sample structure. An ordered bulk crystal has smaller B value while amorphous or nanosized structures exhibit larger B value.[111] Thus this equation explains why the reflections (especially the 002 reflection in MoS_2) originated from a finite nanocrystal model (before HDS) has higher intensities as compared to that based on an infinite crystal (after HDS).

With the aid of diffraction pattern simulation, the comparison of the rotational average profiles of the PXCo2 sample before and after HDS implies that the MoS_2 slabs developed into aggregates more close to randomly distributed bulk material after HDS, while the samples before HDS represent mostly nanosized structure.

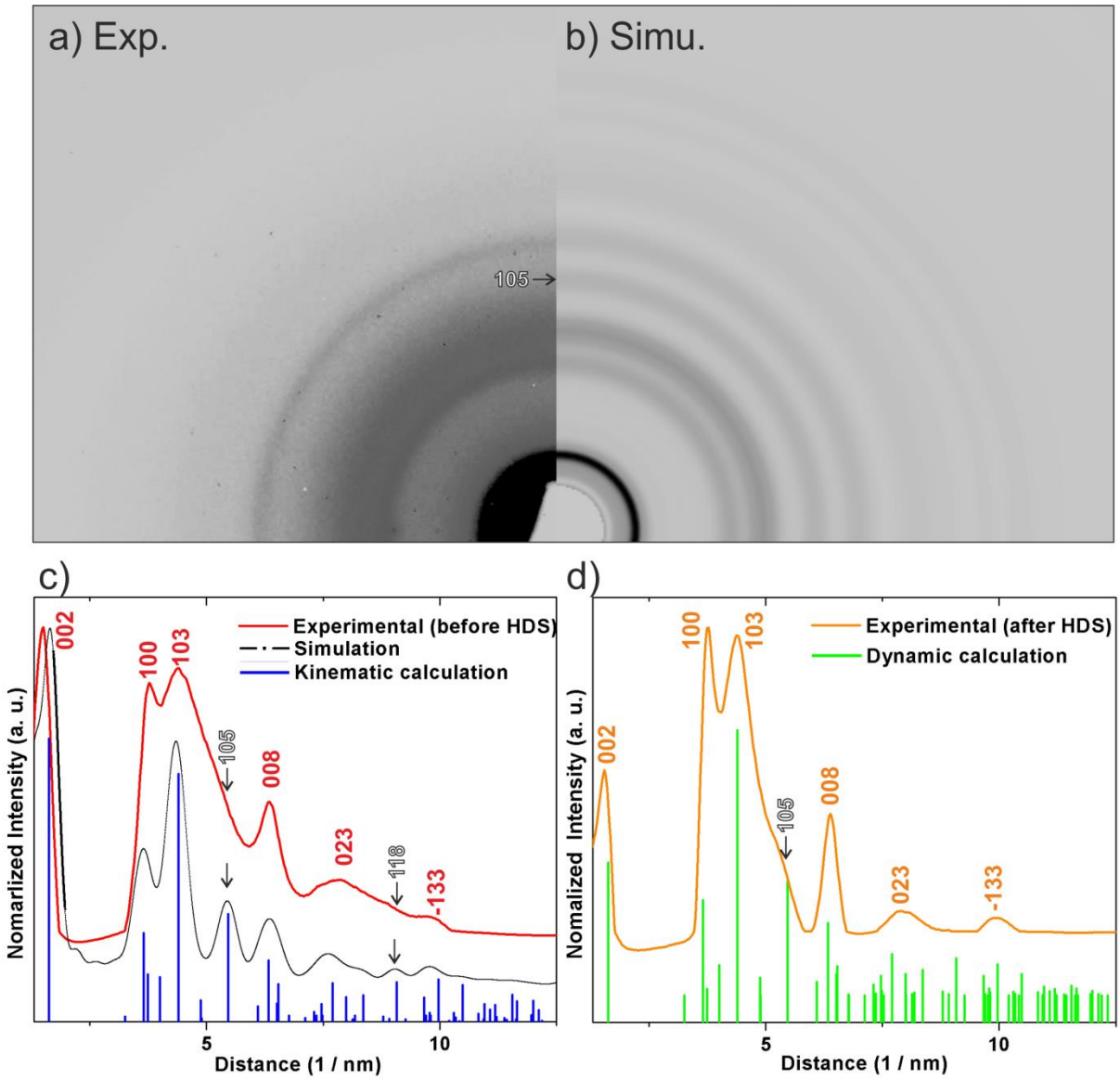

Figure 3.15 *(a) Experimental SAED pattern (contrast inverted) of an aggregate of MoS_2 phase in sample PXCo2 before HDS. (b) Simulated SAED pattern before HDS in comparison with (a). (c) Before HDS: Experimental rotational average profile (red curve) extracted from the SAED pattern in (a) in comparison with the simulated rotational average profile (black dotted curve) as well as the intensity profile (blue columns) calculated based on kinematic scattering theory. (d) After HDS: experimental rotational average profile (orange curve) compared with the intensity profile (green columns) calculated based on dynamic scattering theory.*

3.3.5 HRTEM Study of MoS_2 / Co_9S_8 Interface

An extreme case of a PXCo sample (before HDS) with the smallest selectivity ratio (S_{HYD} / S_{DDS} = 0.25) as well as the lowest conversion rate (26%) is studied via HRTEM investigation. The highly crystalline MoS_2 layers with large stacking degree observed under HRTEM (not shown) evident the low conversion rate, due to the lack of catalytically active sites on the edge location of the MoS_2 slabs. On the other hand, the possible reason for the low selectivity of this sample is explored. The interface is shown in **Figure** 3.16, and a structure model of MoS_2 is inserted. The bright contrast on the basal plane of MoS_2 arising

from the molybdenum atoms, while the chevrons are due to the inner molybdenum single layer and the outer S layer on both sides.[112] The promoter effect is believed to be achieved by a bonding between the Mo atom and the Co atom, i.e. the Co-Mo-S phase model[78, 79]. Remos et al. showed a structure model for the interface between MoS_2 / Co_9S_8 where the Co-Mo bonding can be formed when the basal planes of MoS_2 is perpendicular to the Co sulfide.[6] However in the geometry depicted in **Figure** 3.16, the basal plane is attached parallel to the bulk Co_9S_8, and the sulfur terminated plane hinders the formation of Co-Mo bonds. Nevertheless, this sample shows more preference to the DDS pathway, implying that the promoter effect is quite pronounced. Further verification by building up the interface model and computer simulation is of high interests in order to develop a valid model to explain the promoter effect observed here.

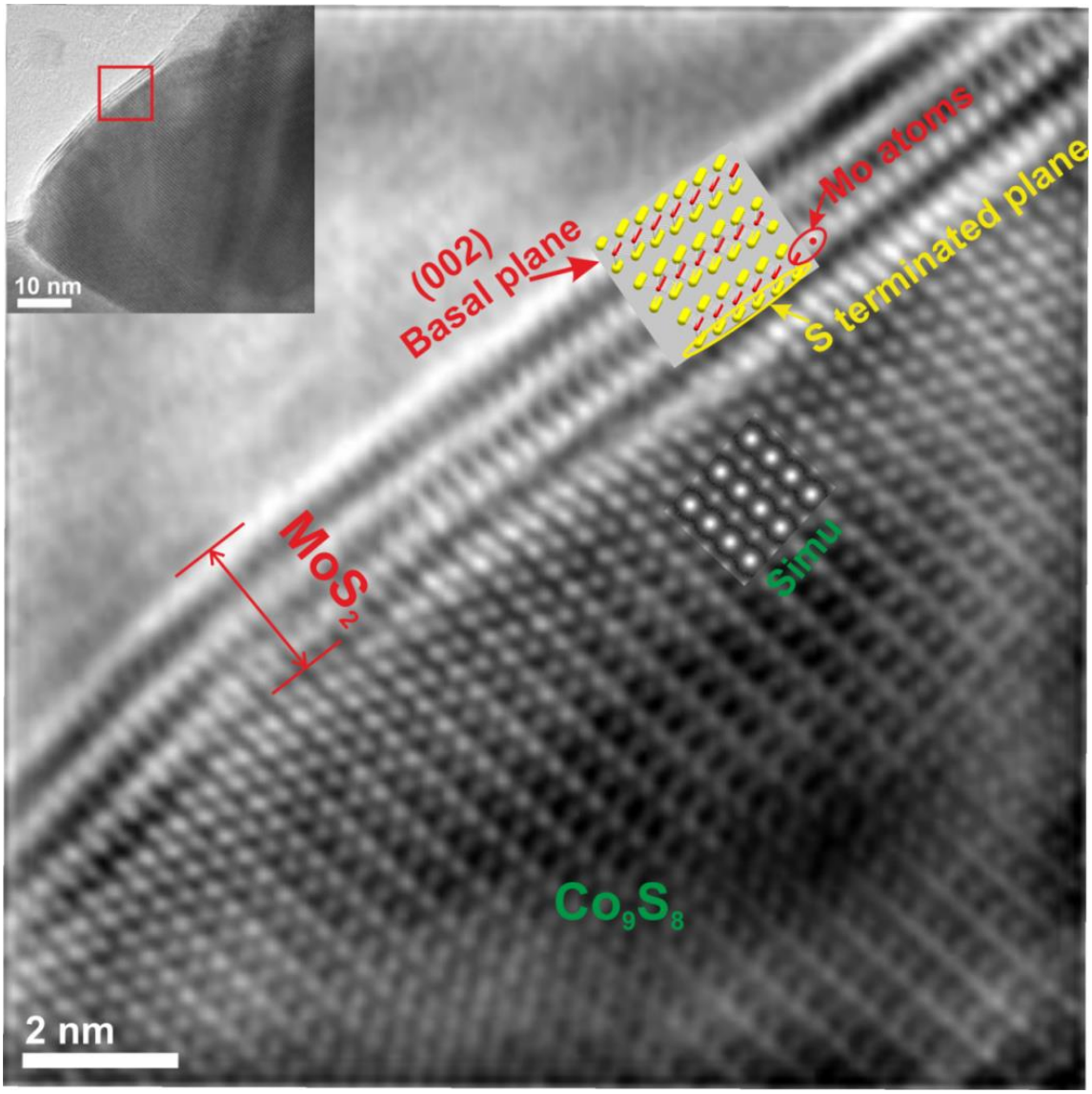

Figure 3.16 *Wiener filtered HRTEM micrograph of the MoS_2 / Co_9S_8 interface of a PXCo sample with the lowest selectivity ratio and conversion rate. The upper left inset depicts the region at a lower magnification, where the red box indicates the origin of the enlarged micrograph. The two lower right insets are computer simulation micrographs of the Co_9S_8 phase. The simulation is obtained with a defocus value of 40 nm and a sample thickness of 7.29 nm.*

3.3.6 Summary and Discussion

i. Effect of synthesis parameter:
In terms of morphology and structural properties of the catalysts, H_2/N_2 treatment generates more regular stacked slabs and less pronounced turbostratic disorder (sample PXCo1, 2, and 3) than observed for the samples prepared in N_2 (sample PXCo4, 5, and 6). The general structural features are observed in XRD, but are even better evidenced by the TEM micrographs.

ii. Influences of HDS reaction:
The HDS reaction leads to a larger stacking degree of the MoS_2 slabs in the catalysts obtained in H_2/N_2, while the samples prepared in N_2 are less affected as shown in **Figure 3.10**.
After HDS a redistribution of Co species and therefore a better promoting effect of MoS_2 in the sample decomposed in H_2/N_2 are observed. The XRD and TEM results confirm the existence of Co_3S_4 and Co_9S_8 in the H_2/N_2 samples before HDS, which are absent in the XRD data of the H_2/N_2 catalysts after the HDS; only by TEM investigation nanosized crystals of unidentifiable Co sulfide phases can be revealed. The better promoter effect explains the high selectivity of the H_2/N_2 catalysts to the DDS route.
For the catalysts obtained in N_2, XRD results indicate that the Co-poor CoS transformed into the more bulky aggregations of Co_9S_8 as evidenced in the HRTEM images as well (**Figure 3.11**). The redistribution of the Co species after HDS is less pronounced in the N_2 sample, thus less preference to the DDS pathway.

iii. Promoter effect:
Whether the Co is really doped on the edges of MoS_2 lattice could not be resolved within the aid of conventional TEM methods. Given to the observation that Co sulfides in the H_2/N_2 catalysts redistribute into nano particles during the HDS reaction, it is reasonable to rule out that the contact synergy (remote control) model[113] as a relevant explanation of Co promoting MoS_2.
Still the better Co promotion effect results in the very low HYD/DDS ratio near 0.3 (**Table 3.2**) for the H_2/N_2 sample. While the high HYD/DDS ratio of the N_2 synthesized catalysts may be due to a less good dispersion of Co or the presence of a CoS_x species that could not be detected in the X-ray powder patterns, which can only detected by EDX spectroscopy in TEM measurements: Regions of high Co contents were observed without any visible Co containing crystalline particles.

iv. Catalytic activity of the as prepared sample:
The sample PXCo6 obtained at the highest temperature in N_2 outperforms all other catalysts. The reason is evidenced by HRTEM images (**Figure 3.10**) that smaller MoS_2 slabs with lower stacking are present in this sample as compared to the catalysts prepared in H_2/N_2.
The decomposition temperature plays a crucial role in the H_2/N_2 samples. PXCo2 exhibits the highest catalytic activity while the other two decomposed at lower and

higher temperatures are less active. This may be rationalized by the assumption that at low temperature an optimal dispersion is not achieved, while higher temperature leads a segregation of Co sulfide species.

In addition, the carbon content which can be referred from elemental analysis before the HDS reaction is on average higher for the samples synthesized in H_2/N_2. These C containing residues may block catalytically active sites.

To verify the catalytic activity of the as prepared samples, a short comparison with literature data is summarized in **Table 3.2**. The selectivity, however, varied in a range from 0.35 for the CoMo-H (lowest carbon content), and 0.57 for CoMo-C_4 (medium carbon content), and to a very large 1.5 for the unpromoted MoS_2.[114] This drastic variation of the selectivity can be ascribed to the promoter effect of Co. Regarding the conversion rates and activities the as prepared catalysts in this study can be classified as highly catalytic active.

v. Quantitative study via TEM:

By quantification of the rotational average from the SAED patterns a general observation can be made. The comparison of the rotational average profile with the simulated one as well as the kinematical and dynamical calculated intensity profiles enables to interpret valuable information about the crystallinity and microstructural arrangement of the MoS_2 phase inside the sample before and after. It is validated by the observation via HRTEM and by the XRD result.

Further computer simulation of the HRTEM micrograph of the interface between MoS_2 and Co sulfide can provide atomic insight into the promoter effect.

Table 3.2 *Results of the catalytic measurements; selectivity, rate constant and conversion rate. (Reprinted from ref. 60, Copyright (2015), with permission from Elsevier.)*

Sample	HYD/DDS	k (mol s^{-1} g^{-1})	Conversion / %	Surface area / m^2 g^{-1}
PXCo2	0.29	1.59×10^{-6}	40	11.7
PXCo6	0.84	1.79×10^{-6}	42	10.6
		Comparison with literature		
MoS_2[114]	1.5	0.17×10^{-6}	10	5.5
Co-MoS_2[114]	0.6	0.76×10^{-6}	40	31.4
Co/C_1-MoS_2[114]	0.1	0.20×10^{-6}	10	3.1
CoMo-H[115]	0.35	0.94×10^{-6}		53
CoMo-C_4[115]	0.57	1.73×10^{-6}		253

3.4 EELS Study of MoS_2/Carbon Composite (MoS_xC_y)

As electrode material in lithium ion batteries, MoS_2 is considered to be a promising candidate.[116] Several composites of MoS_2-like nanoslabs and carbon of unknown species (noted as C) with enhanced catalytic activity and energy storage characteristics were obtained.[117,118] The properties of MoS_xC_y strongly depend on the bonding states of carbon in the composite, e.g. Graphitic carbon, i.e. sp^2-hybridized carbon, would possibly enhance the conductivity favoring for battery materials whereas carbide-like carbon can accommodate active sites for catalytic reactions. In this section, the nature of the carbon species incorporated into the MoS_2 composites is investigated by EELS, and is compared with reference samples of carbides and graphite.

3.4.1 EELS Study of MoS_2/Carbon Composite Samples

HRTEM and EELS investigations were carried out on the Bu_4ATM samples synthesized at different temperatures (cf. Figure 3.17). The synthesis temperature has a pronounced influence on the microstructures of the as formed MoS_2 slabs. For the sample decomposed at 350 °C, the HRTEM micrograph (cf. Figure 3.17(a)) reveals an agglomeration of mostly disordered single slabs of MoS_2, while the sample obtained at higher temperature (750 °C) exhibits more ordered slabs with higher stacking degree and longer length (cf. Figure 3.17(c)). Moreover, the EEL spectra from the 350 °C sample are different from the 750 °C sample: The carbon K edges are more smooth and featureless (cf. Figure 3.17(b)). Furthermore, the spectra exhibit a π* peak (287.1~289.3 eV), and a broadened σ* peak with only one discernible maximum (297.1~301.1 eV) (cf. **Figure 3.20** for the average peak position).

On the other hand, more features are present in the σ* peak fine structure of the 750 °C sample (cf. arrows in Figure 3.17(d)), which indicates a more crystalline structure. This observation is further proved by HRTEM study (Figure 3.17(c)). The positions (cf. Figure 3.17(d), positions 2 and 4) showing more smooth EEL spectra can originate from: (1) less crystalline regions due to the inhomogeneous sample; (2) enhanced thicknesses leading to an incomplete deconvolution to remove the plural scattering effects; (3) locations amorphisized by high energy electron beam. Nevertheless, the locations of the π* peak (286.1~287.1 eV) are all shifted to lower energy with respect to the 350 °C sample, indicating in the 750 °C sample a carbon bonding similar to the conducting phase of carbon, i.e. graphite.[119]

The differences of the EEL spectra present in the same sample have been discussed in **Section 3.1.3**. Despite of the discrepancies, the determining factor of the EEL spectra should be the positions of the characteristic peaks, especially for the π* peak on the onset of C-K edge. From Figure 3.17(b) and (d), there is a consistency of the π* peak position in the same sample.

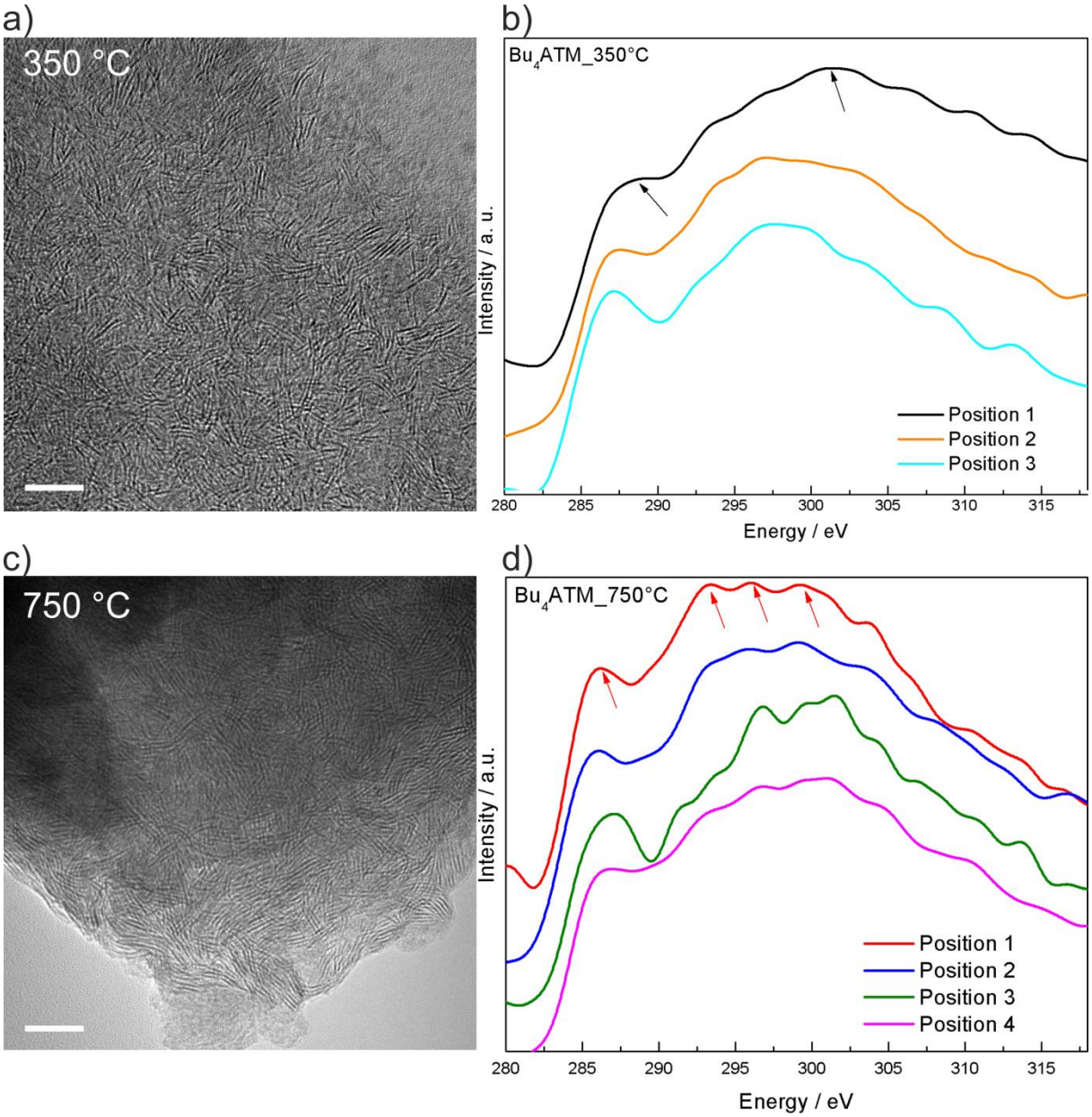

Figure 3.17 *Comparison of morphology and EEL spectra for sample Bu_4ATM_350 °C and Bu4ATM_750 °C. a) HRTEM micrograph of sample Bu_4ATM_350 °C showing disordered and mostly single slabs of MoS_2. b) EEL spectra of the carbon K edge of sample Bu_4ATM_350 °C from different positions of the sample. The arrows mark out the peak maxima in the region of π* and σ* peak. c) HRTEM micrograph of sample Bu_4ATM_750 °C. A more crystalline MoS_2 is obtained at higher synthesize temperature. d) Carbon K edge EEL spectra of sample Bu_4ATM_750 °C from different positions of the sample. Some fine structure features are marked out with arrows as visual guidelines. Scale bar is 10 nm.*

The other MoS_2 composite Me_4ATM_750 °C derived from a shorter carbon chain precursor shows a fullerene-like microstructure (see HRTEM micrograph in **Figure 3.18**(a)). The higher stacking degree and crystallinity than Bu_4ATM_350 °C sample can be due to the higher decomposition temperature and less incorporated carbon. Accordingly, the EEL spectra exhibit more features than the Bu_4ATM_350 °C and Bu_4ATM_750 °C samples (**Figure 3.18**(b)). There is a bump, i.e. an unresolved peak, around 290 eV in the spectra. Due

to the similarity between the microstructures of this sample and carbon fullerite (C_{60}), this additional feature can be analogue with the EEL spectrum of carbon fullerite.[19] The average position of the π* peak is around 287.0 eV (cf. **Figure 3.20**), which is shifted to lower energy as compared to sample Bu_4ATM_350 °C, suggesting a carbon bonding state resembling graphite.

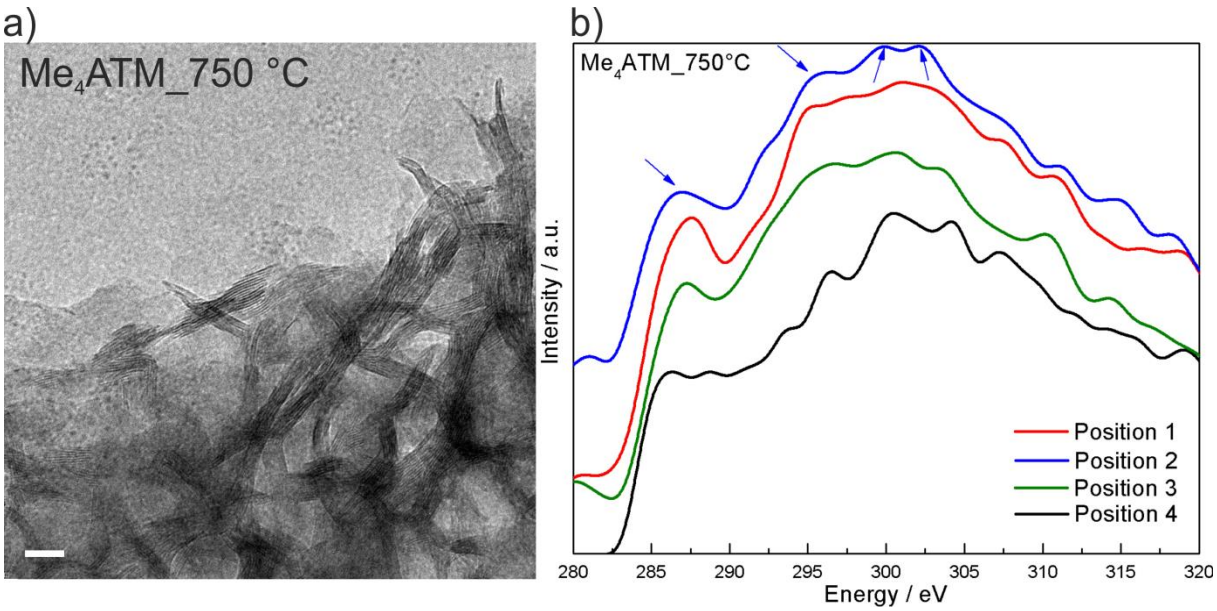

Figure 3.18 *(a) HRTEM micrograph of sample Me_4ATM_750 °C. The characteristic MoS_2 slabs are more ordered and with higher stacking degree. All regions observed in the composite sample exhibit semi-hollow onion-like fullerene morphology of the slab structures. Scale bar is 10 nm. (b) EEL spectra of the carbon K edge of sample Me_4ATM_750 °C from four different positions. Arrows point out the pronounced peaks on the edge.*

3.4.2 EEL Spectra of Reference Samples: Graphite and Carbides

Studies on three types of reference samples: graphite, MoC and Mo_2C are carried out to provide more insight into the possible carbon bonding states existing in different carbon compounds. Three representative EEL spectra are shown in **Figure 3.19**. The spectra of MoC and Mo_2C display two main peaks at the same energy loss: π* peak (P1): 288.6 eV, and σ* peak (P2): 299.2~300.3 eV. The slight curvature present in the near edge region (305~320 eV) in the Peak 2 of Mo_2C might be due to a different coordination number of the carbon atoms surrounded by molybdenum atoms as compared to MoC. For graphite, the π* peak (P1) is at 286.1 eV and σ* peak (P2) at 295.6 eV. The peak positions of the graphite and carbides are quite distinct, which can serve as criteria to differentiate between graphitic and carbide-like carbon by examining the experimental EEL spectra from unknown samples.

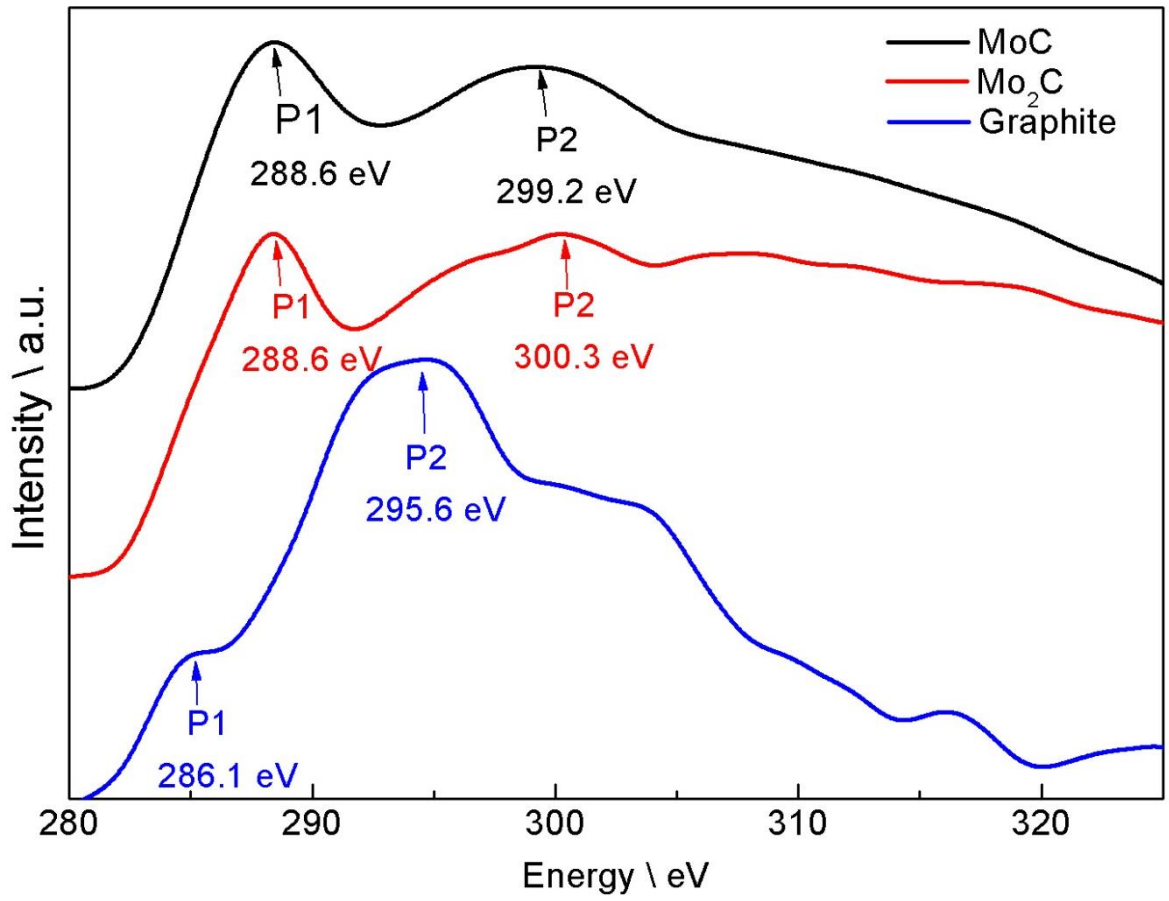

Figure 3.19 *A comparison of EEL spectra of reference samples. Black curve: MoC, red curve: Mo_2C, and blue curve: graphite. The two main peaks (π* (Peak 1) and σ* (Peak 2)) are marked out with arrows and their exact values of energy loss are shown. The spectrum from graphite is completely different from the carbide samples.*

3.4.3 Comparison of MoS_2 / Carbon Composites with References

The average positions of the characteristic peaks in the carbon K-edge are calculated and are shown in **Table 3.3** and **Table 3.4** together with selected literature values. A plot based on the calculation is shown in **Figure 3.20**. The two characteristic peaks of all the as prepared samples are within the range of graphite and molybdenum carbide, suggesting a mixture of both graphitic and carbide-like carbon species. Moreover, the samples Bu_4ATM_750 °C and Me_4ATM_750 °C synthesized at higher temperature have a π* peak located more close to the graphite reference sample. This finding is consistent with the observation that the π* peaks are shifted to lower energy loss, indicating a similar phase to graphite, i.e. the predominate carbon bonding state within the sample is sp^2-bonded. Therefore, higher decomposition temperature can probably promote better crystallinity, as demonstrated in HRTEM micrographs, more ordered graphitic carbon phase inside the composite. On the other hand, the sample Bu_4ATM_350 °C shows a π* peak position closer to the carbide reference. The reasons can be the higher carbon content and lower decomposition temperature, which lead to a more carbide-like or disordered carbon bonding within the sample.

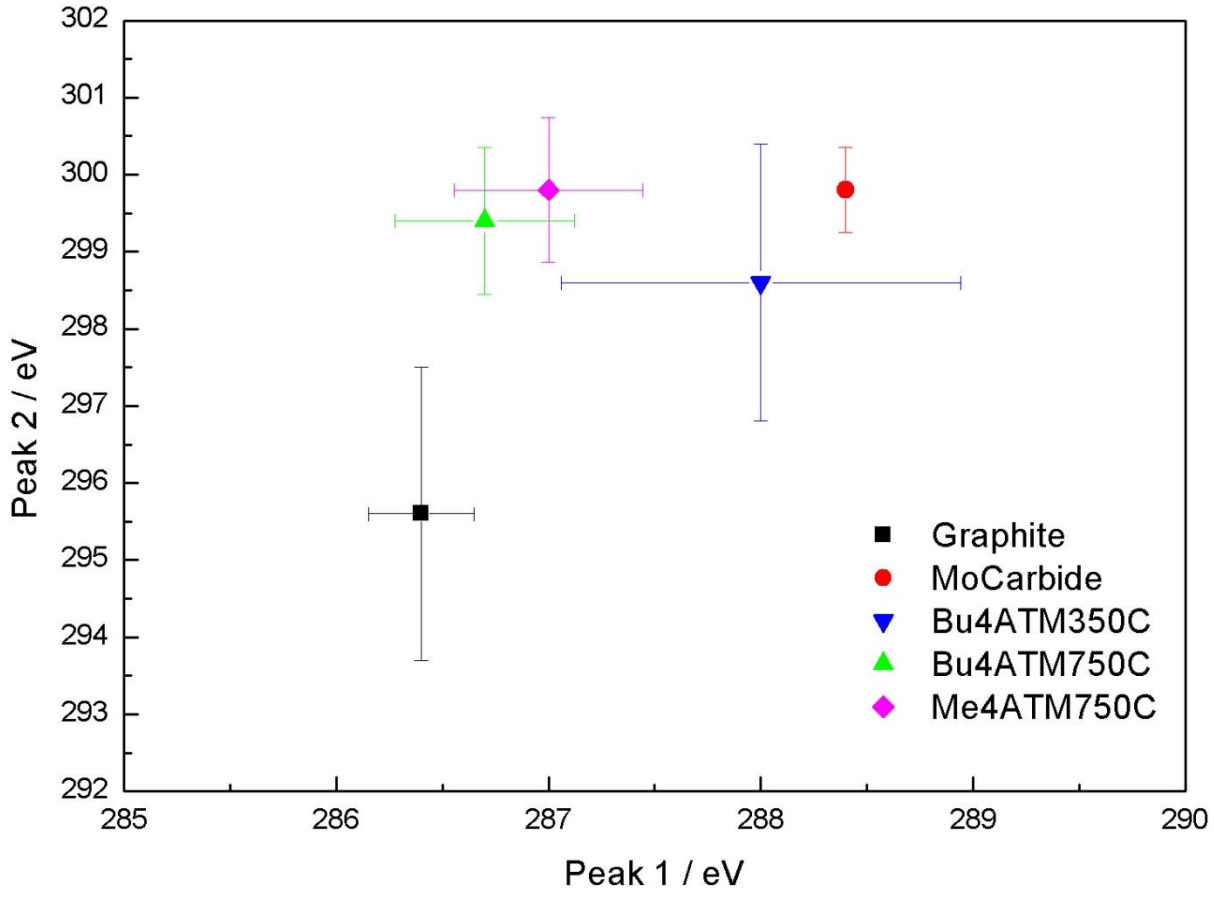

Figure 3.20 *Comparison of the peak positions determined from the EEL spectra of the as prepared MoS_2/carbon composite samples with graphite and molybdenum carbide references. Each value of the peak position is an average from 3~7 different positions in the sample. The corresponding error bar is determined together with the average value of each peak. Both samples decomposed at 750 °C are more close to the graphite reference. The sample Bu_4ATM_350 °C with more carbon content and prepared at lower temperature contain more carbide-like or amorphous carbon, and the characteristic peaks are located more close to the range of the molybdenum carbide.*

Table 3.3 *Peak positions determined from the EEL spectra of the reference samples and literature values of the carbon K-edge in terms of different carbon compounds and bonding states.*

Graphite			**Mo Carbide**			**Literature value[120] (eV)**	**XPS binding energy [121] (eV)**	
Positions	**Peak 1 (eV)**	**Peak 2 (eV)**	**Samples**	**Peak 1 (eV)**	**Peak 2 (eV)**			
						C=C π*	**C-C sp2**	**Mo_2C**
1	286,1	293,8	**MoC**	288,4	299,2	~285	284.3-284.6	282.7
						C-C σ*	**C-C sp3**	**C-S**
2		294,7	**Mo_2C**	288,4	300,3	~292	285.0-286.0	285.2-287.5

						C=C σ*	**Graphite**	**C adsoorbed on MoS2 unsaturated site**:	
3	286,6	298,2				~300	284.3-284.6	285.8	
Average	286,4	295,6	**Average**	288,4	299,8				
Standard deviation	0,25	1,90	**Standard deviation**	0	0,55				

Table 3.4 *Average peak positions calculated from the EEL spectra of different positions of the three as prepared samples*.

Bu_4ATM 350°C			**Bu_4ATM 750°C**				**Me_4ATM 750°C**				
Positions	**Peak 1 (eV)**	**Peak 2 (eV)**	**Positions**	**Peak 1 (eV)**		**Peak 2 (eV)**	**Positions**	**Peak 1 (eV)**	**Fulerite-like feature**	**Peak 2 (eV)**	
1	289,3	301,1	**1**	287,1	296,8	299,8	**1**	287,2	292,7	298,8	301,2
2	287,6	297,1	**2**	287	296,8	301	**2**	286,3	288,7	300,5	
3	287,1	297,5	**3**	286,9		298,1	**3**	286,4		298,3	
			4	286,2	296	299,2	**4**	287,3		300,6	
			5	286,1	295,9	299,1	**5**	287,6		301,1	
							6	287		299,9	
							7	287,2	291,4	299,5	304,3
Average	288	298,6		286,7	296,4	299,4		287	290,9	299,8	
Standard deviation	0,94	1,80		0,42	0,43	0,95		0,44		0,94	

3.5 Summary: MoS_2-based Catalysts

For the $MoS_xC_yP_z$ composite, IFFT calculations based on the HRTEM study clearly visualized the expanded slab distances in the 250 °C sample in real space, and together with other analytic methods an intercalation of phosphorus and carbon containing organic species in between the MoS_2 slabs is confirmed. *In situ* electron beam irradiation shows the instability of the intercalated molecules and decreasing distances of adjacent slabs. Incorporation of different carbon species into the MoS_2 catalyst can lead to a modification of the photocatalytic activity.[9,10] EELS studies on the carbon edges suggest an ordered and graphitic (i.e. sp^2 dominated) carbon species within the 250 °C sample, the origin of which is suggested by NMR and IR showing the π bonding on the phenyl groups incorporated in MoS_2. The intercalation of graphitic carbon inside the 250 °C sample and the nanoslabs with more active sites in the 350 °C sample are considered to be responsible for their higher photocatalytic activities as compared to bulk MoS_2.

For the amorphous MoS_2 (PX) sample, the *in situ* electron beam irradiation and *in situ* thermal annealing inside TEM both lead to an increased crystallinity upon irradiation/heating. Yet the statistic studies via HRTEM images comparing the size distribution of the MoS_2 slabs reveal different crystallization mechanisms of the two pathways. *In situ* electron beam irradiation results in an anisotropic size distribution due to the highly localized heat confinement, while *in situ* thermal annealing produces more uniform crystallites due to better thermal equilibrium achieved via the carbon grid. *Ex situ* heating experiment confirms the *in situ* observation. The inherent coordinatively unsaturated sites inside the amorphous MoS_2 (PX) sample accounts for the high photocatalytic activity.

For the PXCo sample, HRTEM imaging close to atomic resolution allows structural analyses on MoS_2 layers and cobalt promoter particle. Quantitative analyses and computer simulation of the rotational average profiles shows a good agreement with the statistic histogram results. Especially the kinematic and dynamic simulation of the SAED pattern reveals quantitatively the evolution of crystallinity and microstructural arrangement of the MoS_2 phase under HDS reaction.

For the MoS_xC_y composite, EELS analyses prove a mixture of graphitic and carbide-like carbons inside the three samples. By comparing with reference samples of carbides and graphite, higher temperature ensures composite with higher crystallinity and more graphitic feature, while lower temperature promotes more carbide-like feature with poor crystallinity. The results suggest that better synthesis parameters should be adjusted to result in higher purities of the graphitic or carbide-like carbon content, in order to enhance the performances of MoS_xC_y as an electrode material or a catalyst.

4 MoO_3 and SnO_2 based Micro- / Nano-Sensors

Micro-/Nano-particle-based semiconductor devices can drastically reduce the dimension of the devices. In this chapter the structural analysis of MoO_3 and SnO_2 micro-/nano-belts based composite particles is carried out. Furthermore, the influence of *in situ* and *ex situ* thermal annealing to the structure and properties of the SnO_2 composite sample is introduced. Additionally, the sensor performance is briefly discussed with regard to the corresponding microstructures.

4.1 MoO_3 Micro-/Nano-Rods

Quasi 1D structure has unique properties due to its large surface to volume ratio, which accommodates a high percentage of surface atoms. Consequently, its Debye length is comparable to the lateral dimensions. Therefore the conductivity of the quasi-1D structure is strongly dependent on surface reactions.[16] Using TEM to investigate the nature of the surface sites of the quasi 1D strucuture can provide fundamental insights into the atomic and structural origin of surface reactions, thus better understanding the structure-property correlation of the micro-/nano-devices. In this section, the MoO_3 quasi 1D nano-/micro-rod samples are studied by applying high resolution TEM investigation.

4.1.1 Structural and Chemical Investigation via TEM

The MoO_3 particles obtained at 670 °C feature nano-/micro-rods or belts with a high aspect ratio which is revealed by TEM investigations. The length is several micrometers and width 100~200 nm (see **Figure 4.1**(a)). The crystallinity is examined by SAED (cf. inset displays the [100] zone axis of MoO_3 (space group: *Pbnm*)). A preferential crystal growth direction along the *c*-axis of MoO_3 is indicated by the FFT from the HRTEM micrograph (inset in **Figure 4.1**(b)). Furthermore, several EDX elemental investigations performed at various positions on the sample grid shows a marginal deviation from the stoichiometry ratio of Mo : O = 1 : 3. This deviation could be due to the oxygen vacancies generated via a reduction process induced by electron beam irradiation.[122, 123]

For the sample prepared at 800 °C, the TEM micrograph revealed a similar morphology as the sample obtained at 670 °C (see **Figure 4.1**(c)). The SAED pattern exhibits strong dynamic excitation of kinematically forbidden reflections. This phenomenon originates from the enhanced thickness of the nanorod and consequently more pronounced multiple scattering effects. Moreover, the preferential growth direction of the MoO_3 crystal is determined to be along the *c* direction (**Figure 4.1**(d)), which is in agreement with other studies. [124,125,126] In addition, splitting of Bragg reflections perpendicular to the c^* direction is detected in both of the SAED and FFT patterns. Such observation can be due to the formation of planar defects[122], crystallographic shear planes[122] and stacking faults[127]. The first two types of defects are considered to be formed due to electron-beam induced phase transformation of MoO_3.[122]

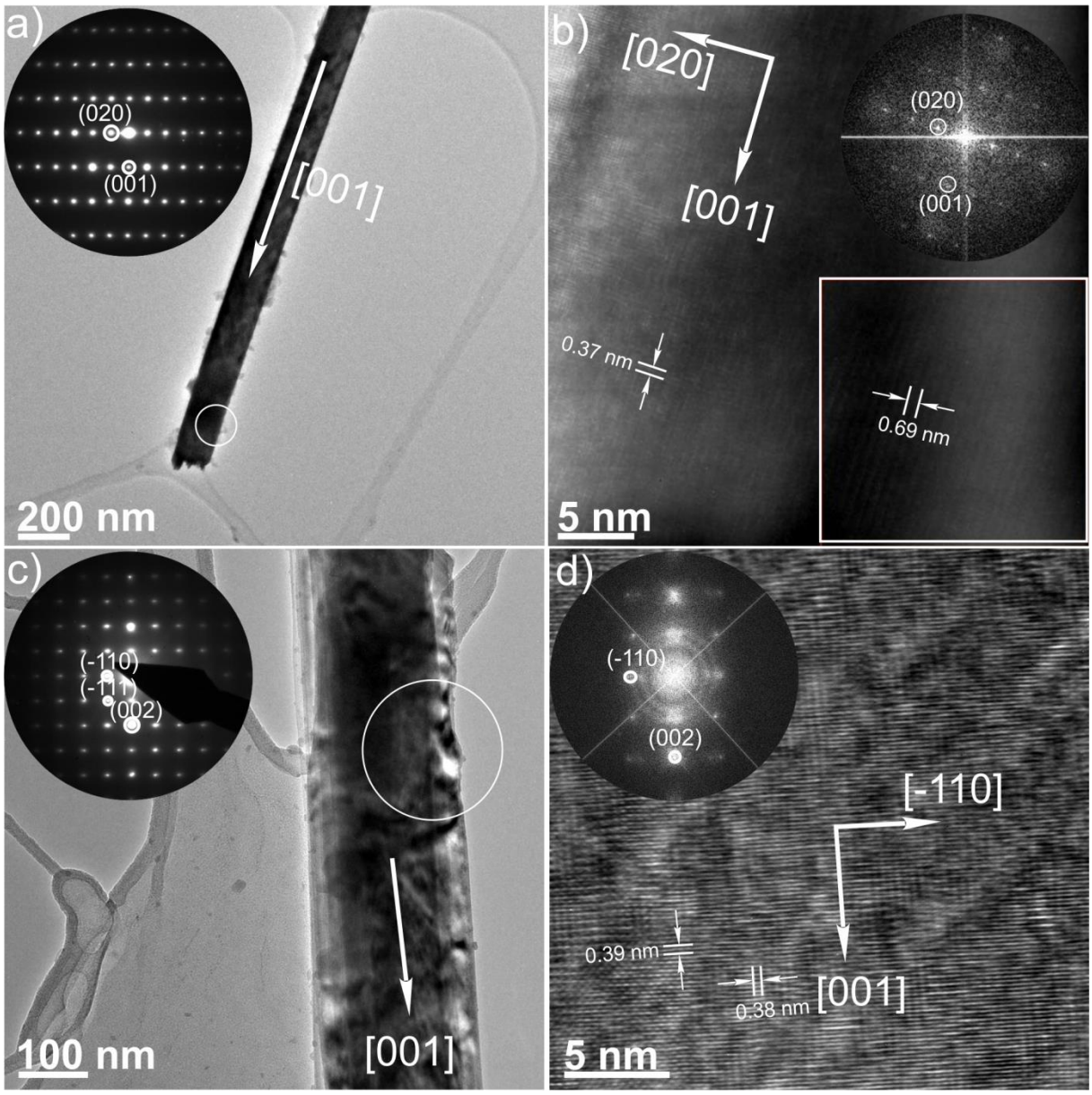

Figure 4.1 *(a) TEM micrographs of a typical MoO_3 nanorod prepared at 670 °C. The inset shows the SAED pattern (zone axis: [100]) from the circled region. (b) HRTEM image from the same spot marked in (a) and the corresponding FFT in the inset calculated from the square marked part. The growth direction of the nanorod is indicated, and the d-spacings of the (001) (0.37 nm |literature value[128]: 0.370 nm) and (020) (0.69 nm |literature value[128]: 0.693 nm) planes are specified. (c) TEM micrograph of a MoO_3 nanorod prepared at 800 °C. The inset presents a SAED pattern (zone axis: [110]) taken from the circled region. (d) HRTEM micrograph from the same position circled out in (c) and the corresponding FFT in the inset. The d-spacings of the (001) (0.39 nm |literature value[128]: 0.370 nm) and (-110) (0.38 nm |literature value[128]: 0.381 nm) planes are shown. (Adapted with permission from ref. 91. Copyright (2014) American Chemical Society.)*

Except for the nanorods with a growth direction along the *c*-axis, in rare cases a few MoO_3 nanorods can grow along the *a*-axis for both synthesis temperatures (see **Figure 4.2**). Nonetheless, the *c*-axis growth direction is preferred according to a statistic evaluation of the TEM observations. This finding agrees with previous study[129] as well as the surface energy

theory[130]. As the surface energy of the (001) plane is the lowest, the MoO_3 nanowires preferentially grow along the *c*-axis instead of other directions such as the *a*-axis.[130]

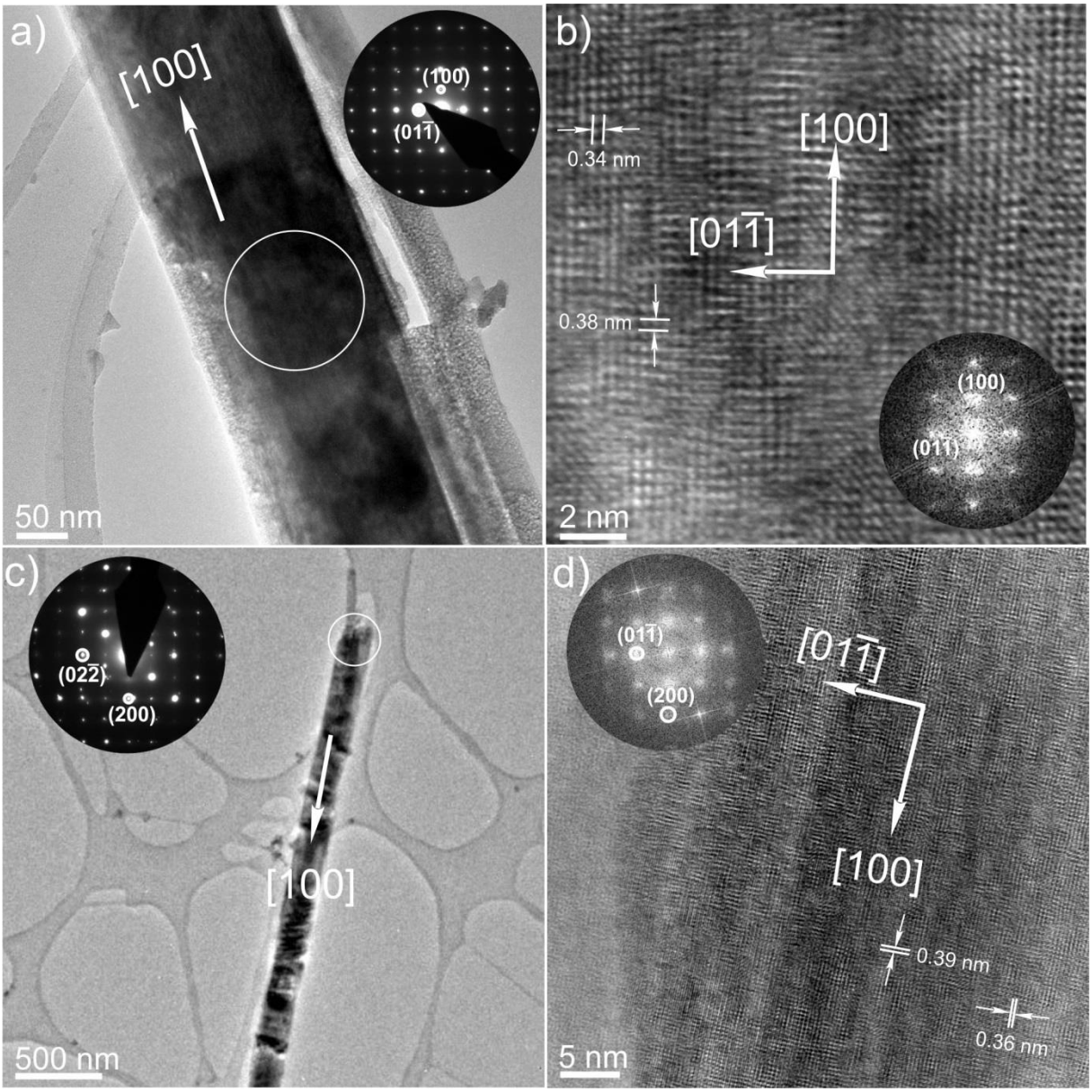

Figure 4.2 *(a) TEM bright-field image of a MoO_3 nanoribbon synthesized at 670 °C with the inset of the corresponding SAED pattern. (b) HRTEM micrograph recorded on the edge of the same region in (a). The inset shows an FFT indicating a growth direction along the a-axis. (c) TEM micrographs of a MoO_3 synthesized at 800 °C with the inset of an SAED pattern. (d) HRTEM micrograph acquired from the same region in (c) and the FFT in the inset indicating the growth direction along the a-axis. (Adapted with permission from ref. 91. Copyright (2014) American Chemical Society.)*

4.1.2 Sensor Response

The characterization of sensor response is performed by *Dr. Oleg Lupan*, which demonstrates a single MoO_3 nanorod based sensor exhibits a superior response to ethanol vapor.[91] Here a are few comments on the structure-property correlation of this nano sensor.

Firstly, two models are proposed to explain the conductance increase of the MoO_3 sensing nanorod upon its exposure to ethanol vapor: [131]

(1) Adsorption of ethanol molecules onto the surface. Subsequently, the molecule donates an electron to the nanorod:

$$C_2H_5OH \rightarrow C_2H_5OH_{(ads)} \rightarrow C_2H_5OH^+_{(ads)} + e^- \qquad \textit{fast}$$

(2) A catalytic reaction between MoO_3 and ethanol. The oxygen which is incorporated within the lattice (i.e. lattice oxygen) oxidizes ethanol, during which oxygen vacancy and free electrons are produced on the nanorod. Consequently, MoO_3 is reduced to lower valence molybdenum ions:

$$C_2H_5OH + O_s \rightarrow CH_3CHO + H_2O + V_o^{2+} + 2e^- \qquad \textit{slow}$$

In the equations above, the subscripts *(ads)* and *(s)* denote to an adsorbed molecule or a surface site, respectively. The reaction proposed in the first model is a fast process compared to the second model. Therefore, reaction (1) is responsible for the short response time of the nanosensor. In reaction (2), the oxygen vacancy and partially reduced Mo ion can be re-oxidized to the initial state. This semi-reversible process accounts for the recovering ability of the sensor after the ethanol vapor stimuli are turned off.

Furthermore, the surface morphology and crystal structure of the MoO_3 nanorod layer have to be taken into account to understand the reaction mechanism of the sensor behavior. The crystalline MoO_3 is considerably defective as disclosed by HRTEM imagining (**Figure 4.1**(b), **Figure 4.2**(b) and (d)). The defects can provide a fair amount of active sites for the absorption of the gas molecule and for the catalytic oxidation process. Unlike other n-type semiconductor gas sensors, e.g. SnO_2 or ZnO, where the oxidation process is facilitated by the surface chemisorbed oxygen, MoO_3 is able to oxidize the gas molecule via its own lattice oxygen.[131,132,133] This difference stems from its structure: the orthorhombic MoO_3 is prone to forming crystallographic shear planes (cf. **Figure 4.1**), which can be facilitated by removing lattice oxygen at the surface.[122] Consequently, the consumption of lattice oxygen during the catalytic oxidation process with ethanol gas is favored by the structural rearrangement of MoO_3.[131]

Moreover, the overall sensor performance of the MoO_3 nanorod towards different gases is highly dependent on the thickness of the nanorod.[91] The sensor response of the thinner nanorod (150 nm) is higher than that of the thicker one (200 nm), because as dimension decreases, the surface-to-volume ratio increases, and the influence of the surface reaction to the conductivity of the nanorod is enhanced.

4.2 SnO_2 / Ga_2O_3 / GaN:O_x Composite

In comparison to single component nanosensors, hybrid nano-composite based devices can exhibit superior performances due to synergistic effect.[134] In this section, a hybrid core-shell nano-/micro-composite based on quasi 1D nanobelts of SnO_2 is introduced. The SnO_2 nanobelt is grown via the FTS method.[61] The outer shell of the nanobelt is composed of gallium compounds deposited by radio frequency (RF) magnetron sputtering approach. The results of TEM structural analysis of the hybrid composite are discussed. The evolution of the structural and chemical properties upon thermal annealing is further studied *ex situ* in ambient atmosphere and *in situ* in TEM, subsequently, the results are compared accordingly.

4.2.1 As Prepared Sample

The TEM micrograph of the as prepared hybrid nanostrucuture is demonstrated in **Figure 4.3**(a). The nanobelt adopts a structure of SnO_2 (core) / GaN:O_x (shell) / β-Ga_2O_3 (shell) as it is further substantiated by chemical analyses via EDX (cf. inset of **Figure 4.3**(a)). The enhanced shell thickness on one side originates from the shadowing effect introduced by sputtering, which is evident by the EFTEM elemental mapping (**Figure 4.3**(b)). The poorly crystalline nature of the shell is confirmed via SAED investigation (**Figure 4.3**(c)). Four Bragg intensities can be asigned to the lattice planes of β-Ga_2O_3 (space group: *C12*/*m1*). Besides, the brightest and broad ring with the largest d-values includes 6 strongest reflections from β-Ga_2O_3, i.e. (111), (-3-11), (002), (-401), (400) and (401) reflections. The findings suggest a presence of a poorly crystalline β-Ga_2O_3 phase. The GaN:O_x phase is believed to be an amorphous gallium oxynitride, i.e. GaN incorporated with extra oxygen. The x value is determined to be ~1.27 before annealing (see **Figure 4.3**(a), inset), and it can be influenced by an annealing process in air to the composite (see **Section 4.2.2**). The existence of GaN:O_x is evident by the stoichiometry ratio calculated from EDX data and by EFTEM elemental mapping as well. The two components of the shell GaN:O_x and β-Ga_2O_3 are believed to be uniformly mixed, i.e. a lateral superposition of these two phases, as no clear interface between them has been observed via HRTEM imaging inside the shell (cf. **Figure 4.4**).

Additionally, the hardly crystalline nature of the shell is further evidenced by HRTEM micrograph (**Figure 4.4**). The interface of the core and the shell region gives an enhanced view of the highly crystalline SnO_2 core covered with a thin outer layer (~10 nm) of Ga_2O_3/GaN:O_x. The single crystallinity of the SnO_2 core is revealed in the FFT pattern in **Figure 4.4**(d), which is indexed to be along the [110] zone axis of SnO_2 (space group: $P4_2/mnm$).

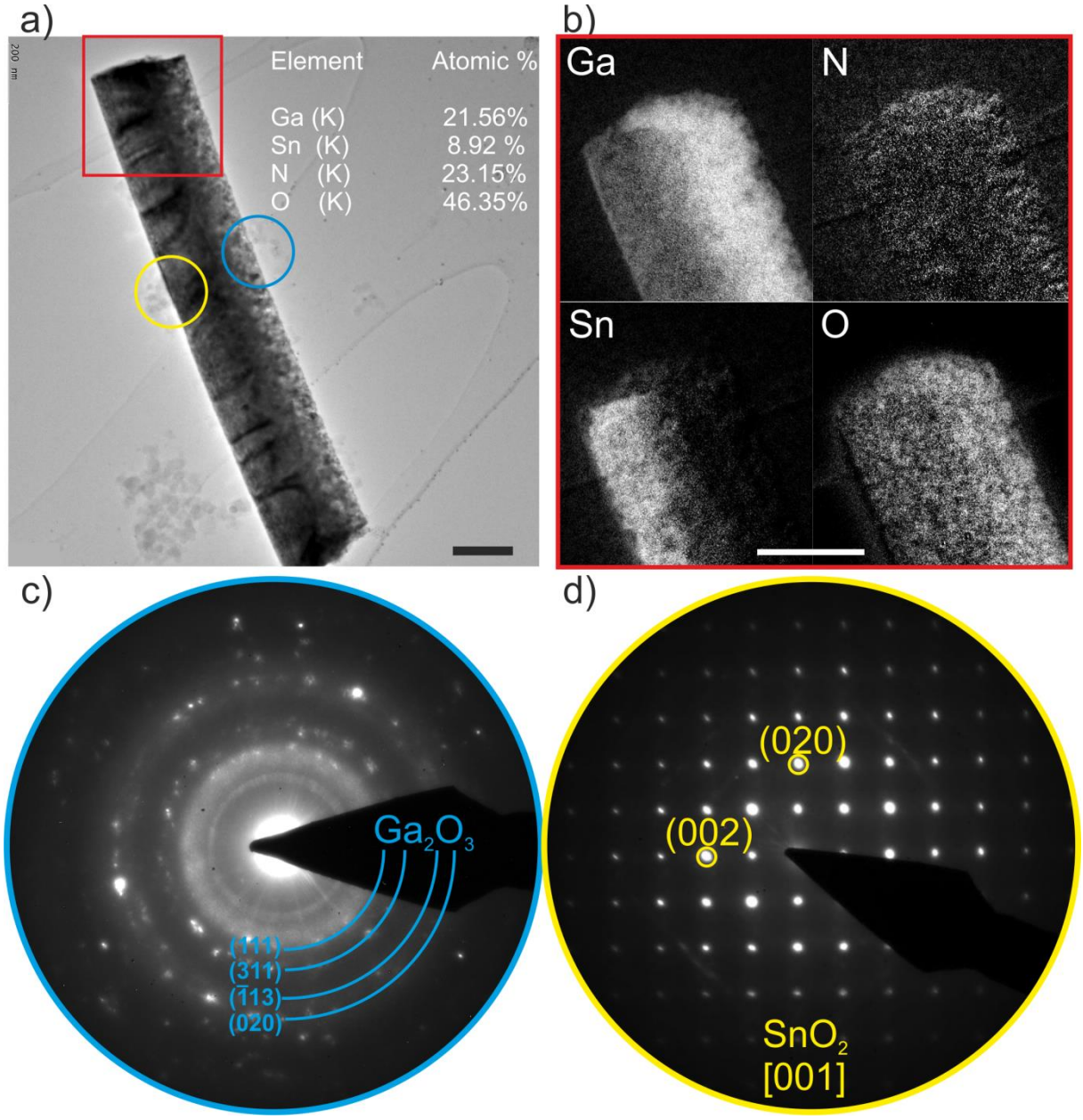

Figure 4.3 *(a) TEM micrograph of an as prepared single core-shell nanobelt. Inset: the corresponding elemental composition of the whole nanobelt confirmed via EDX study. (b) EFTEM elemental maps from the region which is marked with a red square, indicating an incorporation of the Ga, O and N in the shell. (c) SAED pattern recorded from the shell region of the nanobelt marked with a blue circle in (a). (d) SAED pattern from the SnO_2 core region marked with a yellow circle in (a). Scale bar is 0.2 µm.*

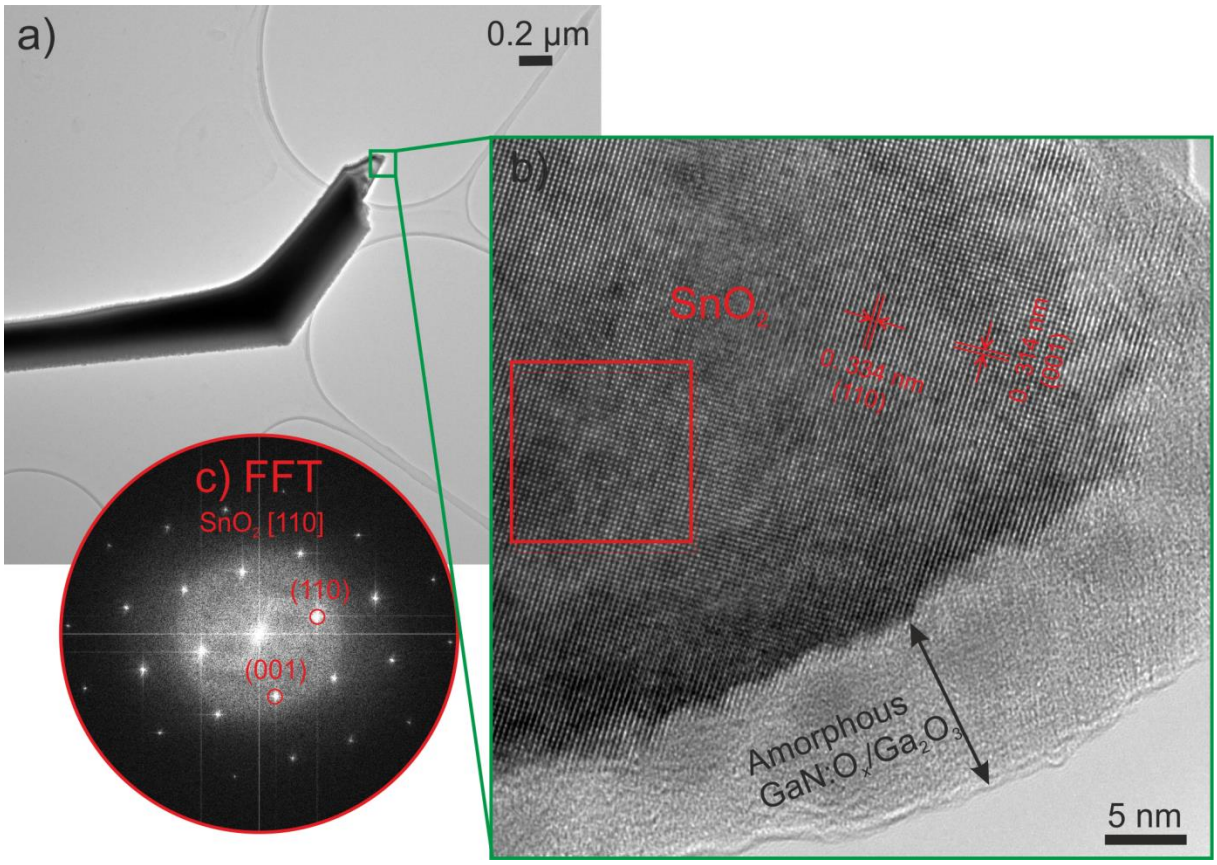

Figure 4.4 *(a) TEM bright field image recorded on a tip of a hybrid nanobelt. (b) HRTEM micrograph of the area marked with a red square in (a). The lattice fringes are present in the inner region of the composite interface. The (110) and (001) lattice planes of crystalline SnO_2 are indicated. The outer region is a thin layer (~ 10 nm) of poorly crystalline Ga_2O_3/GaN:O_x shell. (c) FFT pattern calculated from the area marked with a red square in (b), showing a projection along the zone axis [110] of SnO_2.*

4.2.2 *Ex situ* Annealing on As Prepared Sample

In order to explore possible methods to improve the crytallinity of the shell in the composite nanobelt, several annealing processes are applied. Firstly, an *ex situ* thermal annealing process was conducted on as prepared core-shell nanobelts in air at 700 °C for 90 min by *Dr. Oleg Lupan*. The annealed composite nanobelt remains the core-shell hybrid structure (**Figure 4.5**(a)). HRTEM imaging on the outer shell revealed the polycrystalline nature (see **Figure 4.5**(b)). One of the nanocrystallites around ~10 nm was imaged along the zone axis [010] of β-Ga_2O_3. The enlarged region exhibits lattice fringes of the (200) plane of β-Ga_2O_3 (**Figure 4.5**(b^{i})). The d-values determined from the FFT pattern (**Figure 4.5**(b^{ii})) agree well with β-Ga_2O_3 (literature[135] and experimental d-values: $d_{(200)}$ = 0.594 nm|0.60 nm, $d_{(201)}$ = 0.367 nm|0.37 nm.). Indeed, the crystallinity of the shell improved after *ex situ* annealing as indicated from the SAED pattern in **Figure 4.5**(c): The number of the reflection rings increased. All the Bragg intensities can be assigned to β-Ga_2O_3 as marked out with red arcs. However, the GaN:O_x phase remains amorphous since high temperature and high pressure is required for producing crystalline GaN:O_x.[136,137] As compared to the GaN:O_x phase before

annealing, it has higher content of oxygen incorporation, i.e. x=2.9 as calculated from the EDX result shown in **Figure 4.5**(a). Yet the excessive oxygen content should include contributions from chemisorbed (-OH) group on the shell and surface oxygen on SnO_2[138], therefore the charge balance criterion is not the only explanation to rationalize the extra oxygen. In addition, the oxygen can be partially contributed from the carbon grid due to an error of the manufacturer, which is just noticed during the last phase of this thesis. Furthermore, as the ring pattern shows no texture, it could be concluded the β-Ga_2O_3 nanocrystals on the surface exhibit no preferential orientation to the SnO_2 core. In addition, **Figure 4.5**(d) depicts the SAED pattern along the [2-10] zone axis of SnO_2, signifying the unchanged single crystallinity of the SnO_2 core after *ex situ* annealing.

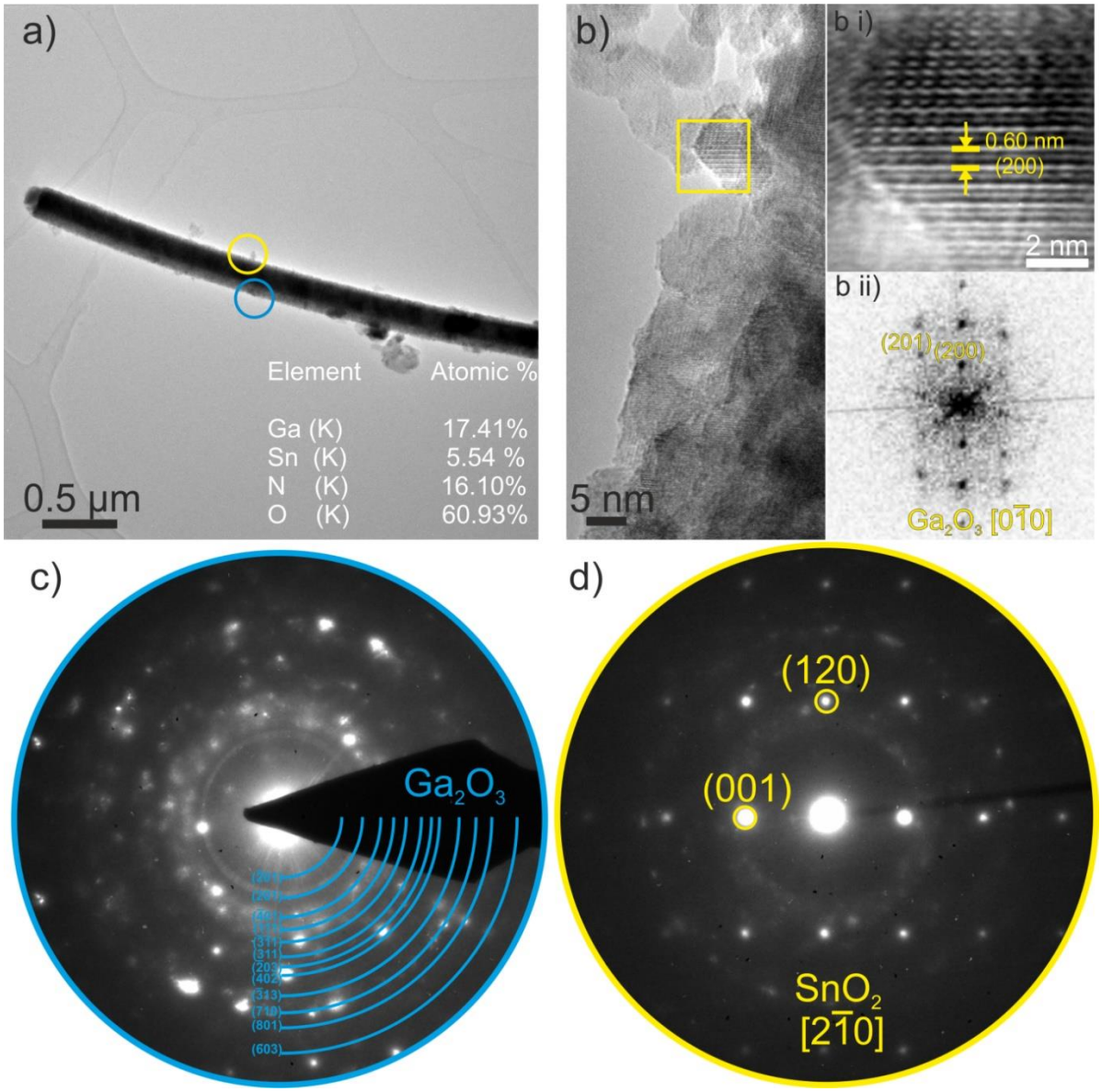

Figure 4.5 *(a)TEM micrograph of a core-shell nanobelt after ex situ annealing and the corresponding EDX elemental result from the whole nanorod in the inset. (b) HRTEM micrograph of a region of the shell. (b^i) Enlarged HRTEM micrograph from the area marked with a yellow square in (b). The (200) plane of Ga_2O_3 and its d-spacing are indicated. (b^{ii}) Corresponding FFT pattern calculated from (b^i) indexed to be along the [0-10] zone axis of Ga_2O_3. (c) SAED pattern from the shell region with a blue circle in (a). (d) SAED pattern from the SnO_2 nanobelt side marked with a yellow circle in (a).*

Furthermore, HAADF-STEM-EDX nanoprobe line scan investigation proves no clear separation between β-Ga_2O_3 and GaN:O_x in the shell (see **Figure 4.6**). The plot in **Figure 4.6**(b) depicts the Ga, N and O elements following almost the same distribution profile on a line scan across a core-shell nanobelt. The oxygen profile (blue curve) exhibits an increase of the slope after ~70 nm as compared to the nitrogen profile (green curve). This phenomenon is due to the contribution from SnO_2 core. The thickness of the shell on the left side (30~70 nm region on the x-axis) is larger than the other (175~230 nm region on the x-axis), as it can be estimated by the lower contrast of the HAADF-STEM image (cf. the profile of image contrast shown in **Figure 4.6**(b): red curve). Accordingly, the signals of the light O and N elements are slightly suppressed on the thicker side due to an enhanced adsorption effect. Note that, the probe size of the electron beam in STEM mode is ~1 nm, therefore, the elemental profile over a nanobelt with a width of 200 nm can be clearly resolved. The superposition of the profiles is not due to the limitation from the lateral resolution of the microscope, but rather a superposition of the Ga_2O_3 and GaN:O_x phases on the shell region of the nanobelt.

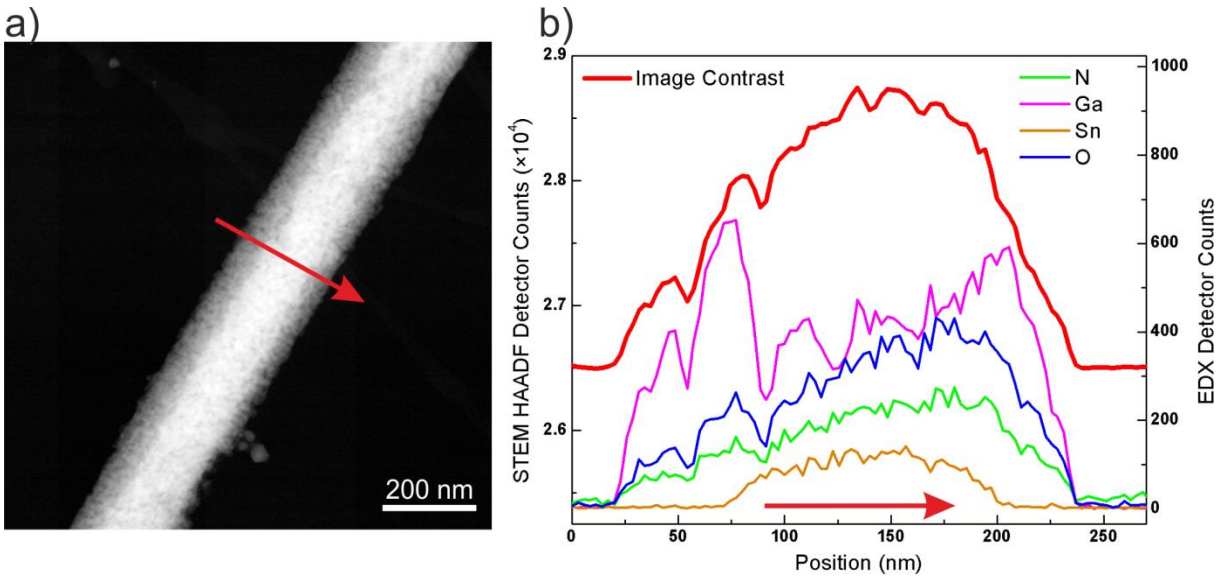

Figure 4.6 *(a) HAADF-STEM image of a core-shell nanobelt after ex situ annealing. The core with a higher contrast is the SnO_2 nanobelt. The shell exhibits a lower contrast due to its smaller thickness and porous structure. The red arrow indicates the position and the direction where the EDX nanoprobe line scan was conducted. (b) Line scan profiles of the electron counts detected by EDX and STEM-HAADF detector from the arrow indicated pathway in (a). The same orange arrow below the profiles denotes the progressing direction of the nanoprobe.*

4.2.3 *In situ* Annealing inside TEM

A further *in situ* annealing experiment is carried out inside TEM to compare with the *ex situ* annealing. *In situ* experiment inside TEM will provide the possibility to better understand the dynamic progress for the enhanced crystallinity of the sample upon heating. The heating ramp is 20 °C / min^{-1}. Starting from 700 °C, the temperature is hold for 10 min both at 700 °C and 800 °C for a stable and comparable annealing with respect to the *ex situ* experiment.

The heating series are shown in **Figure 4.7**. The SAED patterns are recorded from the shell part of a nanocomposite belt at every 100 °C. At 300 °C, the region of interest is still poorly crystalline, as indicated by the faint and diffuse reflection. The strong Bragg intensities are produced by the single crystalline SnO_2 nanobelt due to its thermal drifting inside the SAED aperture during acquisition. Starting from 400 °C, the initial crystallization of the shell is detected. The strongest (111) reflection from β-Ga_2O_3 is present. Furthermore, the broad and bright circle with larger d-spacings between the (-401) and (111) reflections is the region with the four most intense reflections of β-Ga_2O_3, i.e. (111), (-3-11), (002), (-401). However, the crystallinity is still low and the d-spacings of those rings are too diffuse to be resolved. Hence, the innermost (-401) ring is marked with a dashed line. From 500 °C to 800 °C, more reflections appear, indicating an enhanced crystallinity of the shell. Upon annealing at 800 °C for 10 min, the SAED pattern evolves into a typical polycrystalline pattern with multiple rings assigned to β-Ga_2O_3. The reflections can also be assigned to a spinel type of gallium oxonitride, i.e. Ga_3O_3N[136]. Since a high temperature and pressure condition is necessary to form crystalline gallium oxynitride,[136] it is highly unlikely to occur under the condition of *in situ* heating inside TEM.

The observation from the *in situ* annealing experiment verifies poorly crystalline Ga_2O_3 phase is present before annealing and the lattices became more ordered after annealing. However, as further confirmed in HRTEM micrograph in **Figure 4.8**, the GaN:O_x phase seems to remain amorphous even when heated up to 800 °C. This finding is consistent with the results of *ex situ* heating.

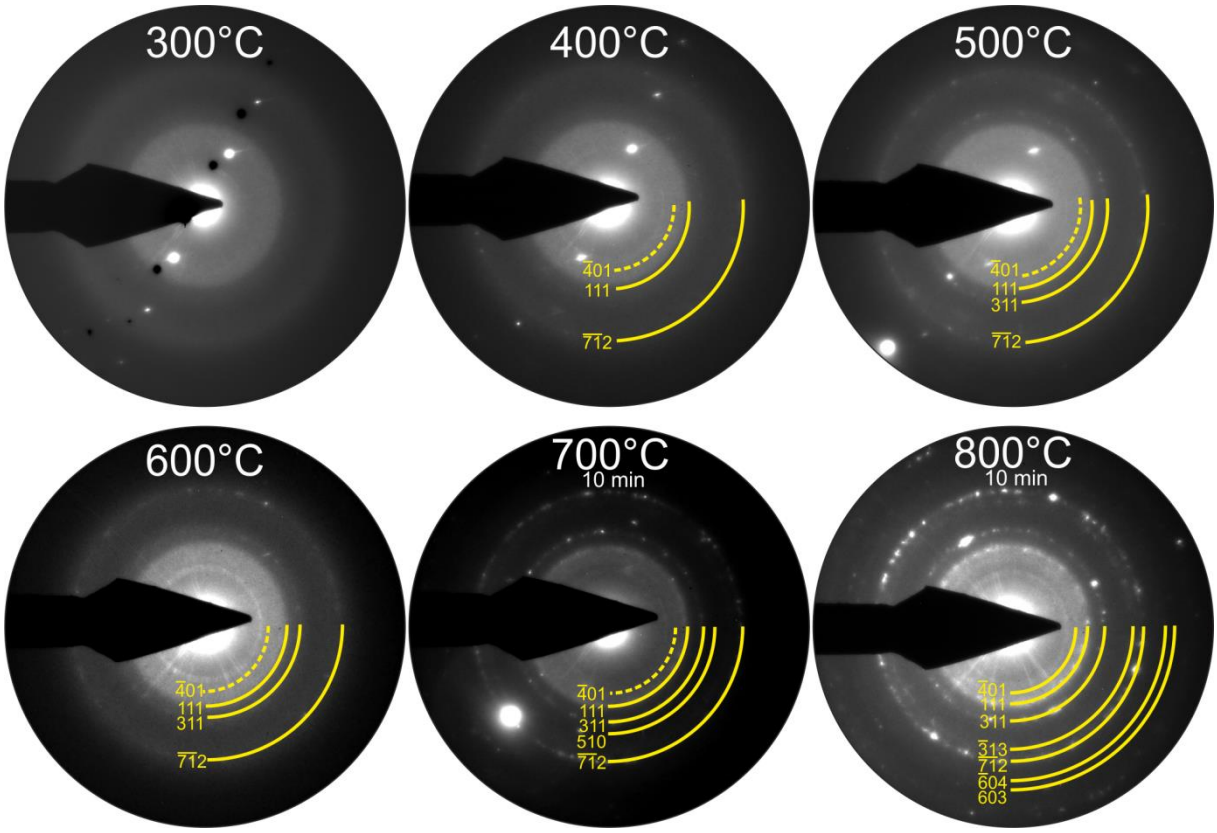

Figure 4.7 *In situ heating series of SAED patterns acquired on the shell region of an as prepared core-shell nanobelt show an increased crystallinity upon heating. The reflections are assigned to lattice planes of β-Ga_2O_3.*

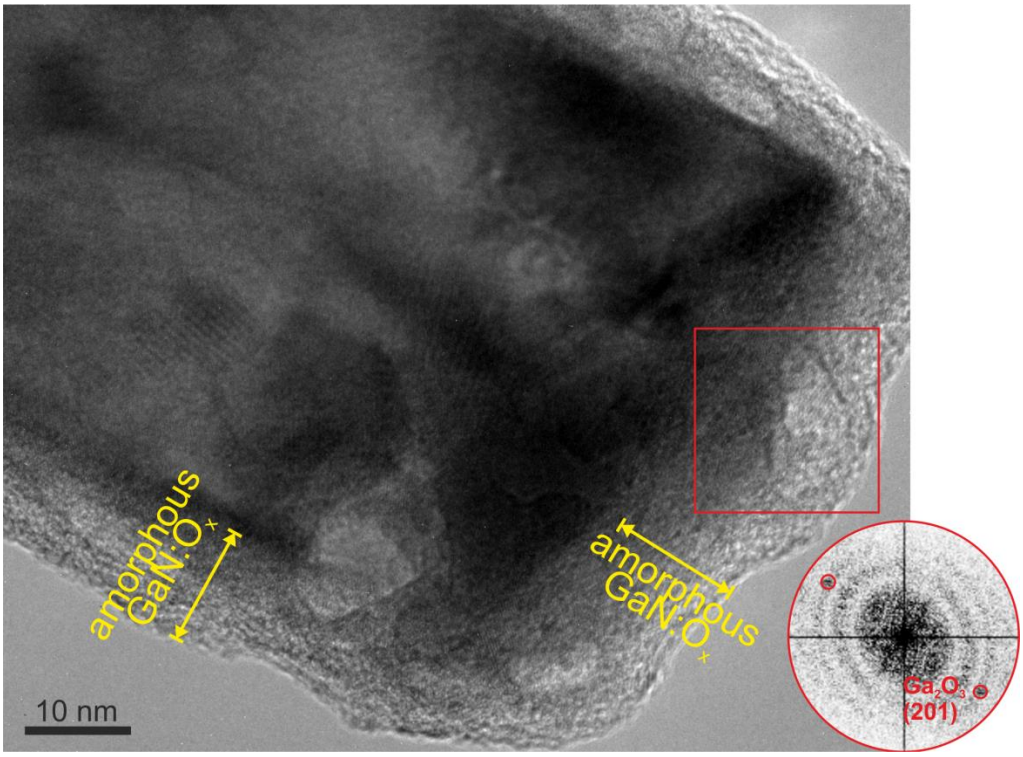

Figure 4.8 *HRTEM micrograph of a core-shell nanobelt after in situ annealing. The regions of the outer shell which remain mostly amorphous consist of GaN:O_x (marked with yellow arrows). Another area in the shell signified with a red square exhibits lattice fringes with a d-value of 0.36 nm (theoretical value: 0.367 nm[135]). Inset show the corresponding FFT from the crystalline region. The reflections indicate the characteristic d-spacing of β-Ga_2O_3 (201) plane.*

4.3 Summary: MoO_3 and SnO_2 based Micro- / Nano-Sensors

For the MoO_3 micro-/nano-rods, TEM structural and compositional studies reveal the growth direction and the highly defective structure of the orthorhombic MoO_3. The detection response of the MoO_3 micro-/nano-rods sensor toward ethanol vapor is related to the surface catalytic reaction on the lattice oxygen of MoO_3, which is further facilitated by the defect rearrangement of the crystallographic structure. The fast gas response is closely related to the dimension of the MoO_3 micro-/nano-rods. Therefore, the structure-property relation of the MoO_3 micro-/nano-rods is revealed by TEM.

For the SnO_2(core)/Ga_2O_3(shell)/GaN:O_x(shell) composite, since the shell is further considered to play a pivotal role for protecting the soft SnO_2 core and to provide synergic sensor responses,[134] a comprehensive TEM study including EFTEM, SAED, HRTEM and *in situ* heating is applied to reveal the complex compositions of the shell. The influences of thermal annealing are demonstrated via *ex situ* and *in situ* experiments, where an increased crystallinity of Ga_2O_3 is detected while GaN:O_x remains amorphous.

5 Aerographite, Aerographite-based Composite and Aero-Gallium Nitride (GaN)

As already mentioned in the Motivation and **Section 2.3**, the correlation of the structure and property is highly demanding for TEM to reveal the detailed structure of the micro-/nano-carbon materials. Accordingly in this chapter, the characterization of structural and chemical properties of a novel carbon microtube material, i.e. Aerographite (AG) and its high temperature variants and its GaN variant 'Aero-GaN', is discussed. In addition, a composite material GaN/AG is introduced. Furthermore, a systematic application of EELS techniques will be established to explore the local bonding states of carbon atoms in AG variants.

5.1 A comparative EELS Study on Aerographite applying Different Acceleration Voltage

The modification of carbon materials, e.g. sputtering, knock-on damage, etc., introduced by high energy electron beam is well known,[139] which arises as a challenge for TEM characterization. A comparative study of the influences by the incident beam with different acceleration voltages to the carbon new material AG is especially of importance. As shown in **Figure 5.1**, the EEL spectra of AG and of a lacey carbon (LC) film exhibit two characteristic peaks on the carbon K-edge: (1) The π* peak with an edge onset from ~284 eV, (2) The σ* peak which extends from 290 ~ 310 eV. The onset of the two peaks in the spectra acquired both at 80 kV and 300 kV is at the same energy loss. However, the maximum of the π* peak in the spectra acquired at 80 kV is at 285 eV, while that of the spectra obtained at 300 kV shifts to 286~287.5 eV. The shifting could be due to beam damage. Furthermore, the π* peaks in the 300 kV spectra are broadened and less intense than those in the 80 kV spectra, which indicates a lower concentration of the sp^2 bonding of the Aerographite.

A quantitative examination of the EEL spectra is carried out by comparing the intensity ratio of the π* / σ* peaks. The π* / σ* peak ratio of AG is always higher than that of the lacey carbon film (AG: 0.66 (300 kV), 0.69 (80 kV); LC: 0.59 (300 kV), 0.54 (80 kV)), indicating a more ordered carbon phase and a higher fraction of sp^2 bonding within AG. Furthermore, the ratio of the π* / σ* peaks in AG is decreasing while the acceleration voltage of the electron beam increased from 80 kV to 300 kV, which suggests a phase with a higher concentration of amorphous carbon for the sample observed under the 300 kV beam. This observation can be ascribed to the knock-on damage by the high energy electron beam, resulting in an amorphization of the specimen. However, the π* / σ* peak ratio of the lacey carbon shows a higher value at higher acceleration voltage, which is seemingly contradicting to the beam damage assumption. The reason can be the inhomogeneity of the lacey carbon films, as the ratio is found to be varying from 0.54 to 0.57 within different sample grids as well.

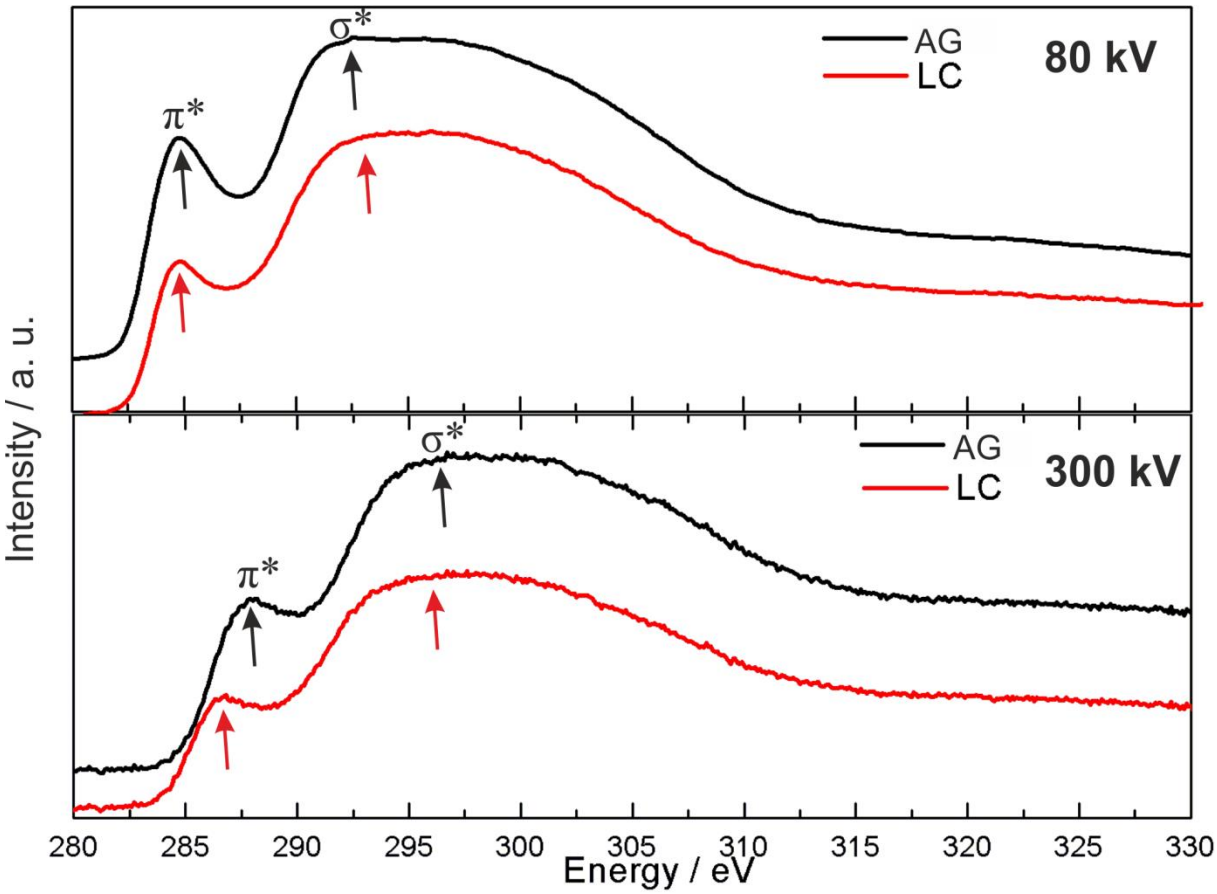

Figure 5.1 *A comparison of EEL spectra on Aerographite (AG) and amorphous lacey carbon (LC) by using different accelerating voltage (upper: 80 kV, lower: 300 kV). The π* and σ* peaks are marked out with arrows.*

5.2 EELS on High Temperature Deposited Amorphous Carbon

The amorphous carbon samples are prepared and annealed for 3 hours and 10 hours, respectively. Both EEL spectra of the carbon K-edge at high energy loss region (280 ~ 350 eV) and low energy loss region (0 ~ 50 eV) are investigated. The spectra are compared with reference samples and literature data to obtain better understanding of the nature of the carbon bonding state within the as prepared samples.

5.2.1 High Loss EEL Spectra

A comparison of EEL spectra from the high loss region of the carbon K-edge is depicted in **Figure 5.2**. The sample prepared for 3h exhibits a less pronounced π* peak and a more featureless σ* peak as compared to that of the sample prepared for 10h, suggesting a less ordered structure of the carbon inside the former sample. However, when compared with the spectrum of the amorphous lacey carbon, the sample prepared for 3h still exhibits a more defined π* peak. This observation implies the structure ordering of the two samples is more prominent than the amorphous lacy carbon. The less noisy spectrum of the lacey carbon sample is probably due to two reasons: (1) The energy dispersion for acquiring this spectrum is larger. (2) The lacey carbon film might be thinner and lead to more transmitted electrons and higher signal to noise ratio.

For the sample prepared for 10 h, the main features of the spectrum are very similar to that of the graphite reference sample. However, they shift to higher energy loss. This change can be ascribed to a longer synthesis duration which can result in a carbon structure close to the insulating allotrope of carbon, i.e. diamond.119 Moreover, the positions of the π* peak (286.1 eV) of the 10 h sample is closer to the literature values of amorphous diamond (286.6 eV)[140], and its σ* peak (293.9 eV) is close to that of diamond (292.3 eV)[141]. This finding suggests a diamond-like structure within the sample. Since a highly ordered diamond shows only a σ* peak due to the pure tetragonal sp^3 bonding within carbon atoms, the residual π* peak at 286.1 eV suggests a mixture of graphite-like and diamond-like carbon species inside the 10 h sample.[140] Nevertheless, longer crystallization time for growing the sample can probably produce carbon phases with more ordered structures as compared to the amorphous carbon reference and the sample prepared in 3 h.

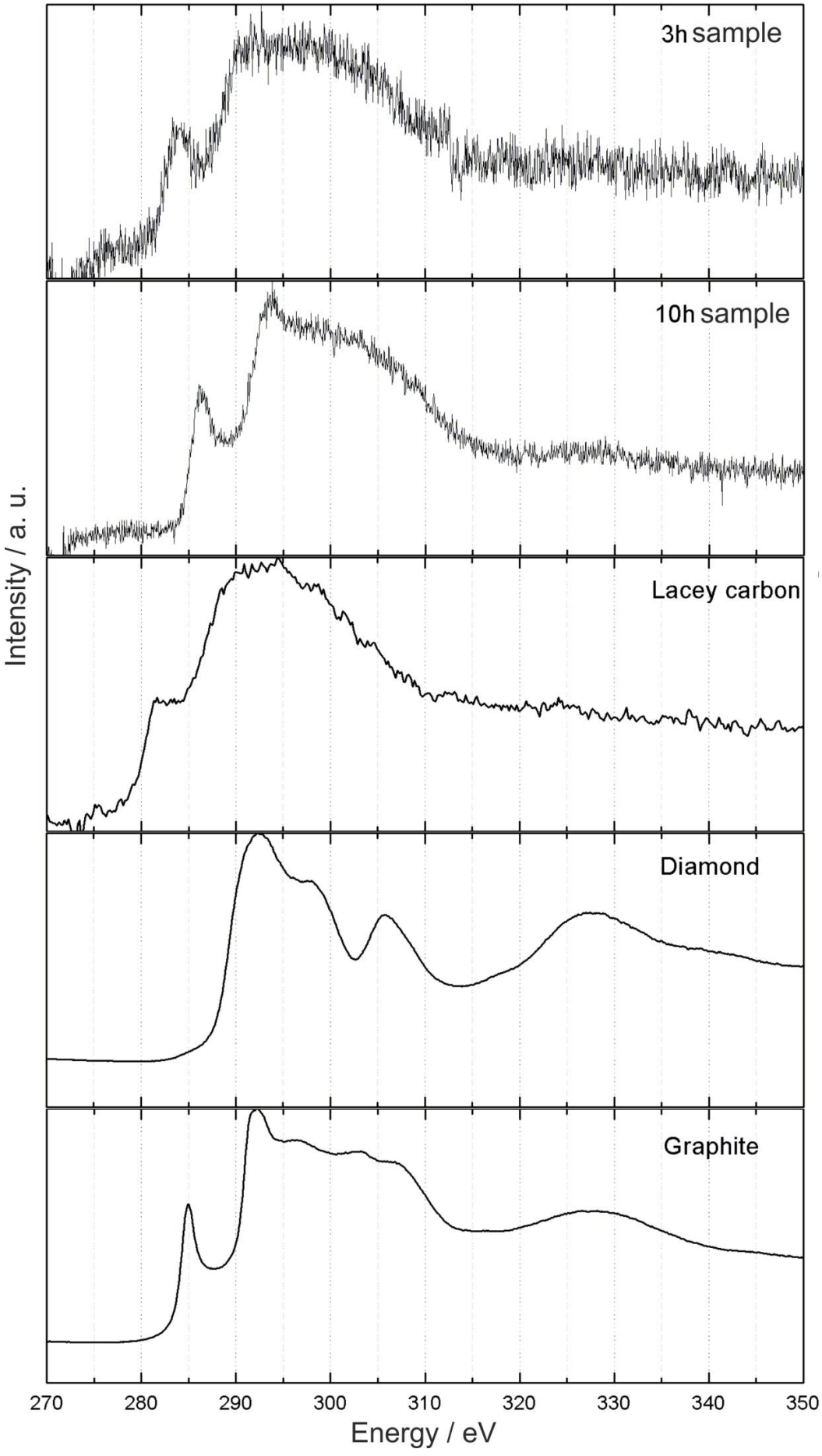
3h sample
10h sample
Lacey carbon
Diamond
Graphite
Intensity / a. u.
270
280
290
300
310
320
330
340
350
Energy / eV

Figure 5.2 *High loss EEL spectra of the as prepared sample for 3h and 10h, of a reference lacey carbon film, and literature data replotted from the references of diamond[141] and graphite[142]. The indent at around 313 eV in the EEL spectrum of the 3 h sample is an artifact due to the dark current from the diode of the GIF CCD camera.*

5.2.2 Low Loss EEL Spectra

While the EEL spectra at high energy loss region can suffer from a systematic shifting due to the sensitivity of the zero loss peak to the environment and to different calibrations of the spectrometer, the low loss EEL spectra can provide accurate locations for characteristic peaks in the plasma region. Therefore, an investigation in the low loss region is a complimentary method to further compensate the observations made in the high loss EEL spectra.

As shown in **Figure 5.3**, the low loss region of the graphite EEL spectra displays a peak at 5.5 eV which is a result of the excitation of π electrons, and another peak at 24.7 eV due to (π+σ) electron excitations.[26] The spectrum of the as prepared sample for 10 h exhibits similar peaks but the (π+σ) peak shifted to lower energy loss (see **Table 5.1**). The spectrum of the sample prepared for 3 h only shows a shoulder at around 5 eV, and a (π+σ) peak at even lower energy as compared to the 10 h sample. The shift of the (π+σ) peak to lower energy loss can be an effect of a lower mass density of the sample.[26] In the case of lacey carbon, the position of the (π+σ) peak is very close to the literature value. However, the π peak is absent which is mostly due to the high intensity of the primary beam that probably hide this feature within the unconvoluted zero loss peak. The spectrum of diamond from literature data is different from those of the as prepared samples and graphite, where only one plasmon peak is present at around 33.8 eV. Further literature data revealed that even amorphous diamond only displays a peak at 30 eV[26], which is different from the observation of the as prepared samples. Therefore, from the low loss region spectra, the as prepared samples can be considered to contain mostly graphite-like carbon. Combining this finding and those are indicated by the high loss EELS data (Section **5.2.1**), it can be conclude that a mixture of both graphite- and diamond-like carbon species is present in the as prepared carbon samples.

Table 5.1 *Peak positions of the low loss EEL spectra of the as prepared carbon samples in comparison with experimental data from reference samples and from literature.*

Sample	π→π* peak (eV)	Plasmon Peak (eV)	Literature value[26]	π→π* peak (eV)	Plasmon Peak (eV)
3h	~ 5	21.2	Diamond	-	33.8
10h	5.5	21.9	Amorphous carbon	4.8	23.6
LC	-	23.2	Graphitized carbon	6.2	26.0
Graphite (700 °C)	5.5	24.7			

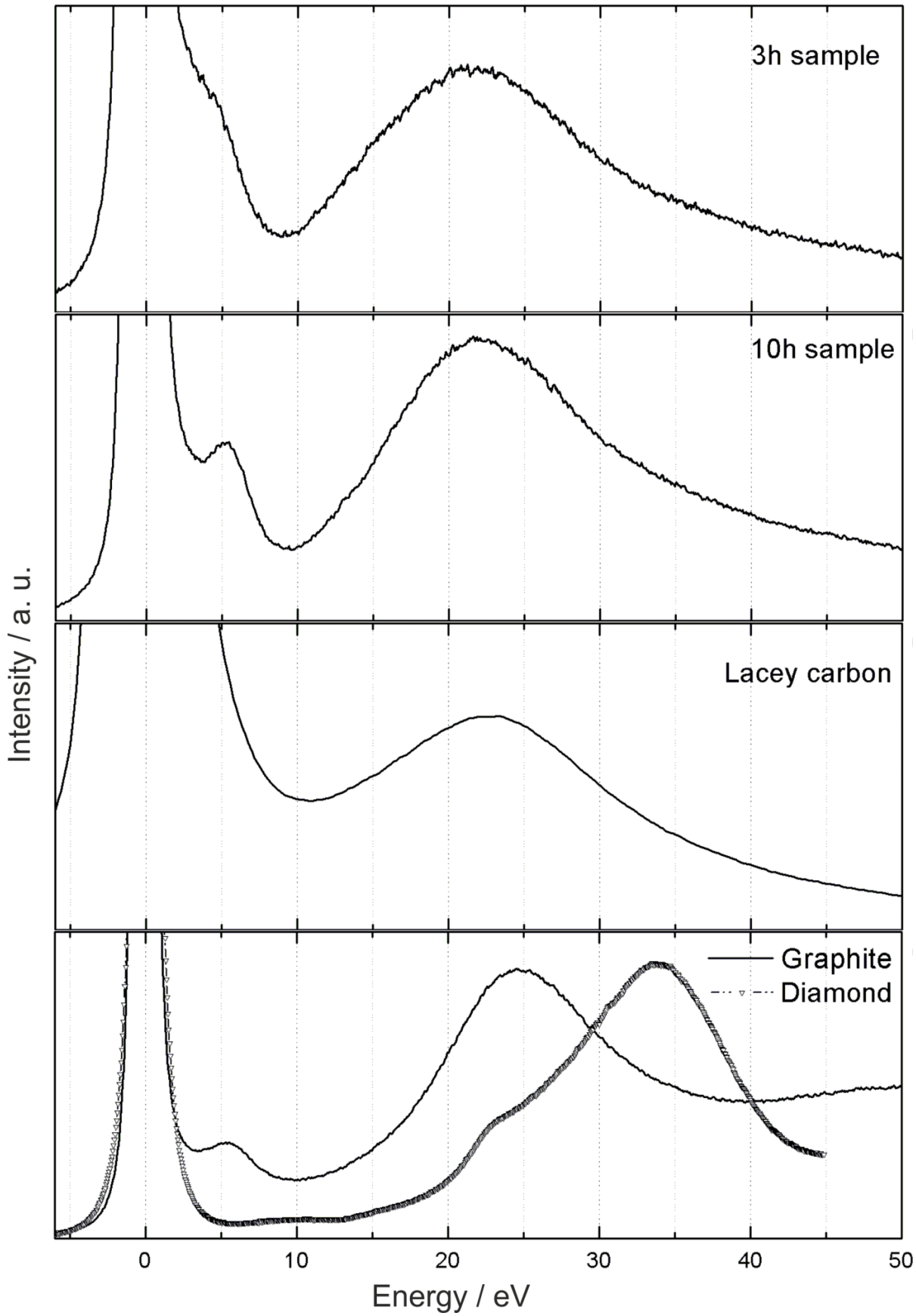

Figure 5.3 *Low loss EEL spectra of the as prepared 3h and 10h samples, of reference samples of a lacey carbon film and a graphite sample, and literature data from diamond (dashed line with symbols, replotted from ref. 141).*

5.3 Aerographite / Gallium Nitride Composite

Gallium nitride (GaN) is a direct bandgap semiconductor with a wide bandgap ~ 3.4 eV, and its nano-/micro-structures are promising materials for the electronic, photonic and piezotronic nano-devices.[63] Epitaxial growth of GaN onto a crystalline substrate is considered so far the most viable method for obtaining GaN nanocrystals.[63] Applying AG network as a substrate to grow GaN nano-/micro-crystallites can overcome the lattice matching issue occurring in the case of epitaxial growth. Furthermore, the high flexibility of AG backbone renders the GaN composite ready to be integrated into any micro device with various length scales.[63]

5.3.1 Fundamental TEM Characterization

A composite particle of GaN crystallites deposited on the outer layer of an AG tetrapod is demonstrated in **Figure 5.4**(a). The soft and thin graphite tubes kept their structural integrity without collapsing when the GaN clusters are attached. Furthermore, preferred growth or texture of the GaN crystallites was excluded based on SEM morphology investigations and XRD structural analysis on a larger scale. By applying SAED, the single crystallinity of the GaN particles is visualized (see **Figure 5.4**(b)): The SAED pattern is recorded at the circular marked area in **Figure 5.4**(a) and is indexed to be along the [100] zone axis of GaN (space group: $P6_3mc$). The smeared diffraction spots of the GaN phase indicate a defect rich structure. Apart from the Bragg intensities, three diffuse rings are displayed in the SAED pattern. These diffuse rings can be assigned to the (002), (011), (-122) planes of carbon (space group: $P6_3/mmc$), which originates from the AG substrate underneath. Hence, a poor crystallinity of AG is confirmed.

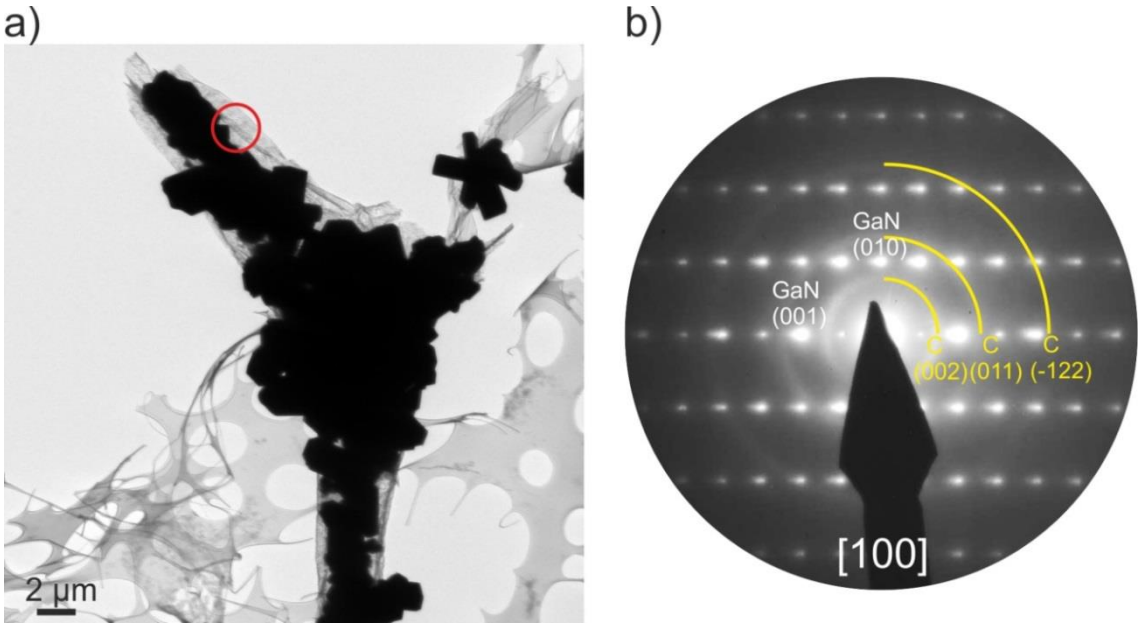

Figure 5.4 *(a) TEM bright field image of GaN crystalline clusters deposited on an AG tetrapod. (b) SAED pattern acquired from the marked area in (a). The single crystalline diffraction pattern is determined to be along the GaN [100] zone axis. The additional three diffuse rings (marked with yellow arcs) are correlated to the (002), (011), (-122) planes of carbon.*

5.3.2 Energy Filtered TEM Elemental Mapping of the AG/GaN Composite

Since the synthesis process of the AG/GaN composite includes a reduction step to eliminate the ZnO template, it is important to examine the possible ZnO residue in the as prepared composite. The as deposited GaN phase (a=3.1620 Å, c=5.1420 Å)[143] and the ZnO phase for the template (space group: $P6_3mc$, a=3.2494(2) Å, c=5.2054(2) Å)[144] have the same crystallographic symmetry and similar lattice parameters. Therefore, rather than the structural study (see **Figure 5.5**(b) and (c)), it is essential to detect the Zn residue via advanced approach with elemental sensitivity, e.g. via EFTEM investigations to distinguish between GaN and ZnO phases. The EFTEM elemental maps in **Figure 5.5**(d-f) reveal Ga and N elements. No Zn or O is detected. The weaker contrast in the Nitrogen map arises from the much narrower energy window applied for the Nitrogen L-edge, where less transmitted electrons contribute to the map and lower the signal to noise ratio. Another reason can be assigned to the enhanced thickness of the GaN crystallites. In conclusion, the comprehensive results of structural and chemical investigations demonstrated a successful synthesis of a novel composite of crystalline GaN on AG.

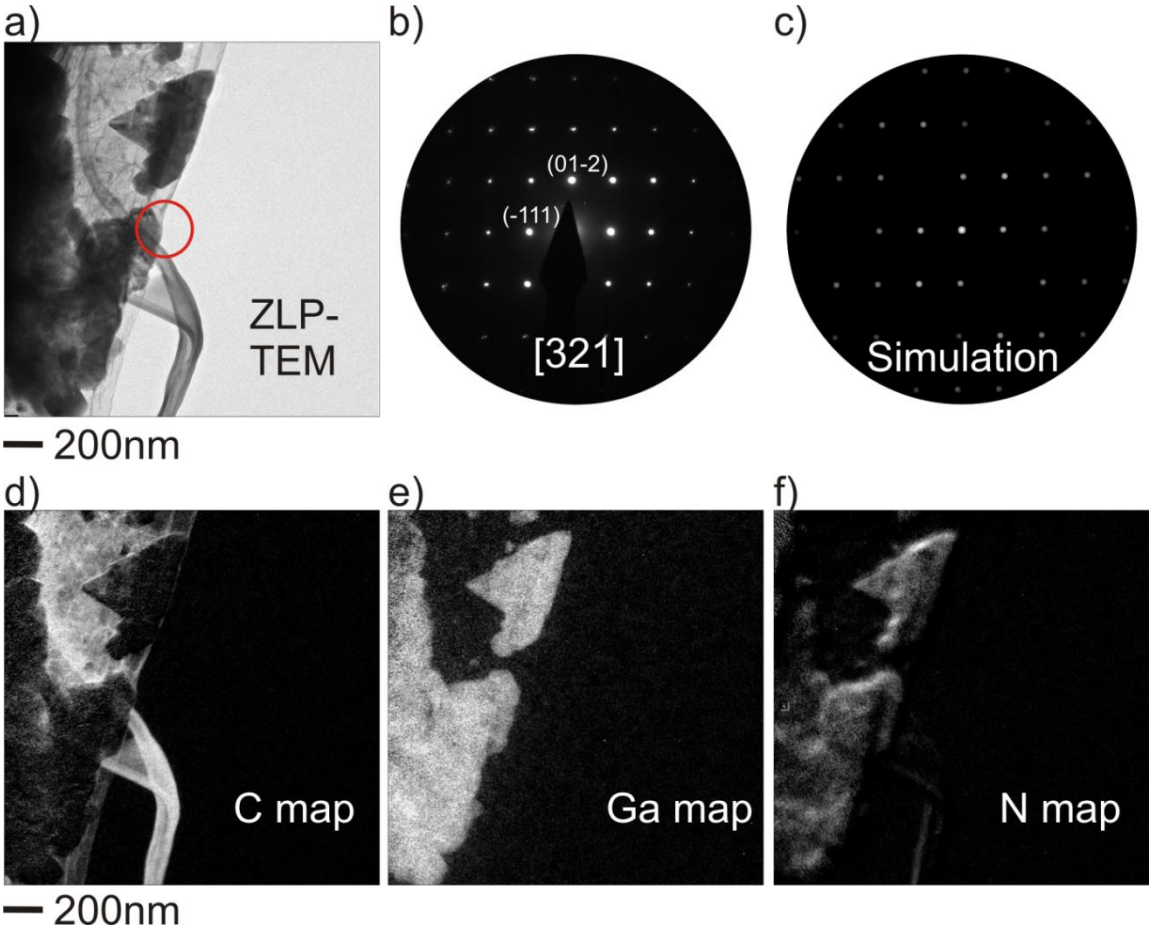

Figure 5.5 *(a) Zero loss peak TEM image of the AG/GaN composite. (b) SAED pattern along the zone axis [321] of GaN obtained from the red circled area in (a). (c) Computer simulated diffraction pattern along the same [321] axis. Additional Bragg intensities (e.g. (-12-1), (-333) (11-5)) are strongly excited by dynamical scattering effects due to thickness effect of the bulky crystallites. (d), (e) and (f) EFTEM elemental maps of carbon, gallium and nitrogen.*

5.4 Porous 3D Interconnected Nano-/Micro- Hollow Tubular Structure of Aero-GaN

In this section, the fabrication and analysis of porous 3D interconnected network structures consisting of only GaN (Aero-GaN) are discussed. The electronic property of this novel semiconductor network greatly depends on its structural quality. TEM is applied in order to investigate the morphology, chemical composition, crystallinity as well as the nature of the defects present in the Aero-GaN, and further uncover the growth mechanism of the 3D micro-network. Additionally, the evolution of microstructure and composition of Aero-GaN variants prepared under different synthesis parameter are revealed via TEM analysis.

5.4.1 As Prepared GaN Samples

One of the variants of Aero-GaN prepared at 850 ºC with the highest amount of remaining Zn component is shown in **Figure 5.6**(a). The side wall of the microtube is a continuous layer without any hole. Besides, it shows a high transparency to the electron beam, as another piece of the GaN film can be seen through this microtube. The bend contour indicates the entire microtube is a single crystalline thin film which is curved up into a hollow tubular structure.

A statistic EDX study in TEM mode from several different GaN microtubes of the sample grid shows an average amount of 7 at. % of Zn remaining on/in the microstructures. To further reveal the spatial distribution of the residual Zn, a spatially more confined EDX elemental mapping was performed (see **Figure 5.6**(b)). As can be inferred from the EDX map, Zn and O are present together with GaN, without any preferential aggregations on the microtube.

Structural analysis with SAED suggests the single crystallinity of the sample (see **Figure 5.6**(c)). However, when the projection of crystal lattice is along the [100] axis, ZnO and GaN can be hardly distinguished in TEM, e.g. the d-value of the ZnO (010) plane is only about 0.7 Å larger than that of GaN. Only for higher order Bragg reflections, a distinction between the two materials can be made, cf. splitting of the Bragg intensities in the experimental and simulated pattern of **Figure 5.6**(c) and (d). The enlarged view of the 4^{th} and 5^{th} order reflections on the bottom of **Figure 5.6** illustrates a d-value of the (010) plane (0.280 nm | ZnO literature value: 0.281 nm[144]) determined from the inner circle, and another one calculated from the outer circle with a smaller d-value of 0.277 nm (comparable to the GaN literature value: 0.274 nm[143]). The enlarged regions marked with green boxes confirm a reasonable match with the experimental data. It can be speculated that the residual ZnO might be serving as a stabilizing layer for the deposited GaN to grow with the similar lattice parameter and further achieve a highly crystalline epitaxial growth in a three dimension manner.

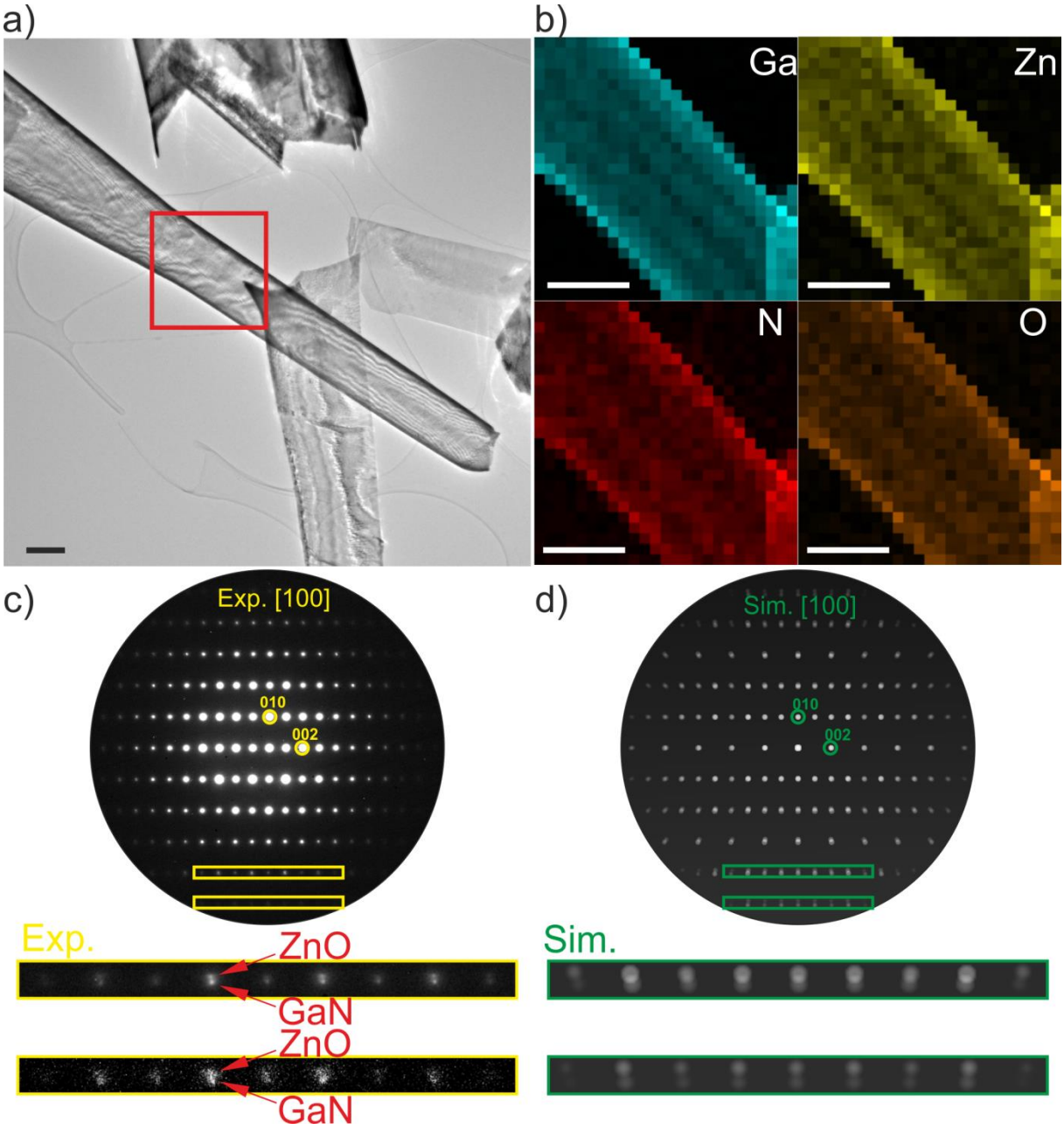

Figure 5.6 *Combined TEM chemical and structural analyses of Aero-GaN (850 ºC) hollow microtubes with an amount of residual Zn around 7 at. %. (a) TEM bright-field image of a GaN microtube. (b) EDX elemental maps from the region marked with a red square in (a). Blue: Gallium map; Red: Nitrogen map; Yellow: Zinc map; Orange: Oxygen map. (c) SAED pattern from the marked region in (a), showing a projection along the [100] zone axis of GaN or ZnO (space group: $P6_3mc$). (d) Computer simulated SAED pattern assuming an exact overlapping of the same [100] zone axis of both GaN and ZnO phases. In the bottom displays a comparison of two enlarged sections from the marked 4^{th} and 5^{th} order reflections in (c) and (d). Scale bar is 500 nm.*

Another variant of Aero-GaN is obtained at 950 ºC. The TEM bright-field image reveals an almost complete GaN tetrapod (see **Figure 5.7**(a)). Unlike the close-wall variant prepared at lower temperature, the microtubes consist of more porous walls. However, this porous tetrapod possesses a single crystalline structure, as proved by SAED on several positions. This finding implies that the porous variant can be a product from the lower temperature sample by further removing or etching away the materials from the originally closed walls.

Another difference as compared to the lower temperature sample is the absence of the splitting of Bragg intensities in the SAED pattern (**Figure 5.7**(a-*i*)). The results from the electron diffraction study may imply that the amount of the Zn phase could be reduced. Further EDX spectroscopy carried out on different particles of the sample verifies a remaining Zn content of only 3~4 at. %. EFTEM is proved to be more sensitive to light elements, i.e. oxygen from ZnO. With the low trace of Zn and thinner wall inside the sample, EFTEM elemental mapping can be an ideal approach to detect the location of Zn on the microtube. Two elemental maps are shown in **Figure 5.7**(b) and (c). The elements Ga and N are present together on the microtube. Moreover, a thin layer of Zn is clearly revealed in the inner wall area of the microtube (indicated with red arrows in **Figure 5.7**(b) and (c)). Furthermore, the light element oxygen maps in **Figure 5.7**(b-*i*) and (c-*i*) show a reasonable agreement with the zinc maps in **Figure 5.7**(b-*ii*) and (c-*ii*), which confirms the presence of residual ZnO.

This variant of the Aero-GaN indicates that with higher synthesis temperature the reduction of the ZnO template can be more intense and thus result in unclosed porous walls on the microtubes.

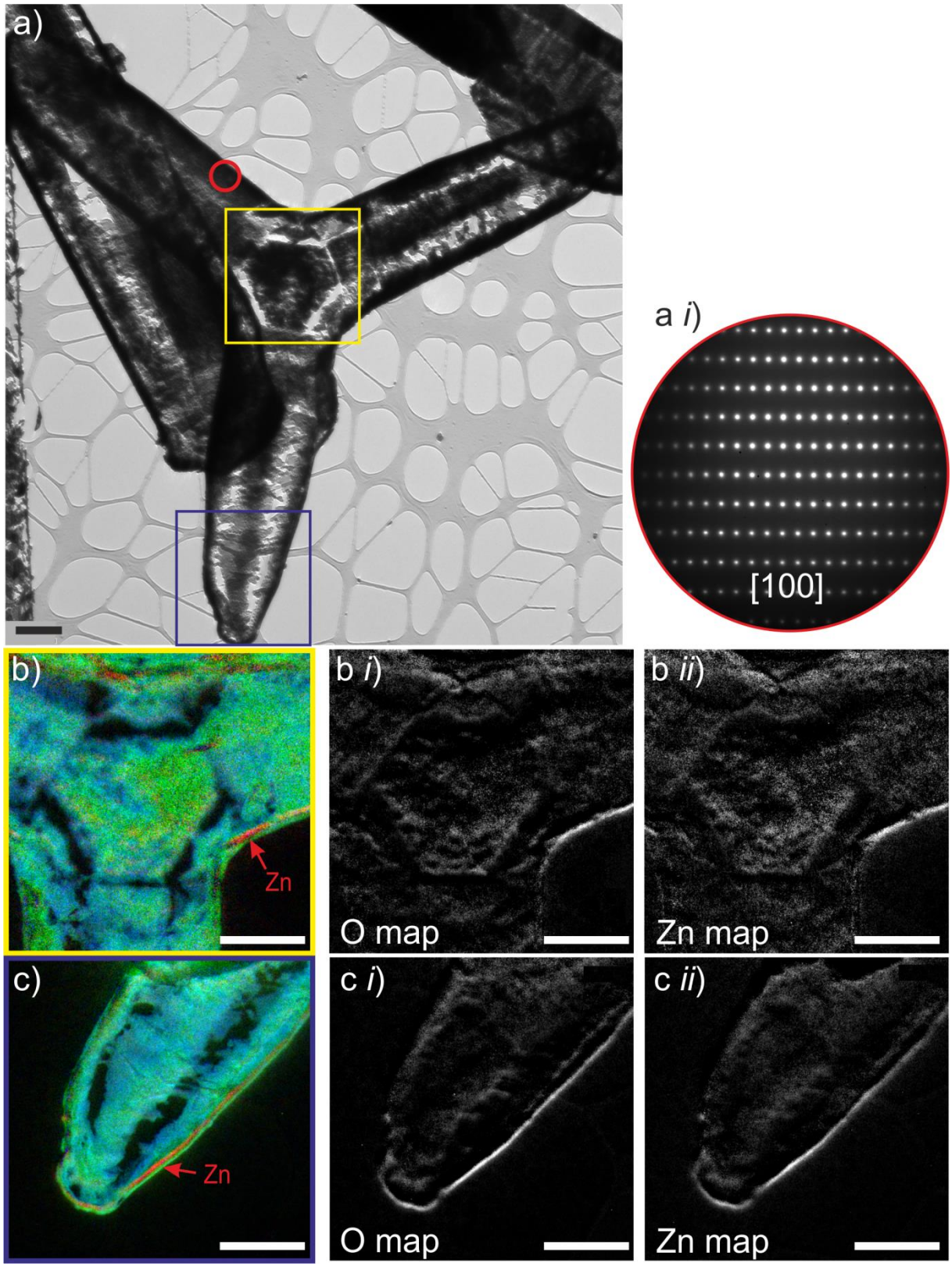

Figure 5.7 *TEM and EFTEM investigation of Aero-GaN hollow microtubes with an amount of residual Zn around 3~4 at. %. (a) TEM bright-field image of a porous GaN tetrapod. Inset (a i) shows the SAED pattern recorded from the red circled area on one of the legs of the tetrapod. (b) A combined EFTEM elemental map from the yellow box region in (a). The elements of interests are represented with different colors. Green: Gallium; Red: Zinc; Blue: Nitrogen. (c i) Oxygen map; (c ii) Zinc map. (c) A combined EFTEM elemental map from the blue box region in (a). (c i) Oxygen map; (c ii) Zinc map. Scale bar is 1 µm.*

5.4.2 After Intensive Hydrogen Treatment

In order to remove the residual Zn from the template, a post synthesis treatment using hydrogen gas was carried out to the as grown sample obtained at 850 °C (cf. **Figure 5.6**). The typical morphology is demonstrated in **Figure 5.8**(a) and (b). As compared to the TEM micrograph obtained before the hydrogen treatment, the post treated sample exhibits a much more porous structure with thinner walls, suggesting hydrogen removed most of the remaining Zn. The EDX measurement performed on several particles on the sample grid confirmed the overall remaining Zn is only about 0.7 at. %, which is an order of magnitude less than the same sample before the post synthesis treatment. Furthermore, the SAED investigation (**Figure 5.8**(c)) shows no more splitting of the Bragg intensities as compared to **Figure 5.6**(c), from which the d-value of the (010) is determined to be 0.277 nm, very close to the GaN literature value 0.274 nm[143]. Nevertheless, HRTEM imaging conducted on a thinner region in the highly crystalline particle (**Figure 5.8**(a)) revealed some stacking faults arranging perpendicular to the crystallographic c-axis (see **Figure 5.8**(d)). The stacking fault is intrinsic type I_1 basal-plane stacking fault, which is typical of wurzite structure.[145,146] The computer simulated micrograph assuming the wurzite structure of GaN is conducted and shown in the inserted image in **Figure 5.6**(d). The simulation exhibits a close match with the experimental HRTEM micrograph.

To conclude, the Aero-GaN is composed of hollow tubes of diameters of several µm with highly crystalline GaN layer as walls, i.e. it follows the morphology and microstructure of AG. Owing to different synthesis parameter and a post synthesis hydrogen treatment, the residual amount of Zn from the original ZnO sacrificial template shows a wide range of atomic percentages incorporated within GaN. Additionally, the as derived variants of Aero-GaN exhibit a variety of wall thicknesses and morphologies.

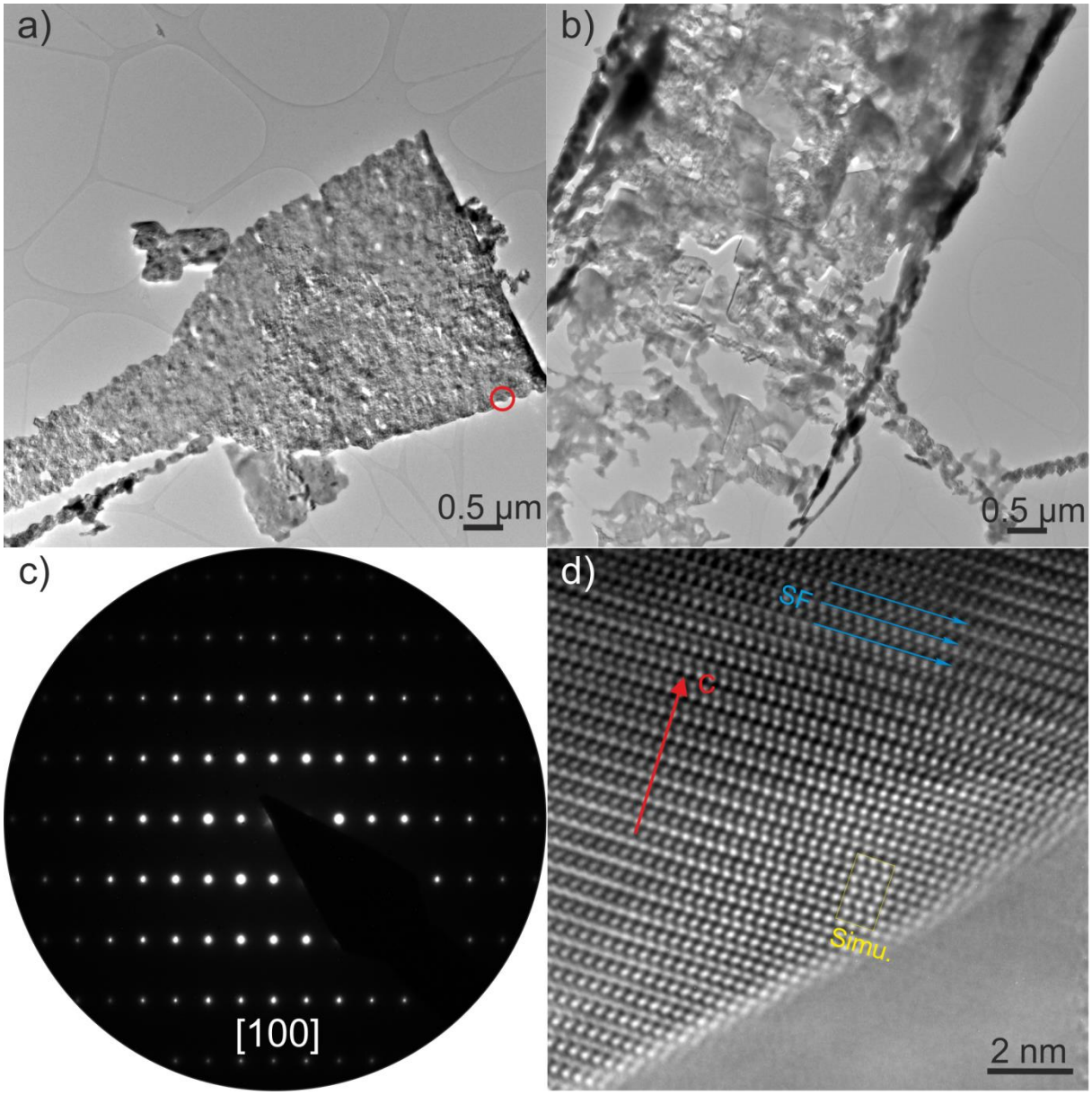

Figure 5.8 *(a) and (b) TEM micrographs from two particles of the Aero-GaN sample after post hydrogen treatment showing very porous morphology. (c) SAED pattern acquired from the red circle region in (a). The pattern is indexed to be along the [100] zone axis of GaN. (d) HRTEM micrograph recorded on the edge of a hole in the particle shown in (a). The red arrow indicates the c-axis of the crystallography direction. Some stacking faults are marked out with blue arrows. A multislice computer simulation image is inserted to be compared with the experimental data. The simulation is assuming a defocus of 70 nm, and a thickness of 4.74 nm of GaN structure.*

5.5 Summary: Aerographite and Aerographite-based Composites

The beam sensitivity of AG is investigated with 80 kV and 300 kV EELS. The quantitative EELS result shows an increased π^*/σ^* peak ratio of the carbon K-edge when lowering the acceleration voltage of TEM, which indicates the 300 kV electron beam modifies the graphitic carbon into the amorphous carbon. This finding signifies the necessity of applying low voltage TEM especially when investigating the graphitic feature within the carbon samples.

For the high temperature variant of the AG-like amorphous carbon, the bonding state is studied by examining both the high loss and the low loss regions of the carbon K-edge. However, a modification due to the 300 kV electron beam should be considered to interpret the results. Due to shorter acquisition time of the low loss spectra, the beam damage to the sample is limited. The low loss spectra reveal the sample contains mostly graphite-like carbon. Combining the information obtained from the high loss spectra, a mixture of graphite- and diamond-like carbon bonding is present in this high temperature AG variant.

For the detection of light elements like oxygen, nitrogen and carbon, the EFTEM elemental mapping technique in **Section 5.3** and **5.4** demonstrate advantageous sensitivities to reveal the spatial distribution of small traces on AG based composite samples down to micro-/nano-scale.

For the novel hollow tubular micor-/nano-structure of Aero-GaN, firstly, the SAED patterns and corresponding computer simulations on the variants of Aero-GaN suggest a possible intergrowth of GaN and ZnO phases. Secondly, in the extra hydrogen reduced Aero-GaN, HRTEM simulation proves the structure of GaN and near-atomic resolution imaging discloses defective structure, which might be a promising characteristic for further semiconductor applications.

6 *In Situ* TEM Observation of Heating and Irradiation on $CdSe/Cr_2Se_3$ 0-3 Nanocomposite

The soft chemical synthesis of multinary nanomaterials favors phase separation phenomena, which can be applied for producing nanocomposites.[147,148] Different morphologies were reported, e.g. the multilayer system of two alternating components (2-2 nanocomposites) or nanoparticles embedded in a matrix material (0-3 nanocomposites). [30,31,149] Moreover, a significant size effect is detected, owing to an enhanced surface to bulk ratio of the nanoparticles. Consequently, intense research interest is drawn to nanocomposites based on CdSe, because of the multidisciplinary applications, such as water splitting catalysts,[150] H_2 storage material,[150] optoelectronic and electroluminescent devices[151]. 0-3 nanocomposites with CdSe quantum dots embedded in a glass matrix are of high interests for electronic applications. [152,153]

The characterization of morphology, structure and chemical property of all components in a 0-3 nanocomposite is critical for the correlation of its structure and property.[27,28,29] TEM is an ideal approach to analyse the nanocomposite close to atomic resolution. However, the analysis is challenging due to electron irradiation damage to the sample. *In situ* TEM investigation enables analysis of these damage mechanisms in real time.[154] On the other hand, well-adjusted electron beam irradiation, e.g. electron beam lithography[155] and radiolytic methods[156,157], can be applied to design nanostructures[158,159,160]. In this chapter, a well-defined, porous and partially crystalline $CdSe/Cr_2Se_3$ composite[161], i.e. a 0-3 nanocomposite, is introduced and the structural and chemical modifications from *in situ* electron beam irradiation are discussed. Furthermore, conventional *in situ* annealing method is applied to study the thermal stability of the composite. The different mechanisms in the microstructural evolution of the 0-3 nanocomposite when applying two different experimental routines are compared and emphasized.

6.1 TEM Investigations

The synthesis of the $CdSe/Cr_2Se_3$ nanocomposite can be found in the work ref [100]. The sample exhibits microsized granular particles by TEM imaging (cf. **Figure 6.1**(a), performed by *Viola Duppel*). Note that the composite particles are not loose agglomerations of nanoparticles, as it is shown in **Figure 6.1**(a) that a particle is stably balancing on a carbon lacey fiber on the TEM sample grid. The composition of $CdCr_2Se_4$ is conserved, as the EDX analyses demonstrate an average ratio of Cd : Cr : Se = (14.9 : 28.8 : 56.3) at % with low variances of (0.3(Cd), 0.7(Cr), 0.2(Se)) at %. Further investigations via HRTEM imaging evidence the existence of a uniform distribution of nanoparticles within a 3D matrix, i.e. a 0-3 nanocomposite, instead of a ternary compound with one fixed chemical composition. Two phases are identified:

(1) CdSe nanocrystals, as the FFT pattern from the selected nanoparticle corresponds to the [1-1-1] zone axis of CdSe (space group: $P6_3mc$) (cf. **Figure 6.1**(b)). The SAED patterns

from larger areas show diffraction rings with d-values of CdSe (cf. **Figure 6.3**(c)) as well. Accordingly, the CdSe nanocrystals show no texture with preferential orientations. In addition, this observation agrees with XRD result.[100]

Furthermore, the second component in the 0-3 nanocomposite shows a chemical composition of Cr_2Se_3. However, it has two structurally different variants:

(2) a. Partially crystalline nanoslabs with a size of 10~20 nm (cf. **Figure 6.1**(b) and **Figure 6.1**(c)). As shown in the HRTEM micrograph (**Figure 6.1**(c)), an interlayer distance of ~0.58 nm of the consecutive nanoslabs is determined (cf. right panel of **Figure 6.1**(c)). This d-value can be assigned to that of the (003) plane of Cr_2Se_3 (space group *R*-3[162]).

(2) b. The second morphological variant is an amorphous matrix confirmed by chemical and electron diffraction analysis. It serves as glue for all other components. Only long-term exposure of the SAED patterns up to 15 s just captures faint and diffuse intensity with the characteristic d-spacings of Cr_2Se_3 (cf. **Figure 6.3**c). To conclude, the 0-3 nanocomposite consists of CdSe nanocrystals and Cr_2Se_3 slabs homogeneously embedded inside an amorphous Cr_2Se_3 matrix with a molar ratio of CdSe : Cr_2Se_3= 1:1. Nevertheless, it should be noted that the dispersal is so homogeneous that when performing EDX with the LaB_6 cathode this ratio is always observed.

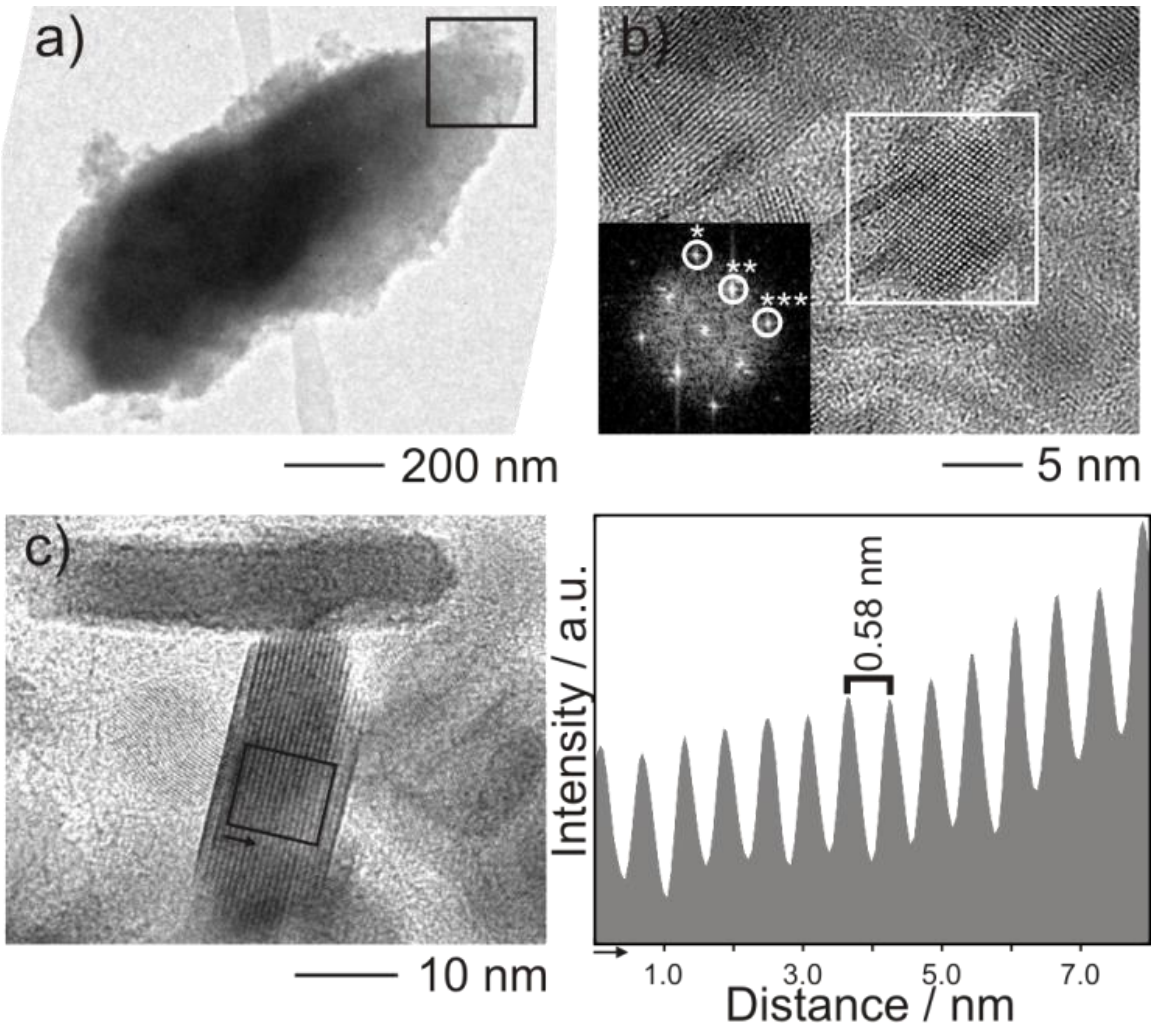

Figure 6.1 *(a) TEM bright field image of a 0-3 nanocomposite particle. (b) HRTEM micrograph of the area marked in (a). Inset: FFT pattern (zone axis [1-1-1] of CdSe nanocrystal with the starred reflection spots: * (110), ** (101), *** (1-12)). (c) Left: of partially crystalline Cr_2Se_3 nanoslabs. Right: line scan profile from the black square in the HRTEM micrograph. The layer distance ~0.58 nm (literature value: 0.576 nm[162]) is assigned to the d-valueg of the (003) plane of Cr_2Se_3. (Copyright © 2015 WILEY-VCH Verlag GmbH & Co. KGaA, Weinheim)*

6.2 *In Situ* Transformation of the 0-3 Nanocomposite Particles in TEM

To study the stability of the 0-3 nanocomposite against possible reactions of the components with increasing temperature, two modes of *in situ* heating were applied inside TEM:

6.2.1 Heating by Massive *In Situ* Electron Beam Irradiation

A higher dose of electron was attuned by increasing the emission parameters and removing the condenser aperture, which was conducted by *Viola Duppel*. The current density in the "transformation mode" is estimated to be 40-fold higher than the normal observation mode.[163] After several minutes of intense irradiation, the shape of the particles remained, (cf. **Figure**

6.2), and no ternary $CdCr_2Se_4$ crystals are found. However, a complete elimination of the CdSe nanocrystals is detected by EDX analyses. Accordingly, the composition of the area studied changes from Cd: Cr : Se = (15.5 : 28.0 : 56.6) at % to Cr : Se = (41.5 : 58.5) at % after irradiation.

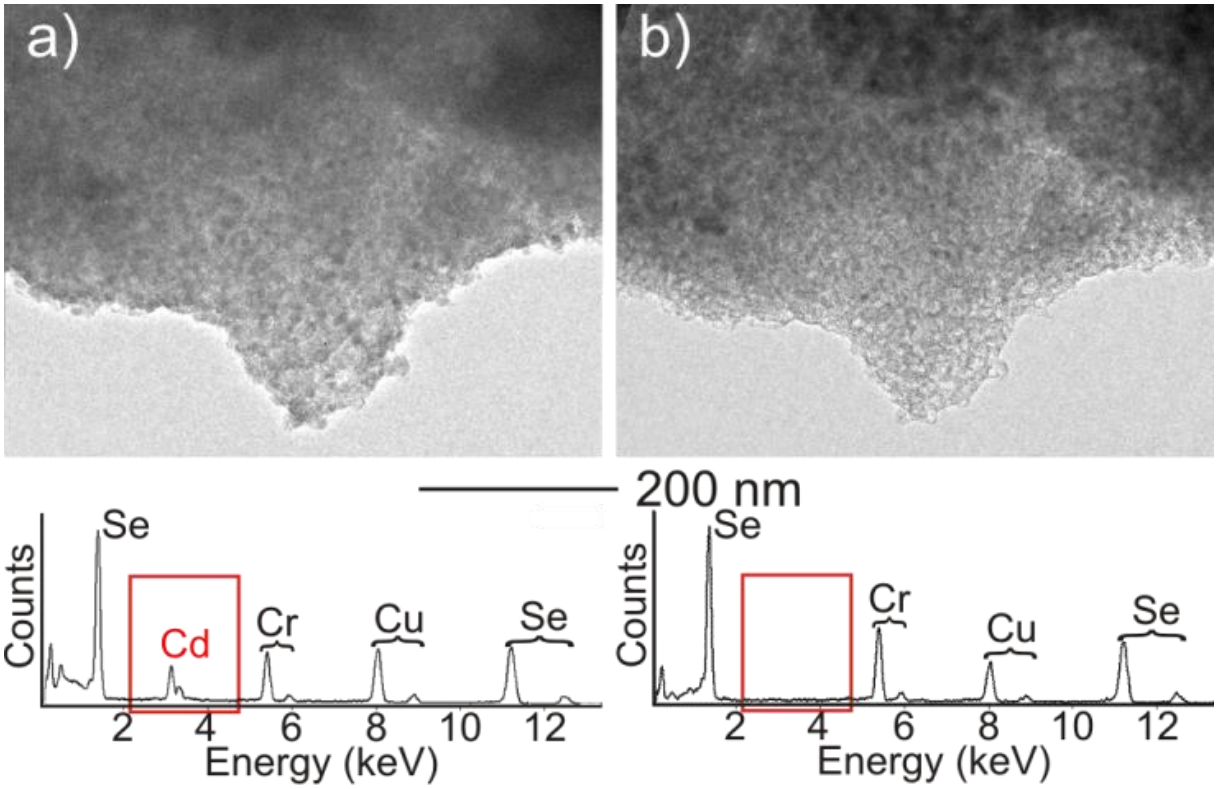

Figure 6.2 *TEM **b**right field images and the corresponding EDX spectra from a 0-3 nanocomposite particle: (a) before and (b) after in situ irradiation. Regardless of the complete removal of the CdSe nanocrystals, the composite particle maintains its original shape during the in situ transformation. (Copyright © 2015 WILEY-VCH Verlag GmbH & Co. KGaA, Weinheim)*

A comparison of HRTEM micrographs before and after electron beam irradiation is shown in **Figure 6.3**. The CdSe nanocrystals (starred in **Figure 6.3**(a)) are clearly shown to be removed, leaving holes at the same positions (starred in **Figure 6.3**(b)). The matrix of Cr_2Se_3 remains mostly unaffected after irradiation. It is confirmed by SAED analysis (cf. **Figure 6.3**(c) and (d)), where both patterns exhibit diffuse intensities corresponding to poorly crystalline Cr_2Se_3. Further study of the radial intensity distribution of SAED patterns is carried out to quantify the change of the crystallinity of the Cr_2Se_3 phase before and after irradiation. From the rotational average profiles in **Figure 6.3**(e) and (f), the elimination of the reflections from CdSe is evident. Additionally, the intensity of the 113, 116 and 030 reflections from Cr_2Se_3 increased, and the intensity ratio of the three reflections evolved into a similar one to the simulated diffraction pattern (cf. **Figure 6.3**(f) and **Figure 6.4**) based on bulk Cr_2Se_3. Before irradiation, the intensity ratio is $I_{113} : I_{030} : I_{116} = 1 : 1.1 : 1.6$, while after irradiation, $I_{113} : I_{030} : I_{116} = 1 : 0.46 : 0.43$. In the theoretical case, the ratio is $I_{113} : I_{030} : I_{116} = 1 : 0.30 : 0.50$.[162] Moreover, the characteristic 113 reflection developed into a more defined shape after irradiation. All the findings suggest a higher crystallinity of the Cr_2Se_3 matrix

which approximates the bulk material of randomly dispersed Cr_2Se_3 crystals after *in situ* irradiation.

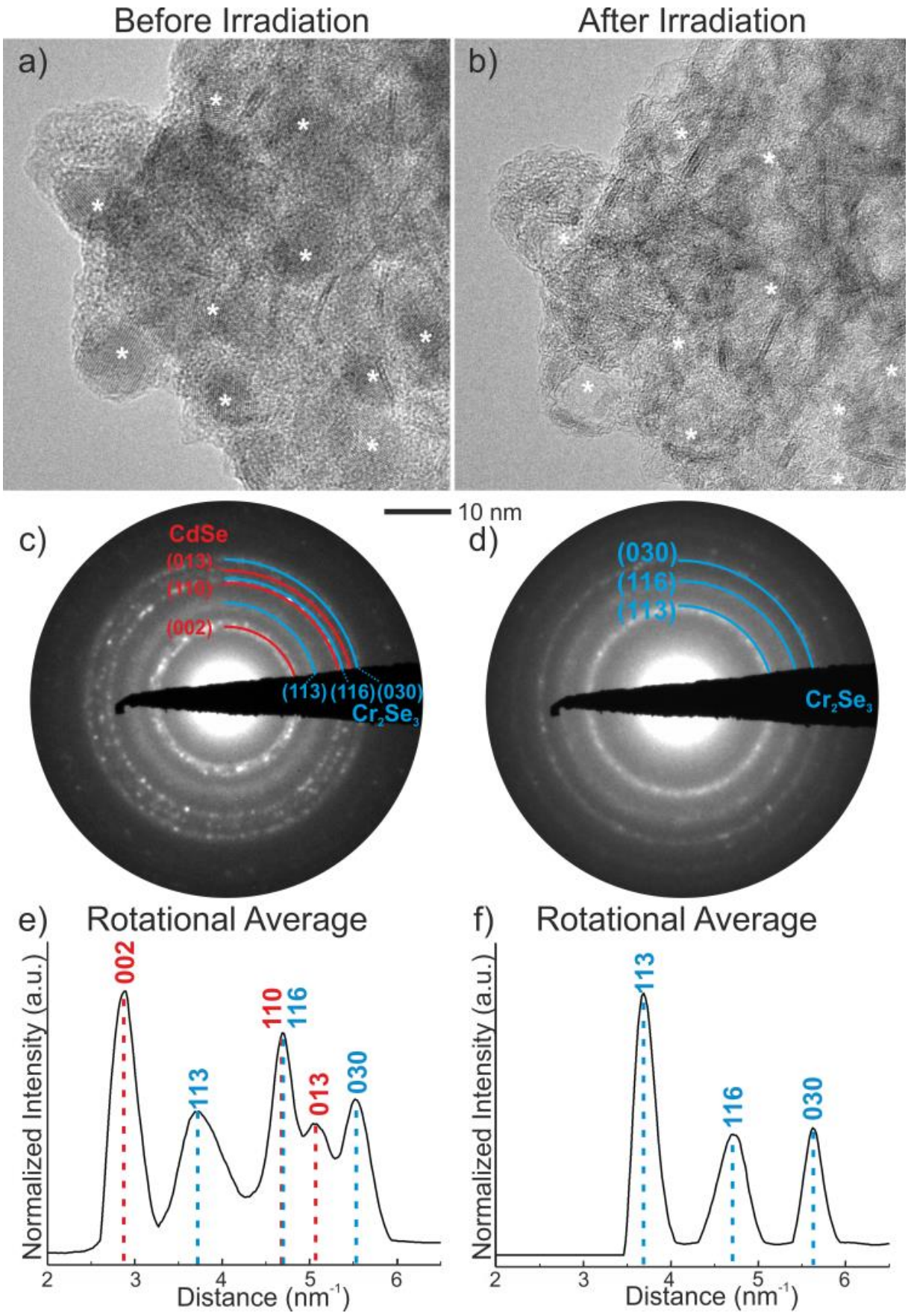

Figure 6.3 *Comparison of the microstructures of the 0-3 nanocomposite: (a) before and (b) after in situ irradiation. The starred positions of the CdSe nanoparticles present before in situ irradiation. (c) and (d): long-term exposed SAED patterns acquired (c) before and (d) after in situ irradiation. (e) and (f): Corresponding rotational average profiles extracted from SAED patterns above. The intensity peaks are identified by the indices given in red (CdSe) and blue (Cr_2Se_3), respectively. (Copyright © 2015 WILEY-VCH Verlag GmbH & Co. KGaA, Weinheim)*

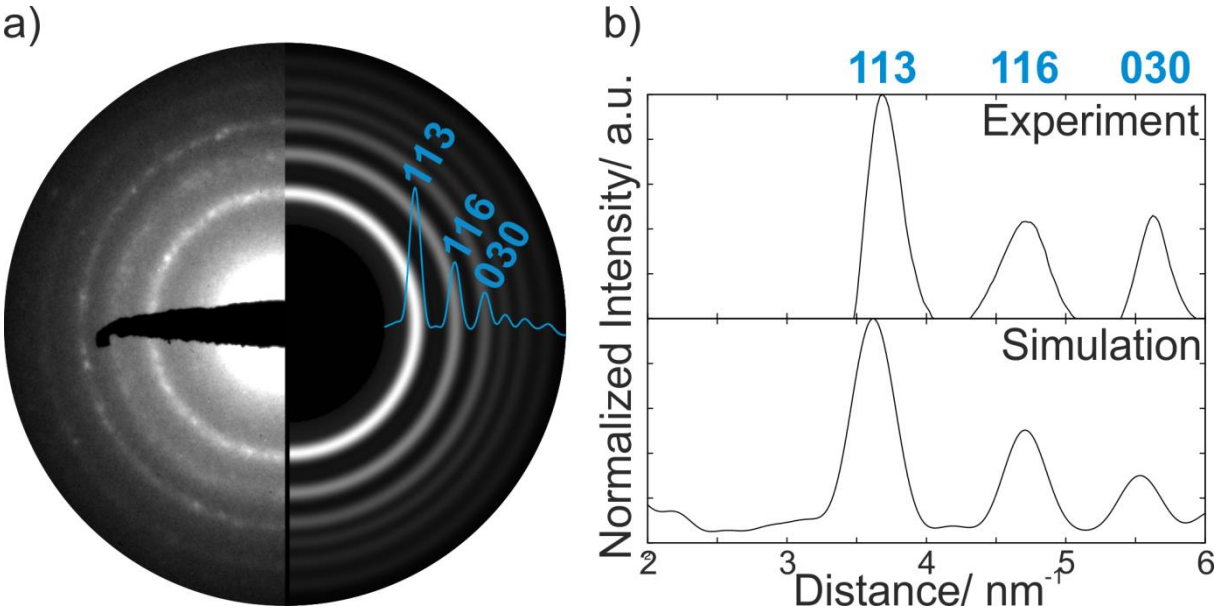

Figure 6.4 *A comparison of experimental SAED pattern and rotational average profile of Cr_2Se_3 after in situ irradiation with the corresponding simulation. The d-values from the reference[162] and experimental data (**113**: 2.752 Å|2.71 Å; **116**: 2.125 Å|2.12 Å; **030**: 1.805 Å|1.78 Å) exhibit a marginal deviation of less than 1.5 %. Simulation performed in collaboration with Dr. Viktor Hrkac. (Copyright © 2015 WILEY-VCH Verlag GmbH & Co. KGaA, Weinheim)*

6.2.2 *In Situ* Heating by a TEM Heating Stage

By using a heating stage and a low dose of electron irradiation, *in situ* heating experiment applies a heating ramp up to 800 °C to the 0-3 nanocomposite particles. A series of SAED patterns recorded every 50 °C is manifested in **Figure 6.5**(a). Two characteristic reflections can be associated to the (116) and (030) planes of Cr_2Se_3 the SAED pattern recorded at 50 °C. Because of thermal drift during the heating experiment, a short exposure time was used for recording SAED patterns, which leads to quasi extinction of the faint (113) reflection. At 800 °C, additional strong Bragg reflections were observed in the SAED pattern (cf. **Figure 6.5**(a)). The d-spacings of the Bragg reflections coincide with Cr_2Se_3. This observation suggests an improved crystallinity of the host matrix and an enhanced size of the Cr_2Se_3 nanoparticles compared to *in situ* irradiation experiment. After cooling down to room temperature, HRTEM micrograph (**Figure 6.5**(b)) confirms the findings as lattice fringes in the Cr_2Se_3 particles are shown and the corresponding FFT pattern reveals the most characteristic (113) peak of Cr_2Se_3. The characteristic (002) reflection of the second component CdSe (red arc marked in **Figure 6.5**(a)) disappeared after 550 °C. The removal of

CdSe is further confirmed by EDX investigations performed after heating, which is similar to the result of *in situ* irradiation with the high dose of electrons.

Nevertheless, unlike the phase diagram of bulk Cr_2Se_3[164] and the *in situ* irradiation experiment, a formation of Cr-enriched and Se-free nanoparticles was observed during the *in situ* heating experiment. The 800 °C SAED pattern (see **Figure 6.5**) displays two diffuse rings, which can be indexed to the (011) and (112) planes of chromium (space group: *Im*-3*m*). Further nanoprobe elemental mapping and HRTEM analysis (**Figure 6.6**(*a*) and (b)) support this finding. The Cr-enriched particles show brighter intensity in the HAADF-STEM image owing to the higher thickness compared to the porous Cr_2Se_3 matrix. Moreover, post-heating structural studies at room temperature (performed by Dr. *Viktor Hrkac*) detected the presence of Cr-enriched crystalline nanoparticles with a size of several tens nanometer with non-cubic structure, cf. **Figure 6.6**(*c*). These particles with a remarkably high density of twin defects cannot be identified to any known phase, e.g. Cr allotropes or the binary phases such as Cr-C, Cr-Se, or Cr-O. One speculation can be the *in situ* heating process might lead to a production of a yet unknown Cr allotrope.

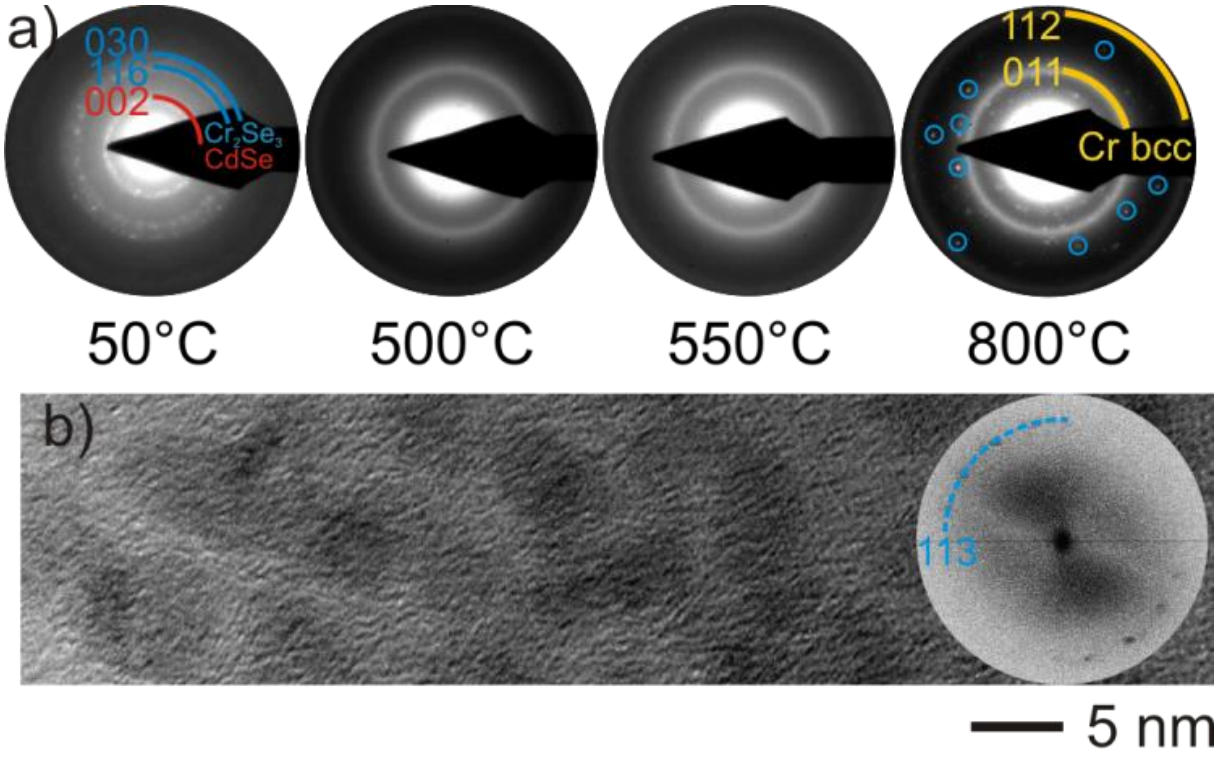

Figure 6.5 *(a) SAED patterns recorded during in situ heating experiment. 50 °C: Identification of Cr_2Se_3 and CdSe. 500 °C: Diminishing intensity for the characteristic (002) reflections of CdSe. 550 °C: Entire disappearance of the (002) reflections of CdSe. 800 °C: Formation of Cr bcc phase (yellow arcs) and presence of Bragg reflections assigned to Cr_2Se_3 (blue circles). (b) HRTEM micrograph of Cr_2Se_3 nanoparticles after in situ heating. Inset demonstrates the corresponding FFT pattern, which shows the characteristic (113) intensity ring from Cr_2Se_3. (Copyright of Zeitschrift für anorganische und allgemeine Chemie)*

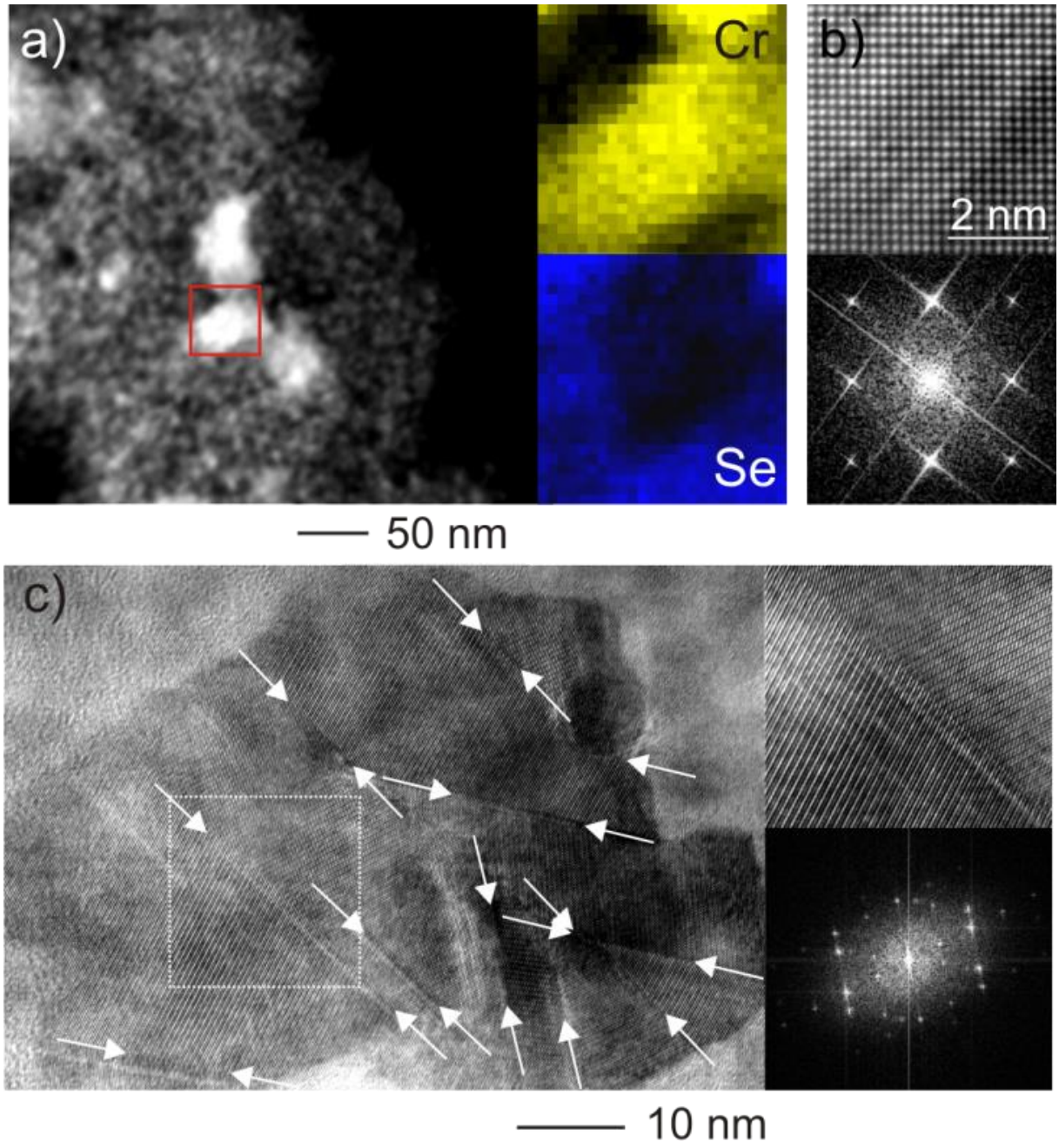

Figure 6.6 *(a) HAADF-STEM investigations: indication of Cr-rich particles inferred by Z-contrast (left) and EDX elemental maps (right). (b) HRTEM micrograph (top) and corresponding FFT pattern (bottom) of crystalline Cr (space group: Im-3m) show the [100] zone axis projection. (c) left panel: HRTEM micrograph of a Cr-enriched particle with several twin defects (marked by white arrows). Note: the multiply twinned particles cannot be assigned to bcc-Cr. right panels: Magnified view and corresponding FFT pattern from the square marked area in the left panel. (Copyright © 2015 WILEY-VCH Verlag GmbH & Co. KGaA, Weinheim)*

6.2.3 *In Situ* Heating Experiment of Bulk Cr_2Se_3

The Cr-formation via *in situ* heating experiment on the $CdSe/Cr_2Se_3$ 0-3 nanocomposite particles cannot be explained by the Cr-Se binary phase diagram for bulk material. *In situ* heating experiments were carried out on crystalline bulk Cr_2Se_3 as a reference to further

verify these findings. The typical morphology of a bulk Cr_2Se_3 crystallite is illustrated in **Figure 6.7**(a) and the HRTEM micrograph from the boxed region confirms its high crystallinity (**Figure 6.7**(b)). Moreover, SAED patterns along the [210] zone axis of Cr_2Se_3 were obtained inside the same area before and after *in situ* heating, cf. **Figure 6.7**(c), where the only differences are arcs of diffuse intensity occurred after heating to 800 °C (**Figure 6.7**(c ii)). The d-spacings still correlate with those of bulk Cr_2Se_3, implying splitting of the crystals and creation of rotationally disarranged grains (mosaic structure) after heating. The almost identical diffraction patterns show that the Cr_2Se_3 bulk crystals are stable under the *in situ* heating experiment. Additionally, an elemental analysis (not shown) from the same region of the crystallite revealed that the chemical composition remains unaffected by heating. Contrary to the *in situ* heating experiments on the 0-3 nanocomposite, no Cr-enriched particles were found.

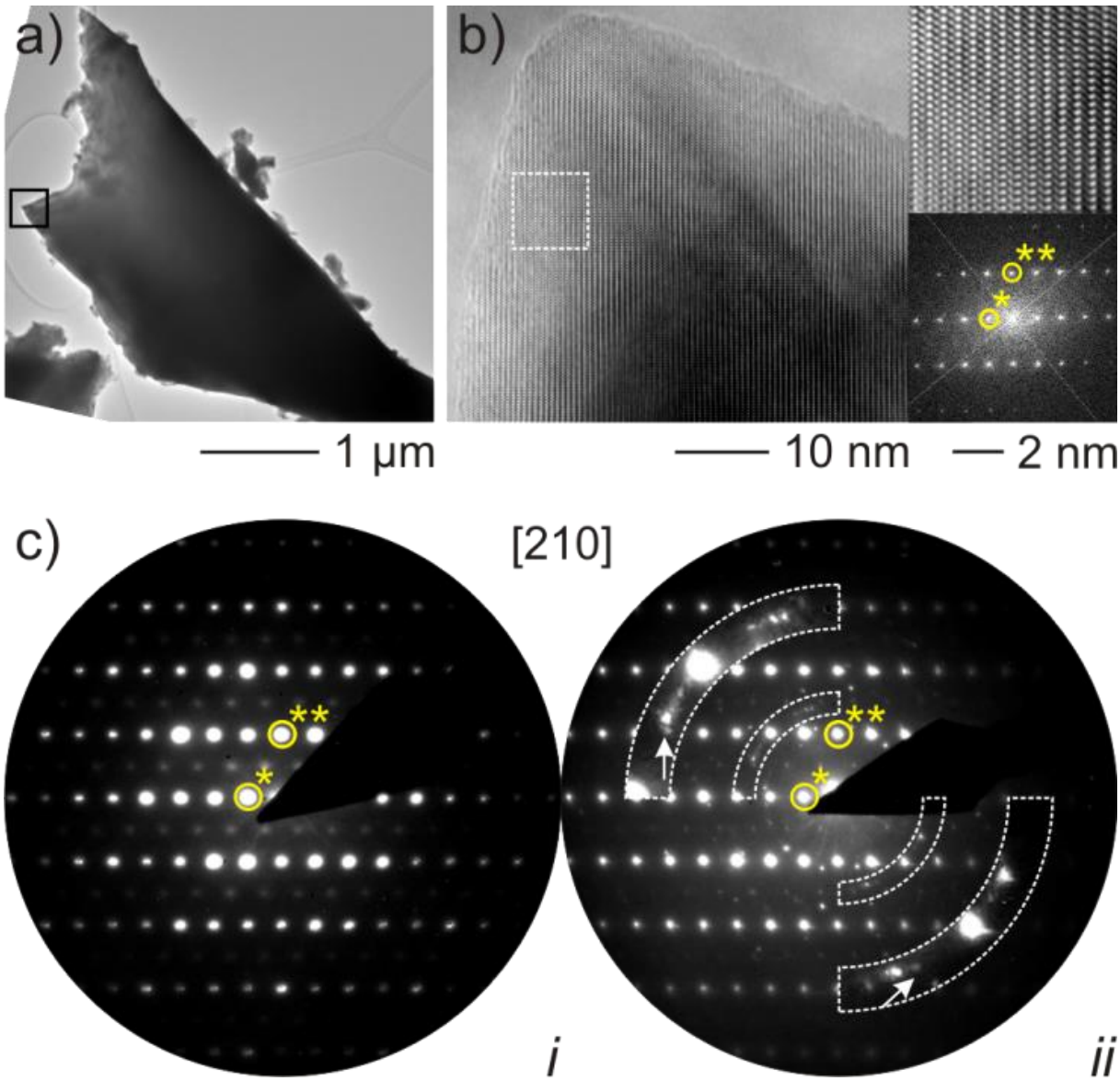

Figure 6.7 *In situ heating experiment on crystalline Cr_2Se_3 bulk samples: (a) TEM bright field image. (b): left panel, HRTEM micrograph of the black square marked area in (a). (b): right panels, Magnified view from the white square marked region and the corresponding FFT pattern (zone axis [210] of Cr_2Se_3). (c) SAED patterns from the same region marked in (a) before (c i) and after(c ii)*

*in situ heating. The insets in (c ii) are magnified sections of the marked region of the SAED pattern showing the presence of diffuse diffraction rings. The asterisks denote the reflections * (003) and ** (-120), respectively. (Copyright © 2015 WILEY-VCH Verlag GmbH & Co. KGaA, Weinheim)*

6.3 Discussion

In this section, the results of the *in situ* observations from 0-3 nanocomposites under different conditions are discussed and related to corresponding reference experiments.

i. During the *in situ* electron beam irradiation experiment of the 0-3 nanocomposite, the selective evaporation of CdSe was observed. As known from literature, there are drastic thermal conductivity (κ_L) differences between the CdSe and Cr_2Se_3 (κ_L(CdSe nanoparticles) = 0.090 W cm^{-1} K^{-1}; [165] $\kappa_L(Cr_2Se_3)$ = 0.019 W cm^{-1} K^{-1} @200 °C, 0.022 W cm^{-1} K^{-1} @600 °C, [166] which should be lower for amorphous Cr_2Se_3). Heat transfer study on nanocomposites reveals that thermally well conducting particles in a thermally isolating surrounding can suffer significant beam heating, e.g. CdSe nanoparticles in Cr_2Se_3 matrix in the 0-3 composite, due to a pronounced interface thermal resistance causing heat entrapment at the interface.[167] The increase of temperature at the interface can be an order of magnitude higher than that inside the matrix.[167] Specifically, the heat entrapment arises when a heat gradient is abruptly generated, e.g. by electron beam irradiation, on the composite surface. However, compared to the *in situ* heating experiment, the gradual and slower heating process cannot cause prominent heat entrapment thanks to the heat redistribution with the aid of the carbon film of the TEM grid. Consequently, a thermal equilibrium can be achieved. Moreover, knock-on damage can enable the removal of the CdSe particles, generating well-defined micro-pores in the matrix.

ii. During the *in situ* heating experiment, the thermal evaporation temperature (~550 °C) of CdSe in TEM is lower than that of the conventional thermal physical vapor deposition to obtain a vapor phase of CdSe (~725 °C (8×10^{-6} Torr)).[168] This observation can be clarified by the size effect of the CdSe nanoparticles, i.e. the limited sizes of the nanoparticle leading to a smaller diffusion path length. Moreover, the pressure in TEM column is lower (1×10^{-7} Torr) and the low thermal conductivity of the Cr_2Se_3 matrix can increase the temperature locally at the CdSe nanoparticles.

iii. During *in situ* heating, no well-defined holes are observed after the evaporation of CdSe. This finding can be interpreted that the electron irradiation is a highly localized process, while the *in situ* heating applies to the whole TEM grid. Therefore, the Cr_2Se_3 matrix undergoes a more uniform annealing during *in situ* heating. Consequently, there is more time for the Cr- and Se-atoms to be transported to the pores left from the evaporation of CdSe and to reorganize into a continuous and thermodynamically more stable matrix.

iv. It is worth comparing the results with those from a heating procedure on Cr/Se multilayers[169]. In the study of Cr/Se multilayers, the initial composition exerts only a minor impact on the reaction pathways and final products. Structural change during heating of the multilayers includes: (1) An amorphous Cr-Se film is formed by interdiffusion of the multilayers. (2) As the thermal treatment continues, the formation of crystalline Cr_3Se_4 is detected (instead of Cr_2Se_3 in the case of 0-3 nanocomposite). In all cases studied (e.g. Cr-rich or Se-rich Cr/Se multilayers), an evaporation of Se was observed. Such situation might be valid for the 0-3 nanocomposite particles. The partial evaporation of Se can result in an excess of Cr in the 0-3 nanocomposite, and finally in the formation of Cr-enriched crystallites after *in situ* heating. Accordingly, no $CdCr_2Se_4$ can be produced when heating up the 0-3 nanocomposite. This finding agrees with reports[170] highlighting the necessity of excess Se for synthesis of $CdCr_2Se_4$. The crystallization of Cr_2Se_3 for the 0-3 nanocomposite particles during heating might be originate from the partially crystalline Cr_2Se_3 nanoslabs which act as nucleation seeds for the amorphous Cr-Se matrix.

6.4 Summery

The *in situ* TEM experiments deliver real time understandings of the impacts of external stimuli onto the nanocomposite. The findings indicate that matrix materials with low thermal conductivities might be undesired candidates for nanocomposites embedded with CdSe nanoparticles, since the thermal stability of the CdSe particles in such matrix is compromised owing to the possible heat entrapment at the interface. The potential mechanisms of beam damage and heat transfer within the 0-3 nanocomposite clarify the reliability of CdSe nanocomposite when under abrupt increase of temperature (heating via beam irradiation) or under gradual thermal heating. Furthermore, more work such as quantification of the actual temperature increase in 0-3 composite and *in situ* experiments on nanocomposites with different matrix materials would give more insight into this topic. Moreover, the production of a yet unknown allotrope of Cr implies that new phases / structures can be produced under extreme *in situ* TEM conditions, enabling fundamental insights into material chemistry.

Conclusion and Outlook

TEM is demonstrated in this work as a powerful tool for retrieving nanoscale information regarding the size, morphology, chemical composition, crystal microstructure, and the dynamics in the physical and chemical processes. The sampled particles feature different length scales and geometries. Furthermore, by discussing the practical properties of the functional nanoparticles and particle systems, the essential relations associated with the microstructure and macroscopic performance are clarified.

Different MoS_2 nanoparticle composites are synthesized and the microstructures of MoS_2 and of the interface are studied. The bonding states of the incorporated carbon inside the composites are revealed by EELS. The microstructural characteristics are further related to the catalytic property.

Quasi 1D nanorods for sensor application are characterized. TEM structural and compositional investigations disclose the defective surface sites of the MoO_3 nanorod, which are believed to be the microstructural origin of its sensor response. Furthermore, a comprehensive method of EFTEM, SAED, HRTEM and *in situ* heating is applied to unravel the complex microstructure of the $SnO_2/Ga_2O_3/GaN{:}O_x$ composite. It defines a fundamental starting point to realize the composite based nanosensors.

AG based 3D microstructured networks are presented. EELS and EFTEM are demonstrated as effective tools to probe the structural and chemical properties of the AG materials. In addition, a possible intergrowth within the Aero-GaN samples is proven by dedicated TEM structure simulation. The findings are essential for controlling the quality and optimizing the performance of the samples.

An extensive *in situ* TEM study of the CdSe / Cr_2Se_3 0-3 nanocomposite is accomplished, which is compared with conventional *ex situ* methods. The findings suggest different mechanisms occurring in *in situ* heating and irradiation. The observations made under extreme *in situ* TEM conditions facilitate fundamental perception of material chemistry.

Further possibilities and challenges for refining TEM characterization in the realm of nanosized and amorphous materials are present in this thesis. With regard to the characterization of the MoS_2 nanosized catalyst, IFFT calculation from HRTEM micrograph proves to be a pragmatic approach to visualize the desired microstructure with highly specified d-spacings, e.g. the characteristic 002 lattice planes of MoS_2 in an amorphous matrix. EELS log-ratio method for thickness measurement manifested on the exfoliated MoS_2 nanoflakes is a promising technique to complement other analytic tools for precise monitoring and controlling size distribution of nanoparticles. These two methods, i.e. IFFT and EELS thickness measurement, can be established as standard routines for TEM analysis of

nanocomposites integrated with layered structure compounds including MoS_2, WS_2, graphite/graphene, and carbon nanotubes. Yet more quantitative experimental setups for the determination of convergence angle and collection angle of the microscope are needed. STEM tomography is another promising method for offering 3D insights into heterogeneous catalyst systems[171,172].

Furthermore, EELS has already proved to be an indispensable method to distinguish between graphitic (sp^2 bonded), carbide-like and diamond-like (sp^3 bonded) carbon species. A systematic approach for determination of the sp^2 and sp^3 bonding via EELS is established in this work. The carbon species in the novel $MoS_xC_yP_z$, MoS_xC_y composites, AG, and AG variants are evidenced for the first time. Nevertheless, the determination of the bonding states is realized here by qualitative comparison with reference materials. Complimentary information obtained by other analyses, e.g. XPS, Raman spectroscopy and EXAFS, is needed to substantiate the EELS results. A further challenge is about the quantitative EELS approach. It includes estimating and modelling the coordination environment of the carbon atoms, especially the carbide-like carbon species, within the complex nanocomposites. The structure model will be verified by comparing computer simulation with experimental EEL spectra. In this manner, EELS simulation will serve as a basic guideline to understand the microstructure of the carbon containing composites.

Regarding to promoted nanocatalysts and core-shell nanocomposites, interface is one of the pivotal aspects for understanding their synergetic effect. HRTEM imaging of the interface between the MoS_2 catalysts and promoter, and between the core and shell in $SnO_2/Ga_2O_3/GaN{:}O_x$ composite are presented in this thesis. The result can be considered as a starting point for investigating such interfacial structures. Further work like structural modelling and computer simulation of the interface between MoS_2 and promoter are needed. It can provide atomic insight into the synergetic effect, i.e. the promoter effect, of the promoted catalyst. In the case of amorphous phases, another possible approach for extracting more information from the interface is the bonding state characterization via STEM-EELS. By a nanoprobe line scan through the interface region, a series of EEL spectra can be collected. Subsequently, the difference of the bonding state in the individual bulk and interface can be revealed. This will open plenty research opportunities for fundamental understandings of interfaces in nanoparticle systems.

The *in situ* TEM experiments deliver real time insights into the impacts of external stimuli onto the nanocomposites presented in this thesis, e.g. the $MoS_xC_yP_z$ composite, the amorphous MoS_2 (PX) sample, the $SnO_2/Ga_2O_3/GaN{:}O_x$ composite and the $CdSe/Cr_2Se_3$ 0-3 nanocomposite. The findings shed light on the dynamic stability of the nanocomposite. Moreover, a controlled crystallization of the PX sample is presented for the first time. Even single slabs of MoS_2 can be produced *in situ* as 2D single sheet material for nanoelectronic applications. On the other hand, more accurate quantification of the actual temperature increase and electron doses is required. A future project that is motived by this topic is to evaluate the mechanical properties of the single sheet material with *in situ* tensile experiments inside TEM.

With the aid of electron diffraction and computer simulation, the statistically representative and quantitative TEM analyses of the rotational average profiles of the PXCo sample gives a good agreement with the XRD results and with the size and microstructure distribution histograms. Especially the kinematic and dynamic simulation of the SAED pattern reveals the evolution of crystallinity and microstructure of the MoS_2 phase under HDS condition. This combined approach of imaging, diffraction and simulation can present as a prototypical methodology for statistical TEM analysis of nanoparticle assemblies. Another advanced TEM method, i.e. Automated Crystalline Orientation Mapping (ACOM), can be employed to reveal the microstructure and crystal phase of the nanoparticles in a larger scale.[173,174,175,176] This technique will enable the fast acquisition and analysis of statistic TEM data.

However, when the size of the nanoparticles decreases to the amorphous region, i.e. angstrom region, conventional TEM techniques mentioned above may not be applicable. Consequently, RDF retrieved either from energy filtered SAED pattern or from EXELFS can be used to investigate the structure ordering of the amorphous materials.[41] In this way, TEM can represent the crucial solution to characterize large varieties of particles and particle systems, starting from micrometer, nanometer to angstrom regions.

Bibliography

[1] J. Thomas, P. A. Midgley, High-resolution Transmission Electron Microscopy: the Ultimate Nanoanalytical Technique, Chem. Commun., 2004, pp 1253-1267.
[2] F. L. Plantenga, R. G. Leliveld, Sulfur in fuels: more stringent sulfur specifications for fuels are driving innovation, Appl. Catal. A: Gen., 248, 2003, pp 1–7.
[3] X. Chen, S. Shen, L. Guo, S. S. Mao, Semiconductor-based Photocatalytic Hydrogen Generation, Chemical Reviews, 110, 11, 2010, pp 6503-6570.
[4] V. H. Grassian, When Size Really Matters: Size-Dependent Properties and Surface Chemistry of Metal and Metal Oxide Nanoparticles in Gas and Liquid Phase Environments, J. Phys. Chem. C, 2008, 112, pp 18303–18313.
[5] K. Tiedeae, A. Boxallae, S. P. Tearb, J. Lewisa, H. Davidc, M.Hassello, Detection and Characterization of Engineered Nanoparticles in Food and the Environment, Food Additives and Contaminants 2008, 25, pp 795–821.
[6] M. Ramos, G. Berhault, D. Ferrer, Brenda Torres and Russell R. Chianelli, HRTEM and Molecular Modeling of the MoS_2–Co_9S_8 Interface: Understanding the Promotion Effect in Bulk HDS Catalysts, Catalysis Science & Technology, 2012, 2, pp 164.
[7] B. Abram, J. Wilcoxon, Nanosize semiconductors for phtooxidation, Critical Reviews in Solid State and Material Science, 30, 2005, pp 153-183.
[8] Z. Wu, B. Fang, Z. Wang, C. Wang, Z. Liu, F. Liu, W. Wang, A. Alfantazi, D. Wang, D. P. Wilkinson, MoS_2 Nanosheets: A Designed Structure with High Active Site Density for the Hydrogen Evolution Reaction, ACS Catal., 2013, 3, pp 2101–2107.
[9] J. Djamil, S. A. Segler, A. Dabrowski, W. Bensch, A. Lotnyk, U. Schurmann, L. Kienle, S. Hansen, T. Beweries, The Influence of Carbon Content on the Structure and Properties of MoS_xC_y Photocatalysts for Light-Driven Hydrogen Generation, Dalton Trans., 2013, 42, pp 1287–1292.
[10] A. B. Laursen, P. C. K. Vesborg, I. Chorkendorff, A High-Porosity Carbon Molybdenum Sulphide Composite with Enhanced Electrochemical Hydrogen Evolution and Stability, Chem. Commun., 2013, 49, pp 4965–4967.
[11] U. Maitra, U. Gupta, M. De, R. Datta, A. Govindaraj, C. N. R. Rao, Highly Effective Visible-Light-Induced H2 Generation by Single-Layer 1T-MoS2 and a Nanocomposite of Few-Layer 2H-MoS2 with Heavily Nitrogenated Graphene, Angew. Chem.-Int. Ed., 2013, 52, pp 13057-13061.
[12] S. P. Kelty, G. Berhault, R. R. Chianelli, the Role of Carbon in Catalytically Stabilized Transition Metal Sulfides, Appl. Cat. A: General, 2007, 322, pp 9-15.
[13] J.A. Rodriguez, P. Liu, J. Dvorak, T. Jirsak, J. Gomes, Y. Takahashi, K. Nakamura, Adsorption and Decomposition of SO_2 on TiC(001): An Experimental and Theoretical Study, Surf. Sci., 2003, 543, L675.
[14] P. Liu, J.A. Rodriguez, J.T. Muckerman, Sulfur Adsorption and Sulfidation of Transition Metal Carbides as Hydrotreating Catalysts, J. Mol. Cat. A: Chem., 2005, 239, pp 116.
[15] R. R. Chianelli, G. Berhault, Symmetrical Synergism and the Role of Carbon in Transition Metal Sulfide Catalytic Materials, Catal. Today, 1999, 53, pp 357.
[16] E. Cominia, L. Yubaob, Y. Brandob, G. Sberveglieria, Gas Sensing Properties of MoO_3 Nanorods to CO and CH_3OH, Chemical Physics Letters, 2005, 407, pp 368–371.
[17] J. Robertson, Diamond-like Amorphous Carbon, Materials Science and Engineering R, 2002, 37, pp 129-281.
[18] A. Jorio, R. Saito, G. Dresselhaus, M. S. Dresselhaus, Raman Spectroscopy in Graphene Related Systems, WILEY-VCH VerlagGmbH & Co. KGaA, Weinheim, 2011, pp 5-9.
[19] P. L. Hansen, P. J. Fallon, W. Krätschmer, An EELS study of fullerite – C_{60}/C_{70}, Chemical Physics Letters, 1991, 181, pp 367-372.

[20] R. A. Alduhaileb, V. M. Ayres, B. W. Jacobs, X. Fan, K. McElroy, M. A. Crimp, A. Hirata, M. Horikoshi, Carbon Onion Films-Molecular Interactions of Multi-Layer Fullerenes, Mater. Res. Soc. Symp. Proc., 2009, 1204, 1204-K05-70.
[21] J. H. Lehman, M. Terrones, E. Mansfield, K. E. Hurst, V. Meunier, Evaluating the Characteristics of Multiwall Carbon Nanotubes, Carbon, 2 011, 49, pp 2581–2602.
[22] J. C. Meyer, A. K. Geim, M. I. Katsnelson, K. S. Novoselov, T. J. Booth, S. Roth, The Structure of Suspended Graphene Sheets, Nature, 2007, 446, pp 60-63.
[23] J. Wang, C. Chen, E. Wang, Y. Kawazoe, A New Carbon Allotrope with Six-Fold Helical Chains in all-sp^2 Bonding Networks, Scientific Reports, 4, 4339.
[24] A. C. Ferrari, B. Kleinsorge, G. Adamopoulos, J. Robertson, W. I. Milne, V. Stolojan, L. M. Brown, A. LiBassi, B. K. Tanner, Determination of Bonding in Amorphous Carbons by Electron Energy Loss Spectroscopy, Raman Scattering and X-ray Reflectivity, Journal of Non-Crystalline Solids, 2000, 266-269, pp 765-768.
[25] J. Yuan, L. M. Brown, Investigation of Atomic Structures of Diamond-like Amorphous Carbon by Electron Energy Loss Spectroscopy, Micron, 2000, 31, pp 515–525.
[26] P. Chu, L. Li, Characterization of Amorphous and Nanocrystalline Carbon Films, Materials Chemistry and Physics, 2006, 96, pp 253–277.
[27] C. B. Murray, D. J. Norris and M. G. Bawendi, Synthesis and Characterization of Nearly Monodisperse CdE (E = sulfur, selenium, tellurium) Semiconductor Nanocrystallites, J. Am. Chem. Soc. 1993, 115, pp 8706–8715.
[28] X. H. Liu, J. Y. Huang, *In situ* TEM Electrochemistry of Anode Materials in Lithium Ion Batteries, Energy Environ. Sci., 2011, 4, pp 3844-3860.
[29] K. W. Urban, Studying Atomic Structures by Aberration-Corrected Transmission Electron Microscopy, Science, 2008, 321, pp 506-510.
[30] B. Gojdka, V. Zaporojtchenko, V. Hrkac, J. Xiong, L. Kienle, T. Strunskus and F. Faupel, Highly Versatile Concept for Precise Tailoring of Nanogranular Composites with a Gas Aggregation Cluster Source, Appl. Phys. Lett., 2012, 100, pp 133104.
[31] B. Gojdka, V. Hrkac, J. Xiong, M. Gerken, L. Kienle, T. Strunskus, V. Zaporojtchenko and F. Faupel, A Critical Evaluation of the 0–3 Approach for Magnetoelectric Nanocomposites with Metallic Nanoparticles, J. Appl. Phys., 2012, 112, pp 044303.
[32] S. Xu, M. Tian, J. Wang, J. Xu, J. M. Redwing, M. H. W. Chan, Nanometer-Scale Modification and Welding of Silicon and Metallic Nanowires with a High-Intensity Electron Beam, Small, 2005, 1, pp 1221-1229.
[33] A. Kulkarni, V. S. K. Chakravadhanula, V. Duppel, D. Meyners, V. Zaporojtchenko, T. Strunskus, L. Kienle, E. Quandt, F. Faupel , Morphological and Magnetic Properties of $TiO_2/Fe_{50}Co_{50}$ Composite Films, J. Mater. Sci., 2011, 46, pp 4638-4645.
[34] U. Pal, N. Koshizaki, S. Terauchi, T. Sasaki, Electron Beam Induced Structural Modification of the Oxidized Silicon Micro-Clusters in ZnO Matrix, Microsc. Microanal. Microstruct. 1997, 8, pp 403-411.
[35] K. Oka, S. Ohnuki, S. Yamashita, N. Akasaka, S. Ohtsuka, H. Tanigawa, Structure of Nano-Size Oxides in ODS Steels and its Stability under Electron Irradiation, Mater. Trans. 2007, 48, pp 2563-2566.
[36] G. Ran, S. Wu, Z. Zhou, R. Qiang, N. Li, L. Wang, In-situ TEM Observation of Microstructural Evolution in 18Cr-ODS Steel Induced by Electron Beam Irradiation, Prog. Nat. Sci.: Mater. Int. 2012, 22, pp 509–513.
[37] P. Linkov, M. Artemyev, A. E. Efimovcd, I. Nabiev, Comparative Advantages and Limitations of the Basic Metrology Methods Applied to the Characterization of Nanomaterials, Nanoscale, 2013, 5, pp 8781.
[38] J. L. Lábár, Electron Diffraction Based Analysis of Phase Fractions and Texture in Nanocrystalline Thin Films, Part I: Principles, Microscopy and Microanalysis, 2009, 15, pp 20.
[39] J. L. Lábár, Consistent Indexing of a (set of) Single Crystal SAED Pattern(s) with the ProcessDiffraction Program, Ultramicroscopy, 2005, 103, pp 237–249.

[40] P. Boullay, L. Lutterotti, D. Chateignera, L. Sicardd, Fast Microstructure and Phase Analyses of Nanopowders Using Combined Analysis of Transmission Electron Microscopy Scattering Patterns, Acta Cryst., 2014, A70, pp 448–456.
[41] D. B. Williams, C. Barry carter, Transmission Electron Microscopy, A Textbook for Materials Science, Springer Science & Business Media, New York, 2009, pp 293-294.
[42] Y. Waseda, Anomalous X-Ray Scattering for Materials Characterization, Springer, 2002.
[43] T. Vogt et al. (eds.), Modeling Nanoscale Imaging in Electron Microscopy, Nanostructure Science and Technology, Springer Science+Business Media, 2012, pp 15.
[44] C. C. Ahn and O. L. Krivanek (1983), EELS Atlas - a reference guide of electron energy loss spectra covering all stable elements (ASU HREM Facility & Gatan Inc, Warrendale, PA, 1983).
[45] D. B. Williams, C. Barry carter, Transmission Electron Microscopy, A Textbook for Materials Science, Springer Science & Business Media, New York, 2009, pp 743.
[46] R. F. Egerton, Electron Energy-Loss Spectroscopy in the Electron Microscope, 2nd edition, Plenum Press, New York, 1996, pp 228.
[47] G. Laurence and C. Alan, Use of electron-energy loss near-edge fine structure in the study of minerals, American Mineralogist, 79, 1994, pp 411-425.
[48] R. Leapman, L. Grunes, and P. Fejes, Study of the L23 edges in the 3d transition metals and their oxides by electron-energy-loss spectroscopy with comparisons to theory, Phys. Rev. B, 26, 1982, pp. 614-635.
[49] L. Garvie, A. Craven, R. Brydson, Use of Electron-Energy Loss Near-Edge Fine Structure in the Study of Minerals, American Mineralogist, 1994, 79, pp 411-425.
[50] C. Scheu, W. Stein, M. Ru, Electron Energy-Loss Near-Edge Structure Studies of a Cu /(11-20) a-Al_2O_3 Interface, Physica Status Solidi (B), 2000, 222, pp 199-211.
[51] C. Jeanguillaume, P. Trebbia, C. Colliex, About the Use of Electron Energy-Loss Spectroscopy for Chemical Mapping of Thin Foils with High Spatial Resolution, Ultramicroscopy, 1978, 3, pp 237–242.
[52] B. Fultz and J. Howe, Transmission Electron Microscopy and Diffractinetry of Materials, ISBN 3-540-67841-7, Springer-Verlag Berlin Heidelberg New York, 2001, pp 178-179.
[53] D. B. Williams, C. Barry carter, Transmission Electron Microscopy, A Textbook for Materials Science, Springer Science & Business Media, New York, 2009, pp 671.
[54] V. Hrkac et al. unpublished results.
[55] D. B. Williams, C. Barry carter, Transmission Electron Microscopy, A Textbook for Materials Science, Springer Science & Business Media, New York, 2009, pp 731.
[56] C. Scheu, W. Stein, and M. Rühle, Electron Energy-Loss Near-Edge Structure Studies of a Cu / (11-20) α-Al_2O_3 Interface. Phys. Status Solidi B, 222, 2000, pp 199-211.
[57] R. Kilaas, Optimal and Near-Optimal Filters in High-Resolution Electron Microscopy, Journal of Microscopy, 1998, 190, pp 45-51.
[58] D. R. G. Mitchell, DiffTools: Electron Diffraction Software Tools for DigitalMicrograph™, Microscopy Research and Technique, 2008, 71, pp 588-593.
[59] P. A. Stadelmann, JEMS - EMS java version, 2004, (http://cimewww.epfl.ch/people/stadelmann/jemswebsite/jems.html)
[60] F. Niefind, W. Bensch, M. Deng, L. Kienle, J. Cruz-Reyes, J. Granados, Co promoted MoS_2 for Hydrodesulfurization: New preparation method of MoS_2 at room temperature and observation of massive differences of the selectivity depending on the activation atmosphere, Applied Catalysis A: General, 2015, 497, pp 72–84.
[61] Y. K. Mishra, S. Kaps, A. Schuchardt, I. Paulowicz, X. Jin, D. Gedamu,S. Freitag, M. Claus, S. Wille, A. Kovalev, S. N. Gorb, and R. Adelung, Fabrication of macroscopically exible and highly porous 3D semiconductornetworks from interpenetrating nanostructures by a simple ame transport approach. Particle & Particle Systems Characterization, 2013, 30, pp 775-783.
[62] M. Mecklenburg, A. Schuchardt, Y. Kumar Mishra, S. Kaps , R. Adelung, A. Lotnyk , L. Kienle, K. Schulte, Aerographite: Ultra Lightweight, Flexible Nanowall, Carbon Microtube Material with Outstanding Mechanical Performance, Adv. Mater. 2012, 24, pp 3486-3490.

[63] A. Schuchardt, T. Braniste, Y. K. Mishra, M. Deng, M. Mecklenburg, M. A. Stevens-Kalceff, S. Raevschi, K. Schulte, L. Kienle, R. Adelung, I. Tiginyanu, Three-dimensional Aerographite-GaN hybrid networks: Single step fabrication of porous and mechanically flexible materials for multifunctional applications, Scientific Reports, 2015, accepted.
[64] T. Maschmeyer, M. Che, Catalytic Aspects of Light-Induced Hydrogen Generation in Water with TiO_2 and Other Photocatalysts: A Simple and Practical Way towards a Normalization? Angew. Chem.-Int. Ed. 2010, 49, pp 1536–1539.
[65] A. Stanislaus, A. Marafi, M. S. Rana, Recent advances in the science and technology of ultra low sulfur diesel (ULSD) production, Catalysis Today, 153, 2010, pp 1–68.
[66] C. S. Song, An overview of new approaches to deep desulfurization for ultra-clean gasoline, diesel fuel and jet fuel, Catal. Today, 86, 1–4, 2003, pp 211–263.
[67] K. de Jong, C. Leon et al, High-resolution electron tomography study of an industrial Ni-Mo/gamma-Al_2O_3 hydrotreating catalyst, The Journal of Physical Chemistry B, 21, 2006, pp 10209-12.
[68] Y. Okamoto, T. Kubota, A model catalyst approach to the effects of the support on Co–Mo hydrodesulfurization catalysts, Catalysis Today, 86, 1–4, 2003, pp 31–43.
[69] I. Eswaramoorthi, V. Sundaramurthy, N. Das, A. K. Dalai, J. Adjaye, Application of multi-walled carbon nanotubes as efficient support to NiMo hydrotreating catalyst, Applied Catalysis A: General, 339, 2, 2008, pp 187-195.
[70] R. Huirache-Acuña, R. Nava, C. Peza-Ledesma, J. Lara-Romero, G. Alonso-Núez, B. Pawelec, E. Rivera-Muñoz, SBA-15 Mesoporous Silica as Catalytic Support for Hydrodesulfurization Catalysts—Review, Materials, 6, 9, 2013, pp 4139-4167.
[71] U. T. Turaga, C. S. Song, MCM-41-supported Co-Mo catalysts for deep hydrodesulfurization of light cycle oil, Catal. Today, 86, 1–4, 1 2003, pp 129–140.
[72] M. Taniguchia, D. Imamuraa, H. Ishigea, Y. Ishiib, T. Muratab, M. Hidaib, T. Tatsumi, Hydrodesulfurization of Benzothiophene over Zeolite-Supported Catalysts Prepared from Mo and Mo–Ni Sulfide Clusters, Journal of Catalysis, 187, 1, 1999, pp 139–150.
[73] J. V. Lauritsen, J. Kibsgaard, G. H. Olesen, P. G. Moses, B. Hinnemann, S. Helveg, J. K. Nørskov, B. S.Clausen, H. Topsøe, E. Lægsgaard, F. Besenbacher, Location and coordination of promoter atoms in Co- and Ni-promoted MoS_2-based hydrotreating catalysts, Journal of Catalysis, 249, 2007, pp 220–233.
[74] Z. D. Huang, PhD thesis, Kiel, 2008.
[75] J. Benck , C. Zhebo, L. Kuritzky, A. Forman, T. Jaramillo, Amorphous Molybdenum Sulfide Catalysts for Electrochemical Hydrogen Production: Insights into the Origin of their Catalytic Activity, ACS Catal., 2012, 2, pp 1916.
[76] H. Vrubel, D. Merki, X. Hu, Hydrogen Evolution Catalyzed by Amorphous MoS_3 and MoS_2 Particles, Energy & Environmental Science, 2012, 5, pp 6136-6144.
[77] M. Daage, R. R. Chianelli, Structure–function relations in molybdenum sulfide catalysts: the "Rim-Edge" model, J. Catal., vol. 149, 1994, pp 414–427.
[78] H. Topsøe, B.S. Clausen, N.Y. Topsoe, P. Zeuthen, Progress in the design of hydrotreating catalysts based on fundamental molecular insight, Stud. Surf. Sci. Catal. 53, 1990, pp 77–102.
[79] H. Topsøe, The role of Co–Mo–S type structures in hydrotreating catalysts, Appl. Catal. A: Gen. 322, 2007, pp 3–8.
[80] G. Eda, T. Fujita, H. Yamaguchi, D. Voiry, M. Chen, M. Chhowalla, Coherent atomic and electronic heterostructures of single-layer MoS_2, by ACS Nano, 6, 8, 2012, pp 7311-7317.
[81] B. L. Abrams, J. P. Wilcoxon, Nanosize Semiconductors for Photooxidation, Critical Rev. Solid State Mater. Sci., 30, 2005, pp 153.
[82] Z. Yin, H. Li, H. Li, L. Jiang, Y. Shi, Y. Sun, G. Lu, Q. Zhang, X. Chen, and H. Zhang, Single-layer MoS_2 phototransistors, ACS Nano, 2012, 6 (1), pp 74–80.
[83] Q. H. Wang, K. Kalantar-Zadeh, A. Kis, J. N. Coleman, M. S. Strano, Electronics and optoelectronics of two-dimensional transition metal dichalcogenides, Nature Nanotechnology, 7, 11, 2012, pp 699-712.

[84] Y. Cao, X. Luo, H. Yu, F. Peng, H. Wang and G. Ning, sp^2- and sp^3-hybridized Carbon Materials as Catalysts for Aerobic Oxidation of Cyclohexane, Catal. Sci. Technol., 2013, 3, pp 2654-2660.
[85] M. F. Thorpe, L Ticha, Properties and Applications of Amorphous Materials, Kluwer Academic Publishers, 2001, pp 330-331.
[86] M. M. Arafat, B. Dinan, S. A. Akbar, A. S M A Haseeb, Gas sensors based on one dimensional nanostructured metal-oxides: a review, Sensors (Basel, Switzerland), 2012, 12, 6, pp 7027-58.
[87] G. Ho, Gas Sensor with Nanostructured Oxide Semiconductor Materials, Sensors (Basel, Switzerland), 2011, 3, 2, pp 150-168.
[88] C. Wang, L. Yin, L. Zhang, D. Xiang, R. Gao, Metal oxide gas sensors: sensitivity and influencing factors, Sensors (Basel, Switzerland), 2010, 10, 3, pp 2088-106.
[89] K. Galatsis, Y.X. Li, W. Wlodarski, E. omini, G. Sberveglieri, C. Cantalini, S. Santucci, M. Passacantando, Comparison of single and binary oxide MoO_3, TiO_2 and WO_3 sol-gel gas sensors, Sens. Actuators B Chem., 2002, 83, pp 276–280.
[90] M.B. Rahmani, S. Keshmiri, J. Yu, A. Sadek, L. Al-Mashat, A. Moafi, K. Latham, Y. Li, W. Wlodarski, K. Kalantar-Zadeh, Gas sensing properties of thermally evaporated lamellar MoO3, Sens. Actuators B Chem., 2010, 145, pp 13–19.
[91] O. Lupan, V. Cretu, M. Deng, D. Gedamu, I. Paulowicz, S. Kaps, Y. K.r Mishra, O. Polonskyi, C. Zamponi, L. Kienle, V. Trofim, I. Tiginyanu, R. Adelung, Versatile growth of freestanding orthorhombic alpha-molybdenum trioxide nano- and microstructures by rapid thermal processing for gas nanosensors, J. Phys. Chem. C, 2014, 118 (27), pp 15068–15078.
[92] J. Djamil, S. Segler, W. Bensch, U. Schürmann, M. Deng, L. Kienle, S. Hansen, T. Beweries, L. von Wüllen, S. Rosenfeldt, S. Förster, H. Reinsch, *In situ* Formation of MoS2-based Inorganic-Organic Nanocomposites by Directed Thermal Decomposition, Chemistry - A European Journal, 2015, 21, pp 1-9.
[93] M. M. Disko, C. C. Ahn and B. Fultz, Transmission Electron Energy Loss Spectrometry in Materials Science (Booknews Inc., Portland, OR, 1992).
[94] A. Kocbach, Y. Li, K. E. Yttri, F. R. Cassee, P. E. Schwarze, E. Namork, Physicochemical Characterisation of Combustion Particles from Vehicle Exhaust and Residential Wood Smoke, Particle and fibre toxicology, 2006, 3, pp 1.
[95] K. A. Katrinak, P. Rez, P. R. Buseck, Structural Variations in Individual Carbonaceous Particles from an Urban Aerosol, Environmental Science & Technology, 1992, 26, 10, pp 1967-1976.
[96] S. Min, G. Lu, Sites for High Efficient Photocatalytic Hydrogen Evolution on a Limited-Layered MoS_2 Cocatalyst Confined on Graphene Sheets—The Role of Graphene. J. Phys. Chem. C, 2012, 116, pp 25415–25424.
[97] T. Maschmeyer, M. Che, Intrinsic Catalytic Activity versus Effective Light Usage - A reply to Professor Kisch's Comment. Angew. Chem.-Int. Ed., 2010, 49, pp 9590–9591.
[98] H. Kisch, On the Problem of Comparing Rates or Apparent Quantum Yields in Heterogeneous Photocatalysis. Angew. Chem.-Int. Ed., 2010, 49, pp 9588–9589.
[99] K. D. Bronsema, J. L. De Boer, F. Jellinek, On the Structure of Molybdenum Diselenide and Disulfide, Zeitschrift für anorganische und allgemeine Chemie, 1986, 540(9-10), pp 15–17.
[100] M. Deng, V. Hrkac, U. Shürmann, B. Erkatal, N. Wolff, K. Gerwien, B. Hesseler, F. Beiroth, V. Duppel, W. Bensch, L. Kienle, Nanocomposite CdSe / Cr_2Se_3: Synthesis, Characterization and *in situ* Transformation Study, Zeitschrift für anorganische und allgemeine Chemie, 2015, 641(2), pp 214–220.
[101] C. Muratore, V. Varshney, J. J. Gengler, J. Hu, J. E. Bultman, A. K. Roy, B. L. Farmer, A. A. Voevodin, Thermal Anisotropy in Nano-Crystalline MoS_2 Thin Films, Phys.Chem.Chem.Phys., 2014, 16, pp 1008.
[102] A. Patterson, The Scherrer Formula for X-Ray Particle Size Determination, Phys. Rev., 1939, 56, pp 978–982.
[103] F. Niefind, J. Djamil, W. Bensch, B. R. Srinivasan, I. Sinev, W. Grünert, M. Deng, A. Lotnyk, L. Kienle, L. Dura, S. Hansen, T. Beweries, Convenient and Simple Synthesis of an Amorphous Molybdenum Sulfide Based Material Obtained at Room Temperature: Characterization and Photocatalytic Hydrogen Evolution, in submission.

[104] A. Kudo, Y. Miseki, Heterogeneous Photocatalyst Materials for Water Splitting, Chem. Soc. Rev., 2009, 38, pp 253-78.
[105] X. Chen, S. Shen, L. Guo, S. S. Mao, Semiconductor-Based Photocatalytic Hydrogen Generation, Chem. Rev., 2010, 110, pp 6503-6570.
[106] T. Waitz, H. P. Karnthaler, Analysis of HRTEM Contrast of Overlapping Structures at Transformation Interfaces, Phys. Stat. Sol. (a), 1998, 166, pp 107.
[107] B. Gilbert, F. Huang, H. Zhang, G. A. Waychunas, J. F. Banfield, Nanoparticles: Strained and Stiff, Science 2004,305 (5684) pp. 651-654.
[108] T. Kakeshita, T. Fukuda, A. Saxena, A. Planes, Disorder and Strain-Induced Complexity in Functional Materials, Springer Science & Business Media, pp 137.
[109] P. Debye, Zerstreuung von Roentgenstrahlen, Ann. Physik., 1915, 46, pp 809–823.
[110] M. Blackmann, On the Intensities of Electron Diffraction Rings, Proc. Roy. Soc., 1939, A173, pp 68-82.
[111] F. R. L. Schoening, Influence of Crystal Size on Electron Diffraction Intensities, AppL Cryst., 1973, 6, pp 145.
[112] A. N. Enyashin, M. Bar-Sadan, J. Sloan, L. Houben, G. Seifert, Nanoseashells and Nanooctahedra of MoS_2: Routes to Inorganic Fullerenes, Chemistry of Materials, 2009, 21, pp 5627-5636.
[113] M. Karroua, H. Matralis, E. Sham, P. Grange, B. Delmon, Synergy Between the CoMoS Phase and Supported or Unsupported Cobalt sulfide: Existence of a Remote Control Effect, Bull. Chem. Soc. Jpn., 1995, 68, pp 107-119.
[114] L. Alvarez, J. Espino, C. Ornelas, J.L. Rico, M. T. Cortez, G. Berhault, G. Alonso, Comparative Study of MoS_2 and Co/MoS_2 Catalysts Prepared by *ex situ*/*in situ* Activation of Ammonium and Tetraalkylammonium Thiomolybdates, J. Mol. Catal. A Chem., 2004, 210, pp 105-117.
[115] H. Nava, C. Ornelas, A. Aguilar, G. Berhault, S. Fuentes, G. Alonso, Cobalt-Molybdenum Sulfide Catalysts Prepared by In Situ Activation of Bimetallic (Co-Mo) Alkylthiomolybdates, Catal. Lett., 2003, 86, pp 257-265.
[116] T. Stephenson, Z. Li, B. Olsen, D. Mitlin, Lithium Ion Battery Applications of Molybdenum Disulfide (MoS_2) Nanocomposites, Energy Environ. Sci. 2014, 7, pp 209-231.
[117] M. Poisot, W. Bensch, S. Fuentes, G. Alonso, Decomposition of Tetra-Alkylammonium Thiomolybdates Characterised by Thermoanalysis and Mass Spectrometry, Thermochim. Acta. 2006, 444, pp 35-45.
[118] G. Alonso, G. Berhault, A. Aguilar, V. Collins, C. Ornelas, S. Fuentes, R.R. Chianelli, Characterization and HDS Activity of Mesoporous MoS_2 Catalysts Prepared by *in Situ* Activation of Tetraalkylammonium Thiomolybdates, J. Catal. 2002, 208, pp 359-369.
[119] R. F. Egerton, Electron Energy-Loss Spectroscopy in the Electron Microscope, 2nd edition, Plenum Press, New York, 1996, pp 225.
[120] R. Brydson, Z. Zhili and A. Brown, Revisiting the Determination of Carbon sp^3/sp^2 Ratios via Analysis of the EELS Carbon K-edge, EMC 2008, Vol 1, Instrumentation and Methods, edited by M. Luysberg, K. Tillmann and T. Weirich (Springer-Verlag, Berlin, Germany,2008) pp 357-358.
[121] Handbook of X-ray Photoelectron Spectroscopy, Ed., C. D. Wanger, W. M. Riggs, L. E. Davis, J. F. Moulder and G. E.Muilenberg Perkin-Elmer Corp., Physical Electronics Division, Eden Prairie, Minnesota, USA, 1979, pp 40-41.
[122] D. Wang, D. S. Su, R. Schlögl, Electron Beam Induced Transformation of MoO_3 to MoO_2 and a New Phase MoO, Zeitschrift für anorganische und allgemeine Chemie, 2004, 630 (7), pp 1007-1014.
[123] D. E. Diaz-Droguett, A. Zuñiga, G. Solorzano, V. M. Fuenzalida, Electron Beam-induced Structural Transformations of MoO_3 and MoO_{3-x} Crystalline Nanostructures. Journal of Nanoparticle Research, 2012, 14 (1), pp 1-9.
[124] J. C. Park, H. Song, Synthesis of Polycrystalline Mo/MoO_x Nanoflakes and Their Transformation to MoO_3 and MoS_2 Nanoparticles, Chemistry of Materials, 2007, 19 (11), pp 2706-2708.
[125] D. O. Scanlon, G. W. Watson, D. J. Payne, G. R. Atkinson, R. G. Egdell, D. S. L. Law, Theoretical and Experimental Study of the Electronic Structures of MoO_3 and MoO_2, Journal of Physical Chemistry C 2010, 114 (10), pp 4636-4645.

[126] Y. Chen, C. Lu, L. Xu, Y. Ma, W. Hou, J.-J. Zhu, Single-crystalline Orthorhombic Molybdenum Oxide Nanobelts: Synthesis and Photocatalytic Properties, Crystal Engineering Communications, 2010, 12 (11), pp 3740-3747.
[127] P. L. Gai, Dynamic Studies of Metal Oxide Catalysts: MoO_3, Philosophical Magazine A 1981, 43 (4), pp 841-855.
[128] T. Leisegang, A. A. Levin, J. Walter, D. C. Meyer, *In situ* X-ray Analysis of MoO_3 Reduction, Crystal Research and Technology, 2005, 40 (1-2), pp 95–105.
[129] L. Fang, Y. Shu, A. Wang, T. Zhang, Green Synthesis and Characterization of Anisotropic Uniform Single-crystal α-MoO_3 Nanostructures, Journal of Physical Chemistry C, 2007, 111 (6), pp 2401-2408.
[130] S. Phadungdhitidhada, P. Mangkorntong, S. Choopun, N. Mangkorntong, D. Wongratanaphisan, Synthesis of MoO_3 Nanobelts by Medium Energy Nitrogen Ion Implantation, Materials Letters, 2011, 65 (3), pp 568-571.
[131] N. Illyaskutty, H. Kohler, T. Trautmann, M. Schwotzer, V. P. M. Pillai, Enhanced Ethanol Sensing Response from Nanostructured MoO_3 : ZnO Thin Films and their Mechanism of Sensing, Journal of Materials Chemistry C, 2013, 1, pp 3976-3984.
[132] E. Comini, M. Ferroni, V. Guidi, Response to Ethanol of Thin Films based on Mo and Ti Oxides deposited by Sputtering, Sens. Actuators, B, 2003, 93, pp 409–415.
[133] E. Comini, L. Yubao, Y. Brando, V. Sberveglieri, Gas Sensing Properties of MoO_3 Nanorods to CO and CH_3OH, Chem. Phys. Lett., 2005, 407, pp 368–371.
[134] O. Lupan, T. Braniste, M. Deng, L. Ghimpu, I. Paulowicz, Y. K. Mishra, L. Kienle, R. Adelung, I. Tiginyanu, Fast Switching Sensors based on individual Shell-Core Ga_2O_3/GaN@SnO_2 Nanobelt with Heterogeneous Nanocrystalline Shell in Mixed Phases, in submission.
[135] D. Dohy, J. R. Gavarri, Oxyde β-Ga_2O_3: Champ de force, Dilatation Thermique, et Rigidité Anisotropies, J. Solid State Chem., 1983, 49, pp 107–117.
[136] H. Huppertz, S. A. Hering, C. E. Zvoriste, S. Lauterbach, O. Oeckler, R. Riedel, I. Kinski|, High-Pressure Synthesis, Electron Energy-Loss Spectroscopy Investigations, and Single Crystal Structure Determination of a Spinel-Type Gallium Oxonitride Ga2.79□0.21(O3.05N0.76□0.19), Chem. Mater., 2009, 21, pp 2101–2107.
[137] C. Zvorişte, High-Pressure Synthesis, Crystal Structure and Physical Properties of Gallium Oxonitride, PhD thesis, Darmstadt, 2011.
[138] A. Gurlo, R. Riedel, *In Situ* and Operando Spectroscopy for Assessing Mechanisms of Gas Sensing, Angewandte Chemie International Edition**,** 2007, 46, pp 3826-3848.
[139] R.F. Egerton, P. Li, M. Malac, Radiation Damage in the TEM and SEM, Micron, 2004, 34, pp 399–409.
[140] S. Berger, D. McKenzie, P. Martin, EELS Analysis of Vacuum Arc-Deposited Diamond-like Films, Philosophical Magazine Letters, 1988, 57, 6, pp 285-290.
[141] V. Serin, E. Beche, R. Berjoan, O. Abidate, D. Rats, J. Fontaine, L.Vandenbulcke, C. Germain and A. Catherinot, Proc. of the Vth Int. Symp. on Diamond Materials, J. L. Davidson, W. D. Brown, A. Gicquel, B. V. Spytsin and J.C. Angus Eds, The Electrochem. Soc., Pennington, NJ, 1998, pp. 126-141.
[142] http://pc-web.cemes.fr/eelsdb/index.php?page=displayspec.php&id=24
[143] A. F. Wright, J. S. Nelson, Consistent Structural Properties for AlN, GaN, and InN, Phys. Rev. B, 1995, 51, pp 7866-7869.
[144] H. Sowa, H. Ahsbahs, High-pressure X-ray Investigation of Zincite ZnO Single Crystals Using Diamond Anvils with an Improved Shape, J. Appl. Cryst., 2006, 39, pp 169-175.
[145] Y. Ding, Z. L. Wang, Structures of Planar Defects in ZnO Nanobelts and Nanowires, Micron, 2009, 40, pp 335–342.
[146] D. Zakharov, Z. Liliental-Weber, B. Wagner, Z. Reitmeier, E. Preble, R. Davis, Structural TEM Study of Nonpolar *a*-plane Gallium Nitride rown on (11$\bar{2}$0)4*H*-SiC by Organometallic Vapor Phase Epitaxy, Physical Review B, 2005, 71, pp 235334.
[147] S. Das, S. Sinha, B. Das, S. K. Suar, S. K. S. Parashar, M. Mohapatra, A. Mishra, S. K. Tripathy, Microwave Assisted Hydrothermal Synthesis of Well-dispersed and Thermally Stable Ag@SnO_2

Core–shell Nano-composites for Propane Sensing Applications, J. Mater. Sci.: Mater. Electron., 2014, 25, pp 217-223.
[148] S. Gai, C. X. Li, P. P.Yang, J. Lin, Recent Progress in Rare Earth Micro/nanocrystals: Soft Chemical Synthesis, Luminescent Properties, and Biomedical Applications, Chem. Rev., 2014, 114, pp 2343-2389.
[149] C. Nan, M. I. Bichurin, S. Dong, D. Viehland and G. Srinivasan, Multiferroic Magnetoelectric Composites: Historical Perspective, Status, and Future Directions, J. Appl. Phys., 2008, 103, pp 031101.
[150] T. Wilke, D. Schricker, K. Kleinermanns, Solar Water Splitting by Semiconductor Nanocomposites and Hydrogen Storage with Quinoid Systems, Open J. Phys. Chem., 2012, 2, pp 195-203.
[151] B. O. Dabbousi, J. Rodriguez-Viejo, F. V. Mikulec, J. R. Heine, H. Mattoussi, R. Ober, K. F. Jensen, M. G. Bawendi, CdSe-ZnS Core−Shell Quantum Dots: Synthesis and Characterization of a Size Series of Highly Luminescent Nanocrystallites, J. Phys. Chem. B 1997, 101, pp 9463–9475.
[152] R. M. Morcos, C. Mitterbauer, N. Browning, S. Risbud, and A. Navrotsky, Energetics of CdS_xSe_{1-x} Quantum Dots in Borosilicate Glasses, J. Non-Cryst. Solids 2007, 353, pp 2785–2795.
[153] L. Korala, Z. Wang, Y. Liu, S. Maldonado, S. L. Brock, Uniform Thin Films of CdSe and CdSe(ZnS) Core(shell) Quantum Dots by Sol-Gel Assembly: Enabling Photoelectrochemical Characterization and Electronic Applications, *ACS Nano* 2013, 7, pp 1215–1223.
[154] D. J. Smith, A. K. Petford-Long, L. R. Wallenberg, J. O. Bovin, Dynamic Atomic-Level Rearrangements in Small Gold Particles, Science, 1986, 233, pp 872– 875.
[155] I. Salisbury, R. S. Timsit, S. D. Berger, and C. J. Humphreys, Nanometer Scale Electron Beam Lithography in Inorganic Materials, Appl.Phys. Lett., 1984, 45, pp 1289.
[156] X. Lin, R. Zhou, J. Zhang, S. Fei, A Novel One-step Electron Beam Irradiation Method for Synthesis of Ag/Cu_2O Nanocomposites, Appl. Surf. Sci., 2009, 256, pp 889-893.
[157] H. J. Im, K. S. Choi, Radiolytic Production of Ag-containing Nanocomposite Colloids in Presence of Lithium Ions, J. Nanosci. Nanotechnol., 2012, 12, pp 5808-5811.
[158] A. H. Latham and M. E. Williams, TEM-Induced Structural Evolution in Amorphous Fe, Ni and Co Oxide Nanoparticles, Langmuir 2008, 24, pp 14195–14202.
[159] A. H. Latham, M. J. Wilson, P. Schiffer and M. E. Williams, TEM-induced Structural Evolution in Amorphous Fe oxide Nanoparticles, J. Am. Chem. Soc. 2006, 128, pp 12632–12633.
[160] Y. Zhai, L. Han, P. Wang, G. Li, W. Ren, L. Liu, E. Wang, and S. Dong, Superparamagnetic Plasmonic Nanohybrids: Shape-Controlled Synthesis, TEM-Induced Structure Evolution, and Efficient Sunlight-Driven Inactivation of Bacteria, ACS Nano 2011, 5, pp 8562–8570.
[161] L. Kienle, A. Lotnyk, V. Duppel, F. Beiroth, B. Hessler, K. Gerwien, W. Bensch, MC 2009, M2.P727, pp 133-134.
[162] Y. Adachi, M. Ohashi, T. Kaneko, M. Yuzuri, Y. Yamaguchi, S. Funahashi, Y. Morii, Magnetic Structure of Rhomboheral Cr_2Se_3, J. Phys. Soc. Jpn. 1994, 63, pp 1548.
[163] J. Tomforde, W. Bensch, L. Kienle, V. Duppel, P. Merkelbach, M. Wuttig, Thin Films of Ge-Sb-Te-Based Phase Change Materials: Microstructure and in Situ Transformation, Chem. Mater., 2011, 23, pp 3871–3878.
[164] B. Predel in Phase Equilibria, Crystallographic and Thermodynamic Data of Binary Alloys (Eds. B. Predel), Springer, Berlin Heidelberg 1994, vol. 5d, pp 1-5.
[165] O. Madelung in Semiconductors Data Handbook, Springer, Berlin 2004, pp 815-835.
[166] K. Pisharody, Thermoelectric Properties of Chromium Sulfo-Selenides, J. Solid State Chem., 1979, 30, pp 149-156.
[167] F. Gardea, M. Naraghi, D. Lagoudas, Effect of Thermal Interface on Heat Flow in Carbon Nanofiber Composites, ACS Appl. Mater. Interfaces 2014, 6, pp 1061-72.
[168] K. Sharma, K. Barua, Electrical Properties of Evaporated CdSe Films, J. Phys. D: Appl. Phys., 1979, 12, pp 1729-1735.
[169] M. Behrens, R. Kiebach, W. Bensch, D. Häussler, W. Jäger, Synthesis of Thin Cr_3Se_4-films from Modulated Elemental Reactants via Two Amorphous Intermediates: A Detailed Examination of the Reaction Mechanism, Inorg. Chem. 2006, 45, pp 2704-2712.

[170] K. G. Barraclough, A. Meyer, The CdSe-Cr_2Se_3 System and the Formation of the Ferromagnetic Semiconducting Spinel, $CdCr_2Se_4$, J. Crys. Grow. 1973, 20, pp 212-216.
[171] J. Thomas, C. Ducati, R. Leary, P. Midgley, Some Turning Points in the Chemical Electron Microscopic Study of Heterogeneous Catalysts, ChemCatChem, 2013, 5(9), pp 2560-2579.
[172] H. Friedrich, P. de Jongh, A. Verkleij, K. de Jong, Electron Tomography for Heterogeneous Catalysts and Related Nanostructured Materials; Chemical Reviews, 2009, 5, pp 1613-1629.
[173] E. Rauch and L. Dupuy, Rapid Spot Diffraction Patterns Identification Through Template Matching, Arch. Metall. Mater, 2005, 1, pp 1-13.
[174] A. Kobler, A. Kashiwar, H. Hahn, and C. Kübel. Combination of *in situ* Straining and ACOM TEM: A Novel Method for Analysis of Plastic Deformation of Nanocrystalline Metals. Ultramicroscopy, 2013, 128, pp 68-81.
[175] E. Rauch, A. Duft, Orientation Maps Derived from TEM Diffraction Patterns Collected with an External CCD Camera, Materials Science Forum, 2005, pp 1-6.
[176] V. Hrkac, A. Kobler, S. Marauska, A. Petraru, U. Schürmann, V. S. K. Chakravadhanula, V. Duppel, H. Kohlstedt, B. Wagner, B. V. Lotsch, C. Kübel, L. Kienle: Structural Study of Growth, Orientation and Defects Characteristics in the Functional Microelectromechanical System Material Aluminium Nitride, J. Appl. Phys., 2015, 117(1), 014301.

Acknowledgement

Thanks to my Doktorvater, Prof. Dr. Lorenz Kienle, who offered me this great opportunity to work in the group of Synthesis and Real Structure, and opened the door to the reciprocal space for me.

To Dr. Ulrich Schürmann, Dr. Burak Erkatal and Dr. Viktor Hrkac, they are the inspiring mentors, supportive colleagues and good friends for me in my three years of PhD life. Especiall thanks for their patience and informative suggestions to help me improving this thesis to the final state.

To Christin Szillus for the TEM sample preparation and the nice atmosphere she created for working together.

To Torben Dankwort, for the kind help, interesting discussions, nice conversations and fun MC conference time we have spent together in work, in parties in Kiel and in Regensburg. And to my colleagues Gero Neubüser and Julian Strobel, for the enjoyable time in the office and in Mawi Stammtisch. To all members in group SRS: Niklas Wolff, Igor Barg, Marius Kamp and Lena Nolte, for their professional assistance and nice help. To our reliable secretary Katrin Brandenburg, for her consistent help on both administrative and scientific work.

To the financial support of Deutsche Forschungsgemeinschaft (DFG). To my collaboration partners from Inorganic Chemistry department of CAU Kiel, Prof. Dr. Wolfgang Bench, Felix Niefind, John Djamil, David Westfall and Björn Reimer. Without them, there will not be so fruitful outcomes from the catalyst project. Also thanks to my other collaboration partners, Josef Eiblmeier, Arnim Schuchardt, Dr. Yogendra Mishra and Dr. Oleg Lupan, for introducing me to the world other than catalysts.

To Viola Duppel, Dr. Kiran Chakravadhanula and Dr. Andriy Lotnyk, for their measurements in Max Planck Institute for Solid State Research of Stuttgart, in KNMF at the Karsruhe Institute of Technology and in Leibniz Institute of Surface Modification in Leipzig. Their kind advices for improving my scientific skill are very valuable.

To my office colleagues in Room F-126, Simon Fichtner and Dr. Steffen Chemnitz, for providing me a quiet and productive environment for writing my thesis.

Grate thanks to my uncle Bo Deng for the English language revision of my thesis.

In the end, I would like to express my sincere gratitude to my friends, to my lovely parents, and to my boyfriend Gerrit Gardini, for their endless love and unconditional support in every part of my life, with them I can achieve everything.

List of Publications

1. J. Eiblmeier, M. Kellermeier, M. Deng, L. Kienle, J. M. G. Ruiz, W. Kunz: Bottom-Up Self-Assembly of Amorphous Core-Shell-Shell Nanoparticles and Biomimetic Crystal Forms in Inorganic Silica-Carbonate Systems, Chem. Mater., 25(9): 1842-1851, 2013.
2. M. Deng, V. Hrkac, K. Gerwien, B. Hesseler, F. Beiroth, V. Duppel, W. Bensch, L. Kienle: Observation of the Transformation Behavior of CdSe-Cr_2Se_3 Nanoparticle Composites by *in situ* TEM Techniques, MC Regensburg, IM.3.P068, 2013.
3. O. Lupan, V. Cretu, M. Deng, D. Gedamu, I. Paulowicz, S. Kaps, Y. K Mishra, O. Polonskyi, C. Zamponi, L. Kienle, V. Trofim, I. Tiginyanu, R. Adelung: Versatile Growth of Freestanding Orthorhombic alpha-Molybdenum Trioxide Nano- and Microstructures by Rapid Thermal Processing for Gas Nanosensors, J. Phys. Chem. C, 118(27): 15068-15078, 2014.
4. M. Deng, V. Hrkac, U. Schürmann, B. Erkatal, N. Wolff, K. Gerwien, B. Hesseler, F. Beiroth, V. Duppel, W. Bensch, L. Kienle: Nanocomposite CdSe / Cr_2Se_3: Synthesis, Characterization and *in situ* Transformation Study, Zeitschrift für anorganische und allgemeine Chemie, 641(2): 214–220, 2015,
5. A. Schuchardt, T. Braniste, Y. K. Mishra, M. Deng, M. Mecklenburg, M. A. Stevens-Kalceff, S. Raevschi, K. Schulte, L. Kienle, R. Adelung, I. Tiginyanu, Three-dimensional Aerographite-GaN Hybrid Networks: Single Step Fabrication of Porous and Mechanically Flexible Materials for Multifunctional Applications, Scientific Reports, 5 : 8839, 2015.
6. F. Niefind, W. Bensch, M. Deng, L. Kienle, J. Cruz-Reyes, J. Granados, Co promoted MoS_2 for Hydrodesulfurization: New Preparation Method of MoS_2 at Room Temperature and Observation of Massive Differences of the Selectivity Depending on the Activation Atmosphere, Applied Catalysis A: General, 497,72–84, 2015.
7. J. Djamil, S. Segler, W. Bensch, U. Schürmann, M. Deng, L. Kienle, S. Hansen, T. Beweries, L. von Wüllen, S. Rosenfeldt, S. Förster, H. Reinsch, *In situ* Formation of MoS_2-based Inorganic-Organic Nanocomposites by Directed Thermal Decomposition, Chemistry - A European Journal, 21, 1-9, 2015.
8. F. Niefind, J. Djamil, W. Bensch, B. R. Srinivasan, I. Sinev, W. Grünert, M. Deng, A. Lotnyk, L. Kienle, L. Dura, S. Hansen, T. Beweries, Convenient and Simple Synthesis of an Amorphous Molybdenum Sulfide Based Material Obtained at Room Temperature: Characterization and Photocatalytic Hydrogen Evolution, in submission.
9. O. Lupan, T. Braniste, M. Deng, L. Ghimpu, I. Paulowicz, Y. K. Mishra, L. Kienle, R. Adelung, I. Tiginyanu, Rapid Switching and Ultra-Responsive Nanosensors Based on Individual Shell-Core Ga_2O_3/GaN:O_x@SnO_2 Nanobelt with Nanocrystalline Shell in Mixed Phases, Sensors and Actuators B: Chemical, accepted, 2015.

Declaration

I declare that apart from the guidance of my supervisor, the work presented in this thesis was independently performed by me. For the research I have used only the equipment, software and materials mentioned here, without any illegal help of others and without using any resources that have not been denoted. Measurements or samples prepared by others have been signified in the text.

The rules of Good Scientific Practice of the DFG are followed during the preparation of this work. This thesis has been neither partially nor wholly submitted as a doctoral degree to another examining body. It is submitted to Christian-Albrechts-Universität zu Kiel only. This work has already been published in parts in the publications as listed above.

Kiel, May 2015

_____

(Mao Deng)